UiO : Department of Mathematics
University of Oslo

Log-Layer Mismatch In Wall Modeled Large Eddy Simulation

Dennis Fimland

Master's Thesis, Spring 2022

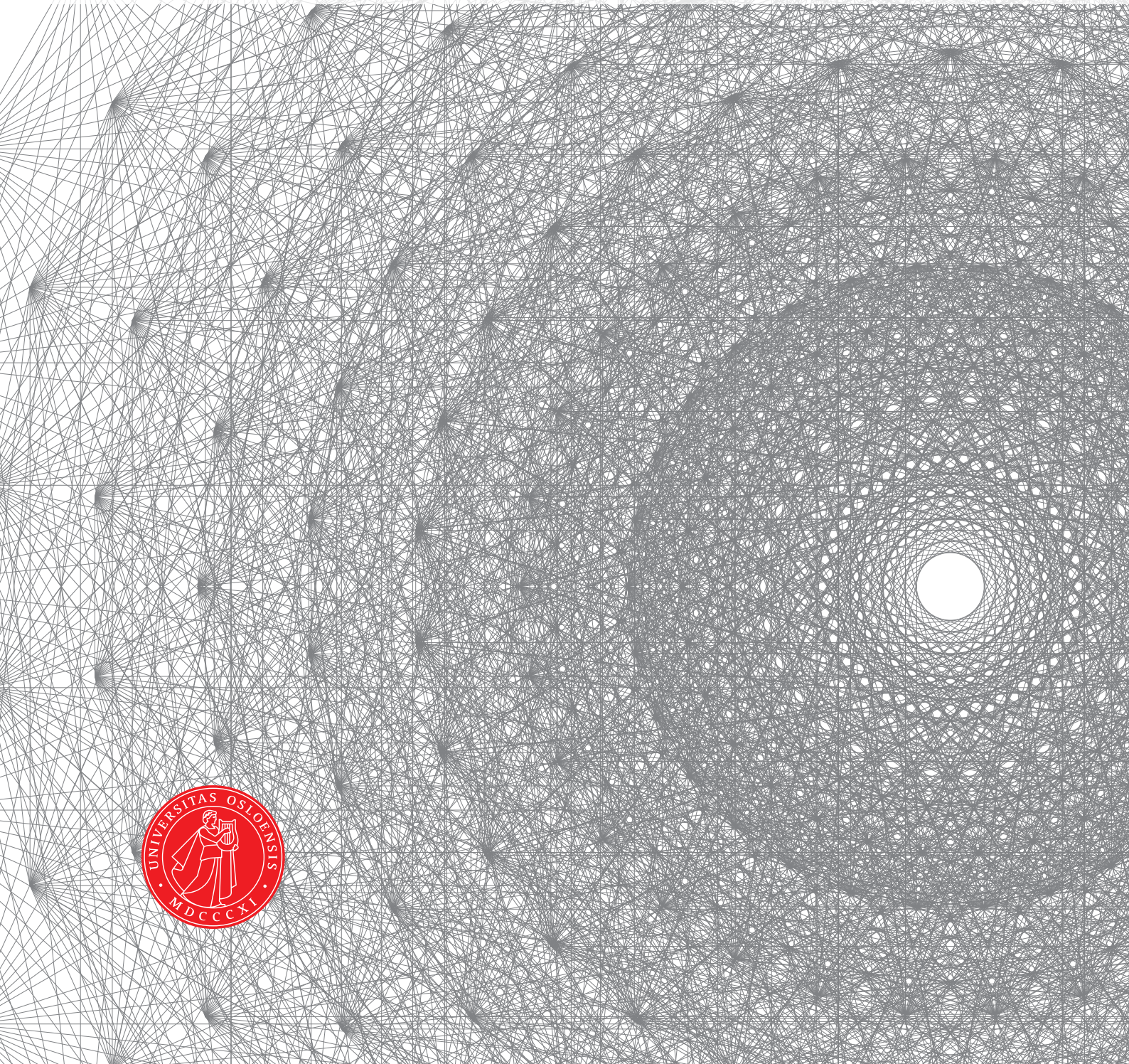

This master's thesis is submitted under the master's programme *Computational Science*, with programme option *Mechanics*, at the Department of Mathematics, University of Oslo. The scope of the thesis is 60 credits.

The front page depicts a section of the root system of the exceptional Lie group E_8, projected into the plane. Lie groups were invented by the Norwegian mathematician Sophus Lie (1842–1899) to express symmetries in differential equations and today they play a central role in various parts of mathematics.

It is only thanks to Christobal Skjulsvik that the work in this thesis was at all feasible

Preface

This Master Thesis is a presentation of my work conducted during the fall of 2021 and the spring of 2022 as a part of my masters degree in Computational Science from the Department of Mathematics at the University of Oslo.

Turbulence springs up in virtually any system containing moving fluids. Clouds are governed by turbulence, as is the motion of waves and solar winds. Due to the ubiquitous nature of turbulence I, somewhat naively, started this thesis with the hope of understanding the complex nature the phenomenon. After a year working with the topic I am still no closer to answering the age old question *What is Turbulence*? Unfortunately, I am not alone, as turbulence is one of the prevailing mysteries of physics.

Great strides within the field of computational sciences have given engineers and scientists the opportunity to perform high fidelity simulations of turbulent fluid flows. This has proven to be an excellent tool for increasing our insight into the nature of turbulence. As a better understanding of turbulence will have huge positive impacts, such as more efficient wind farms, better weather forecasts, and smoother rides for millions of airline passengers, I would like to contribute to the fascinating world of computational modelling of turbulence.

The work has been challenging yet rewarding. A considerable amount of time has been dedicated to implementing new features to existing software. The use of the experimental code developed by Cascade Technology ensured that I had complete control over what the program was doing and was thus an invaluable tool in this work. The challenges related to implementing the different filtering strategies have given me greater insight into the world of numerical fluid dynamics and parallel computing. I have also gained a great amount of respect for all the engineers and scientists that struggle daily with implementing accurate and efficient algorithms for solving the non-forgiving Navier-Stokes equations.

Abstract

Several authors have reported large discrepancies in the normalized mean velocity profile produced by wall modeled Large Eddy Simulation. These discrepancies, known as the *Log-Layer Mismatch*, occur independent of grid topology, subgrid model and wall-model. A significant research effort has been aimed at solving this problem over the past decade. However, there exists no universally accepted model thus far. The most common approaches seek to reduce this mismatch by modifying the subgrid model, changing the wall model height, or by filtering the wall model input in time and/or space.

In this thesis the effect of temporal filtering, spatial filtering, and changing the wall model height is investigated. As a test case, a fully developed turbulent channel driven by a constant pressure gradient at $Re_\tau = 5200$ is considered. The simulation campaign considers two different cell lattices: hexahedral and truncated octahedral. Simulations are performed with and without subgrid modelling. The results are compared with DNS data concerning the mean velocity profile, velocity gradient, and the Reynolds stresses.

It is shown that both the temporal filtering technique and moving the wall model matching location away from the wall have a positive effect on LLM, while spatial filtering has little effect on the predicted mean velocity profile. Further, it is found that the simulations on truncated octahedral meshes perform the best. Turning off the subgrid model reduces the magnitude of LLM, while deteriorating the accuracy of the velocity gradient and the Reynolds stresses.

Several prevailing explanations for LLM are studied, however, non of the arguments seems to give an adequate explanation as to why the phenomenon occurs. Closer study of the algebraic wall model indicates that by enforcing the *Law of The Wall* locally and instantaneously one introduces additional modeling errors proportional to the fluctuations in the velocity field and the instantaneous wall stress. Further analysis of the the semi-discrete transport equations in the near-wall region shows that the computed velocity field relies on data from adjacent control volumes. The non-local nature of the transport equation is believed to be the main reason for why the prevailing arguments of LLM fail to provide a complete explanation of how the phenomenon occurs.

Acknowledgements

I would like to thank the Department of Total Defence at The Norwegian Defence Research Establishment for giving me this opportunity and for providing computational rescues and fresh coffee. Without parallel computing and vast amounts of coffee this study would not have been possible.

Further, I want to express my greatest gratitude to Magnus Vartdal for our regular and always motivating meetings, and superb guidance on this subject over the past year. I consider myself lucky to have such a dedicated, knowledgeable and friendly supervisor. I also want to thank Andreas Nygård Osnes, Espen Åkervik and Hannibal Fossum for excellent company throughout this last year and for providing high quality dilemmas.

I gratefully acknowledge MSc Erlend Flatøy, Halvor Horge and Jannie Fimland for their comments on a draft of this manuscript. Finally, I want to direct special appreciation towards my parents and my good friend Håvard Ola Eggen for all your help and for all the joy you have brought into my life. Without your help and company the last year I would not have been able to finish this thesis.

Contents

Nomenclature

Abbreviations

CFD	Computational Fluid Dynamics
DNS	Direct Numerical Simulations
Hex	Hexahedron mesh topology
LES	Large Eddy Simulation
LLM	Log-Layer Mismatch
MPI	Message Passing Interface
Oct	Truncated Octahedron mesh topology
PDF	Probability Density Function
RANS	Reynolds Average Navier-Stokes
TBL	Turbulent Boundary Layer
TBLE	Turbulent Boundary Layer Equation
WMLES	Wall Modeled Large Eddy Simulation
WRLES	Wall Resolved Large Eddy Simulation
WSM	Wall Stress Models

Greek and Roman Letters

Φ_M	Overshoot of the velocity gradient
τ_{wp}	Predicted fluctuating wall stress
P	Pressure
p	Static pressure
u, v, w	Velocity components in Cartesian coordinates
u_1, u_2, u_3	Velocity components in Cartesian coordinates
u_p	Wall-parallel velocity

x, y, z	Cartesian coordinates
Δt	Time step
$\Delta x, \Delta y, \Delta z$	Length, height and width of the computational grid cells
Δx_c	Characteristic cell size
Δ	Filtering width of primary filter
δ	Boundary layer thickness
δ	Channel half width
Δ_{x_f}	Filter width
ϵ	Mean dissipation rate
ϵ_{k_f}	Viscous dissipation of the resolved velocity field
η	Kolmogorov length scale
κ_η	Kolmogorov wave number
ϵ_{ij}	Viscous dissipation rate tensor
$\mathcal{C}_{ij}$	Cross stress tensor
$\mathcal{D}_{ij}$	Viscous diffusion rate tensor
$\mathcal{L}$	Reynolds Average Navier-Stokes operator
$\mathcal{L}_{ij}$	Leonard tensor
$\mathcal{P}_{ij}$	Production rate tensor
$\mathcal{P}_{k_r}$	Production rate of the residual kinetic energy
$\mathcal{R}_{ij}$	Pressure redistribution rate tensor
$\mathcal{R}e_{ij}^{sgs}$	Reynolds subgrid stress tensor
$\mathcal{T}_{ij}$	Turbulent transport rate tensor
ν	Kinematic viscosity
ν^f	Kinematic viscosity at the faces of the control volume
ν_e	Eddy viscosity
ρ	Fluid density
τ	Kolmogorov time scale
τ_w	Wall shear stress
$\tilde{\tilde{\Delta}}$	Effective filter width of combining the primary and test filter
$\tilde{\Delta}$	Filtering width of test filter

υ	Kolmogorov velocity scale
$\vec{\kappa}$	Wave number vector
$\vec{u}$	Velocity vector
$\vec{x}, \vec{r}$	Cartesian coordinates vectors
ξ	Mean free path
c	Fluid speed of sound
$E(\kappa)$	Energy spectrum
$E_{ij}(\vec{\kappa})$	Spectral tensor
$G_{\Delta_{x_f}}$	Filter function of width Δ_{x_f}
h_{wm}	Wall model thickness
k	Turbulent kinetic energy
k_f	Kinetic energy of the filtered velocity field
k_r	Residual kinetic energy
L	Characteristic length scale of fluid flow
l	Characteristic length scale of the largest eddies
L_x, L_y, L_z	Length, width and height of the computational domain
Re	Reynolds number
Re_η	Reynolds number for the smallest eddies
Re_τ	Friction velocity based Reynolds number
Re_b	Bulk velocity based Reynolds number
$R_{ij}(\vec{r})$	Spatial velocity correlation tensor
R_{ij}	Reynolds stress tensor
S_{ij}	Strain-rate tensor
T_f	Flow through time
T_{ij}	Subgrid stress tensor
U	Characteristic velocity scale of fluid flow
u	Characteristic velocity of the largest eddies
U_∞	Free flow velocity
u_τ	Friction velocity
U_b	Bulk velocity

u_{LES}	Instantaneous LES solution
u_{wm}	Wall model input velocity
W_{ij}	Spin tensor
x_1, x_2, x_3	Cartesian coordinates

Symbols

$\bar{X}$	Filtered field of X (filtered width Δ, Δ_{x_f})
$\langle X \rangle$	Average or expected value X
$\tilde{\bar{X}}$	Filtered field of X (filtered width $\tilde{\bar{\Delta}}$)
$\tilde{X}$	Filtered field of X (filtered width $\tilde{\Delta}$)
X'	Fluctuations of X with respect to the average $\langle X \rangle$
X'	Residual from the filtered field
X^+	Value of X normalized in terms of the kinematic viscosity ν and friction velocity u_τ

List of Figures

List of Tables

CHAPTER 1

Introduction

The ability to accurately predict the motion of fluids has important applications for engineers and scientists. A fundamental problem arises when fluid flows transition from laminar flow, where the flow features are contained within a small range of scales in time and space, to turbulent flow, for which the flow dynamics are spread over a large number of scales. At present, a complete description of turbulent flows is only accessible by numerically solving the fundamental equations of fluid flows. Performing such simulations, termed Direct Numerical Simulations (DNS), are still a source of major difficulties as the required computational effort increase rapidly with the Reynolds number. Hence, most real fluid flow problems, such as the flow past an aircraft or a ship's hull may not be computed with DNS. A thorough review of the challenges related to performing such high fidelity simulations may be found in Moin and Mahesh (1998). To mitigate the vast computational cost related to DNS one usually rely on simplified descriptions of the flow, such as the technique of Large Eddy Simulation (LES).

The main idea behind LES is to reduce the computational cost by only resolving the large length scales, while modeling the computationally expensive small-scale motions. Smagorinsky (1963) was the first to propose the use of LES in his study of atmospheric flows. Due to the limited computational power at the time the use of LES were for a long time restricted to the analysis of simple flow problems, such as plane channels and mixing layers (Zhiyin 2015). The advent of more modern computers in the late 1980s and early 1990s increased the CFD community's interest in LES. In the following decades several models have been developed, allowing LES to be applied in many types of real fluid flow situations. Despite the considerable progress in the development of LES the past 30 years, LES does still have several issues (Piomelli 1999; Pope 2004).

Perhaps the greatest challenge when performing LES is related to the near-wall region of attached flows. Close to walls, the turbulent flows are dominated by eddies with characteristic lengths and time scales much smaller than those of the free flow. Choi and Moin (2012) estimated that the number of grid points necessary to resolve the near wall flow is proportional to $Re^{13/7}$. Hence, the resolution requirements for Wall-Resolved LES (WRLES) is almost as high as DNS, making WRLES at high Reynolds number infeasible even with the most advanced computers.

In order to apply LES to high Reynolds number engineering applications, wall models are usually introduced. By modeling the flow in the near-wall region, one may significantly reduce the requirement for the number of grid

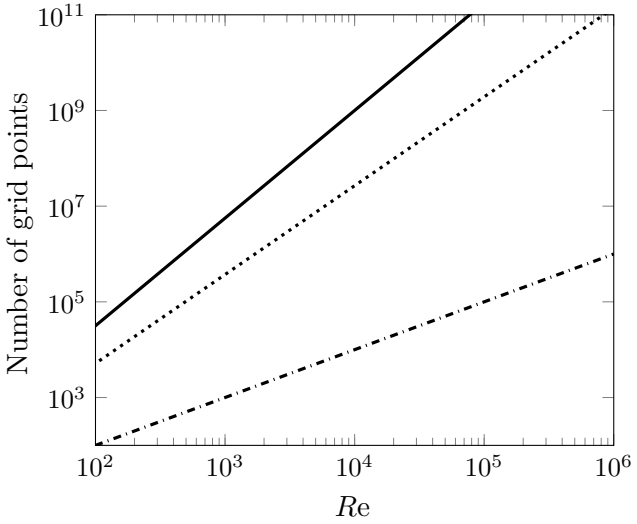

Figure 1.1: Estimated number of grid points necessary to resolve all relevant flow structures as a function of Reynolds number. (———), DNS; (·····), WRLES; (-·-·-·-) WMLES.

points, since only the larger scales in the outer region of the boundary layer needs to be resolved. The estimated resolution requirement of Wall-Modeled LES (WMLES) grows linearly with increasing Reynolds number (S. T. Bose and Park 2018), and WMLES is therefore an attractive alternative from a computational point of view. The approximate number of grid cells needed to perform DNS, WRLES and WMLES are illustrated in Figure (1.1).

Following the taxonomy of Larsson et al. (2016), the wall model approaches can be classified as hybrid LES/RANS method, where the near-wall region is computed by solving the Reynolds Average Navier-Stokes (RANS) equations interfaced to a LES region at some distance y_{int} above the wall, or as a pure LES formulation where the LES equations extend all the way down to the solid boundary. In the latter formulation, one usually introduces Neumann boundary condition in terms of the wall shear stress, τ_w, obtained by solving a wall model over a layer with thickness h_{wm}. Larsson et al. (2016) and Piomelli and Balaras (2002) provide a thorough discussion of both approaches.

The first attempt to implement a model for the wall layer was made by Deardorff (1970) for an LES of a plane channel flow at infinite Reynolds number. However, the results obtained did not agree well with experimental measurements. Assuming the wall shear stress to be in phase with the velocity at the first off-wall grid point, Schumann (1975) derived what is now considered the first standard wall model. This model performed much better than Deardorff's original attempt of WMLES. In the decades following U. Schumann's publication, several improved wall models have been developed, such as the methods proposed by Piomelli, Ferziger et al. (1989) and S. Bose and Moin (2014). Significant research effort is still aimed at this topic and recent reviews can be found in Larsson et al. (2016) and S. T. Bose and Park (2018). The development of suitable wall models is, however, a challenging task and as pointed out by Piomelli (2008) "despite the increased attention to the problem, no universally

accepted model has appeared".

The scope of this thesis is inspired by the work of X. I. Yang, Park and Moin (2017) and Kawai and Larsson (2012), both of have contributed greatly to the study of Wall Modeled Large Eddy Simulation. The main goal is to implement and verify different wall modeling strategies and their suitability for different mesh topologies. The results will be verified by comparing the results to DNS data available in the literature. Since this is a quite broad scope of work, the present study is limited to a single test case, namely a fully-developed turbulent channel flow with constant pressure-gradient.

The thesis is divided into 7 chapters, including the introduction. The contents of the remaining chapters are briefly outlined below.

- **Chapter 2** is devoted to the concept of turbulence. The chapter starts by introducing the phenomenon and the main characteristics of turbulent fluid flows. Next, the mathematical tools used in the theoretical analysis of turbulent flows together with some characteristics of such flows are presented. Thereafter, the concept of boundary layers and their extension to turbulent flows is introduced.

- **Chapter 3** focuses on applied turbulence models. The chapter present the governing equations of fluid flow and derive both the Reynolds Averaged Navier-Stokes and Filtered Navier-Stokes equations, and give a short description of their physical characteristics. Lastly, the concept of wall modelling, focusing on the algebraic wall model, is introduced.

- **Chapter 4** outlines specifics of the problem studied in the thesis. Aspects of the computational domain, grid topology and boundary conditions are presented. The treatment of solid boundaries are described in detail and we conclude the chapter with some general remarks regarding the implementation of the boundary conditions.

- **Chapter 5** presents the results obtained using the different wall modeling strategies. The chapter focuses on the quantitative validation with reference to existing DNS data.

- **Chapter 6** seeks to explain how grid topology, wall modelling strategy and eddy viscosity affect the near wall behavior of the WMLES solution and why they affect the magnitude of LLM.

- **Chapter 7** concludes the findings of the thesis and outline recommendations for further work.

PART I

Theory

CHAPTER 2

Introduction to Turbulence

2.1 The Physics of Turbulence

The phenomenon of turbulent fluid motion is all around us, and almost everyone have experienced hitting an extra rough patch of air on their way to their next vacation. Still physicists and mathematicians do not agree on a universal definition of the phenomenon. There are, however, a general agreement that turbulence involves the complex, chaotic motion of a fluid.

Osborne Reynolds was the first to show that the distinction between laminar and turbulent flow depends upon the relative magnitude of the viscous and inertia forces (Jackson and Launder 2007). This relationship is usually represented in terms of the dimensionless Reynolds number, Re, as defined in Equation (2.1).

$$Re = \frac{UL}{\nu} \tag{2.1}$$

Here, U denotes the characteristic velocity, L is the characteristic length scale of the flow, and ν the fluid kinematic viscosity. The key characteristic of turbulent flow is that the flow is dominated by three-dimensional time dependent swirling flow structures, known as turbulent eddies. These structures occur over a vast range of time and length scales, the largest being proportional to the flow field itself. The size of the smallest eddies was for a long time disputed. In his famous paper from 1941, Kolmogorov postulated that only two quantities, the kinematic viscosity and the mean dissipation rate, ϵ, characterize the small-scale motion of a fully developed turbulent flow (Tennekes 1972). From this assumption, he derived the now well known Kolmogorov microscales of length η, time τ, and velocity υ for the smallest turbulent structures, presented in the Equation (2.2).

$$\eta = \left(\frac{\nu^3}{\epsilon}\right)^{\frac{1}{4}}, \qquad \upsilon = (\nu\epsilon)^{\frac{1}{4}}, \qquad \tau = \left(\frac{\nu}{\epsilon}\right)^{\frac{1}{2}} \tag{2.2}$$

Introducing the Kolmogorov length and velocity scale into the expression for the Reynolds number yields Equation (2.3).

$$Re_\eta = \frac{\upsilon\eta}{\nu} = (\nu\epsilon)^{\frac{1}{4}}\left(\frac{\nu^3}{\epsilon}\right)^{\frac{1}{4}}\frac{1}{\nu} = \frac{\epsilon^{\frac{1}{4}}\nu}{\epsilon^{\frac{1}{4}}\nu} = 1 \tag{2.3}$$

The Reynolds number for the small scale eddies are of order 1. The small-scale motions are thus dominated by viscosity, and the kinetic energy contained in these eddies are rapidly dissipated by viscous heating.

One important consequence of the Kolmogorov scale is the fact that the smallest eddies typically are significantly larger than the scale of molecular motion. Hence, turbulence is a continuous phenomenon. A pertinent example is the motion of the Earth's atmosphere. Here the dissipation rate and kinematic viscosity is of order $10\text{cm}^2/\text{s}^3$ and $0.1\text{cm}^2/\text{s}$ respectively, while the mean free path ξ is in the order of 10^{-4}cm. From Equation (2.2), one may estimate the ratio ξ/η as shown below.

$$\frac{\xi}{\eta} = \xi\left(\frac{\epsilon}{\nu^3}\right)^{\frac{1}{4}} \approx \frac{1}{1000} \tag{2.4}$$

The smallest eddies are several orders of magnitude larger than the molecular scales and the small-scale eddies can be assumed to operate in a continuum. For a more thorough discussion of the validity of the continuum hypothesis for turbulent flows, consult R. D. Moser (2006).

Taylor (1935) postulated that the rate of viscous dissipation of the small-scale eddies can be approximated from the large-scale dynamics, for which viscosity is negligible, according to Equation (2.5).

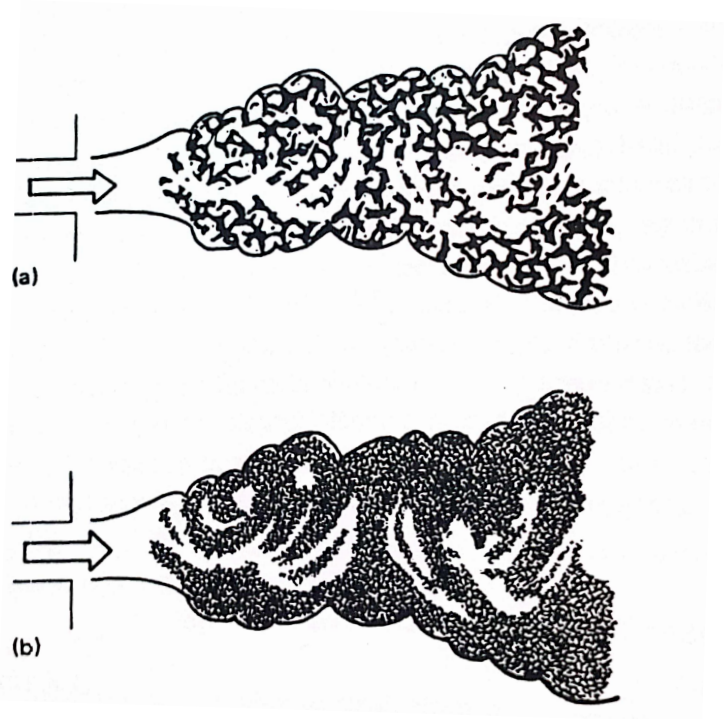

Figure 2.1: Turbulent flows at different Reynolds numbers. (a) jet flow at a relative low Reynolds number, (b) similar flow but at a higher Reynolds number (Tennekes 1972).

$$\epsilon \propto \frac{u^3}{l} \tag{2.5}$$

Here, u and l represent the velocity and length scales of the largest eddies respectively. Substituting the above relation into the expressions for the Kolmogorov microscales, we obtain relations for the relative size of the small- and large-scale eddies. These relations indicate that the time, length and velocity scales of the small eddies are significantly smaller than that of the larger scales. The gap widens with increasing Reynolds number as expressed in Equation (2.6).

$$\frac{\eta}{l} \propto Re^{-\frac{3}{4}}, \qquad \frac{\upsilon}{u} \propto Re^{-\frac{1}{4}}, \qquad \frac{\tau}{t} \propto Re^{-\frac{1}{2}}, \tag{2.6}$$

In light of Equation (2.6), it follows that the main characteristic differentiating turbulent flows at different Reynolds numbers, everything else being equal, is the size of the smaller eddies. This is illustrated in Figure (2.1).

Another characteristic of turbulent flows is the enhanced transport of mass and momentum. The transfer rate being several orders of magnitude larger than what is observed for laminar flows.

2.2 The Stochastic Description of Turbulence

In a turbulent flow, the velocity u at any given point varies in a seemingly random manner, as illustrated in Figure (2.2). Here, we observe a typical measurement of a velocity component captured by a hot wire at a given location within the flow. This raises the question, how can deterministic equations such as the Navier-Stokes have a stochastic nature? The answer is two-fold. First, turbulent flows are chaotic processes. That is, an aperiodic system which exhibits extreme sensitivity to small perturbations in the initial and boundary conditions

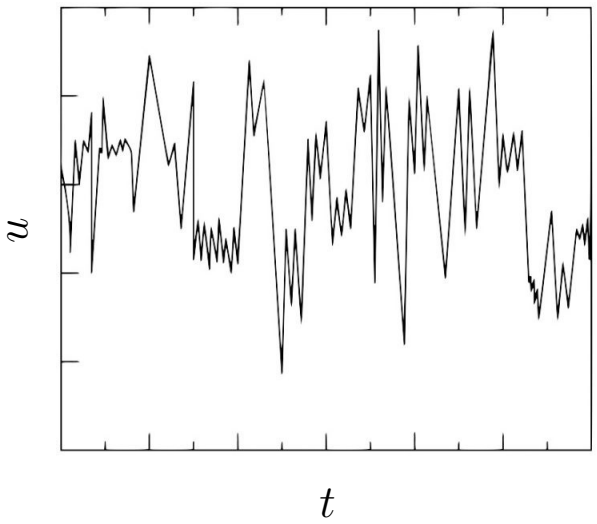

Figure 2.2: Typical velocity signal of a single component of velocity in turbulent flow measured at a given location.

(Strogatz 2015). Secondly, even though one may reduce the presence of such perturbations, one cannot remove them entirely. Unavoidable perturbations in the initial conditions, boundary conditions and material properties make it impossible to predict the state of the system over any significant amount of time. Thus, one usually reduces the description of turbulence to the various statistical moments since these properties are quite reproducible.

Probability Density Function and Moments

A turbulent flow parameter, such as the flow velocity $\vec{u}$, is fully characterized at a given location in time and space by its Probability Density Function (PDF). Letting $f(X)$ denote the PDF of an arbitrary turbulent variable X, then the n^{th} moment of the variable X is defined as Equation (2.7) below.

$$\langle X^n \rangle = \int_{-\infty}^{\infty} X^n f(X)\,\mathrm{d}X \tag{2.7}$$

Even though there is no limit to the number of moments one might examine, one generally limits the study of turbulence to the lowest non-zero moment of the stochastic variable. The first moment of any turbulent variable X, usually referred to as the mean or expected value of X, is defined in Equation (2.8) below.

$$\langle X \rangle = \int_{-\infty}^{\infty} X f(X)\,\mathrm{d}X \tag{2.8}$$

Following the excellent work by O. Reynolds one usually decompose the turbulent quantities into a stochastic mean and a fluctuating part, $X = \langle X \rangle + X^{'}$ (Reynolds 1995). This procedure is known as Reynolds decomposition. By design the mean value of the fluctuating part is exactly zero, $\langle X^{'} \rangle = 0$. However, this is generally not true for the higher order moments of $X^{'}$. Thus, the properties of the fluctuating fields are usually presented in terms of the second moment, computed according to Equation (2.9).

$$\begin{aligned} \langle X^{'} X^{'} \rangle &= \Big\langle \big(X - \langle X \rangle\big)\big(X - \langle X \rangle\big) \Big\rangle \\ &= \Big\langle X^2 - 2X\langle X \rangle + \langle X \rangle \langle X \rangle \Big\rangle \\ &= \langle X^2 \rangle - \langle X \rangle \langle X \rangle \end{aligned} \tag{2.9}$$

The random variables describing turbulent flows are not independent. Thus, the joint statistical properties of turbulent flow parameters are included in the stochastic description of turbulence in the form of their covariance. Letting X and Y denote two random variables, the second moment of the fluctuating part of X and Y is calculated according to Equation (2.10).

$$\begin{aligned} \langle X^{'} Y^{'} \rangle &= \Big\langle \big(X - \langle X \rangle\big)\big(Y - \langle Y \rangle\big) \Big\rangle \\ &= \Big\langle \big(XY + \langle X \rangle Y + \langle Y \rangle X - \langle X \rangle \langle Y \rangle\big) \Big\rangle \\ &= \langle XY \rangle - \langle X \rangle \langle Y \rangle \end{aligned} \tag{2.10}$$

Assumption of Turbulent Flows

Formally, the PDF's of turbulent quantities are constructed from an ensemble of n independent realizations of the turbulent flow. In practice, this is a daunting task as this requires the experiment, physically or numerically, to be performed repeatedly. Therefore, one usually assume the principle of ergodicity to be valid (Sagaut 2006). That is, all stochastic properties can be deduced from a single, sufficiently long, realization. As a consequence one assumes the statistical properties of turbulent flows to be stationary, i.e. all moments of the turbulent quantities are time independent.

The added complexity introduced by the fluctuations superimposed onto the fluid motion makes theoretical study of turbulence a challenging task. One therefore frequently assumes that turbulent flows are homogeneous. That is, the mean quantities are assumed invariant under any spatial translation. Further, one commonly assumes all probabilistic quantities to be invariant under any arbitrary rotation of the frame of reference, this assumption being commonly referred to as isotropic turbulence. It should however be noted that isotropic homogeneous turbulence is an idealization of true turbulent flows rarely encountered in nature.

Correlations and Spectra

Even though one may extract a lot of useful information about the turbulent variables from their PDF's and their moments. They do not, in general, give a complete description of the random processes of a turbulent flow. For example, they do not contain any information about the interaction of turbulent quantities at two or more locations. The simplest extension of the stochastic analysis of turbulence is by way of two-point correlation. The correlation can be at different points in time (usually referred to as auto-correlation) or in space. Let $\vec{x}$ and $\vec{x}+\vec{r}$ be two points in space. Then the spatial velocity correlation tensor $R_{i,j}(\vec{r})$ is defined according to (2.11).

$$R_{i,j}(\vec{r}) = \left\langle u_i(\vec{x}), u_j(\vec{x}+\vec{r}) \right\rangle \tag{2.11}$$

Since turbulence spans a vast range of eddy sizes, it is convenient to take the Fourier transform of $R_{i,j}(\vec{r})$ to consider the statistical properties at different wave numbers. Taking the Fourier transform of Equation (2.11) we obtain the spectral tensor $E_{i,j}$ as a function of the wave number vector $\vec{\kappa}$.

$$E_{i,j}(\vec{\kappa}) = \frac{1}{(2\pi)^3} \int R_{i,j}(\vec{r}) e^{-i\vec{\kappa}\vec{r}} \, \mathrm{d}^3\vec{r} \tag{2.12}$$

$E_{i,j}(\vec{\kappa})$ describes the direction and magnitude of the kinetic energy of all scales present in the flow. Usually the information about the direction is of less interest and is often removed by considering the energy at a particular scale $\kappa = |\vec{\kappa}|$. We obtain $E(\kappa)$, called the energy spectrum, by integrating the half trace of the spectral tensor over a sphere with radius $|\vec{\kappa}|$ (Sagaut 2006).

$$E(\kappa) = \frac{1}{2} \int_{\kappa=|\vec{\kappa}|} E_{i,i}(\vec{\kappa}) \, \mathrm{d}A \tag{2.13}$$

We note that the energy spectrum $E(\kappa)$ is a real and positive function. Further, the spectrum is related to the total turbulent kinetic energy k and the

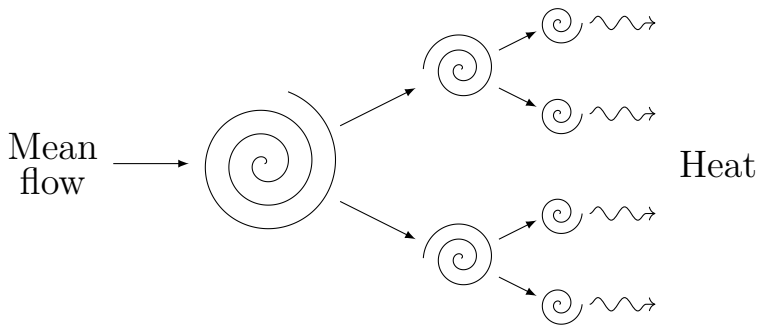

Figure 2.3: Illustration of the energy cascade. Kinetic energy is transferred from the mean flow to the large eddies. Energy is further transferred to the smaller eddies, before being dissipated in to heat.

total dissipation ϵ according to Equation (2.14) (Pope 2000).

$$k = \int_0^\infty E(\kappa)\,\mathrm{d}\kappa \qquad\qquad \epsilon = \int_0^\infty \nu\kappa^2 E(\kappa)\,\mathrm{d}\kappa \tag{2.14}$$

In general, for fully developed turbulence at high Reynolds numbers the bulk of turbulent energy is contained in the large-scale turbulent structures with wave number $\kappa \approx l^{-1}$. By means of the nonlinear interaction, the energy is transferred through an energy-cascade for which turbulent kinetic energy is distributed from the large to the small-scale motions, as illustrated in Figure (2.3). Moving down this cascade, towards the high wave number structures, the viscous dissipation increases gradually. Peak dissipation occurring for $\kappa \approx \kappa_\eta$, where $\kappa_\eta = \eta^{-1}$ denotes the Kolmogorov wave number. For higher wave numbers, the energy spectrum rapidly drops to zero (Phillips 1991).

Assuming the turbulence to be locally homogeneous and isotropic Kolmogorov concluded that the energy spectrum could be fully expressed in terms of the energy dissipation rate, the kinematic viscosity and the wave number (Kolmogorov 1991).

$$E = E(\kappa, \epsilon, \nu) \tag{2.15}$$

For $\kappa >> l^{-1}$ the spectrum is almost isotropic and in general equilibrium, and is usually referred to as the equilibrium range. Excluding the energy contribution from the smallest structures of the equilibrium range one obtain the inertial subrange, for which $\kappa_\eta >> \kappa >> l^{-1}$. The turbulent energy contained in this part of the energy spectrum is not affected by viscosity. Using Equation (2.15) as an ansatz, Kolmogorov derived the now well-known Kolmogorov spectrum presented in Equation (2.16) through dimensional analysis, valid for the inertial subrange.

$$E(\kappa) = \alpha\epsilon^{\frac{2}{3}}\kappa^{-\frac{5}{3}} \tag{2.16}$$

Here α denote the universal Kolmogorov number. For the smallest length scales, where viscosity is of importance, Equation (2.16) does not provide a good fit compared with real life turbulence spectra. Several improved spectra, such as Equation (2.17) proposed by Kovasznay (1948), have been suggested

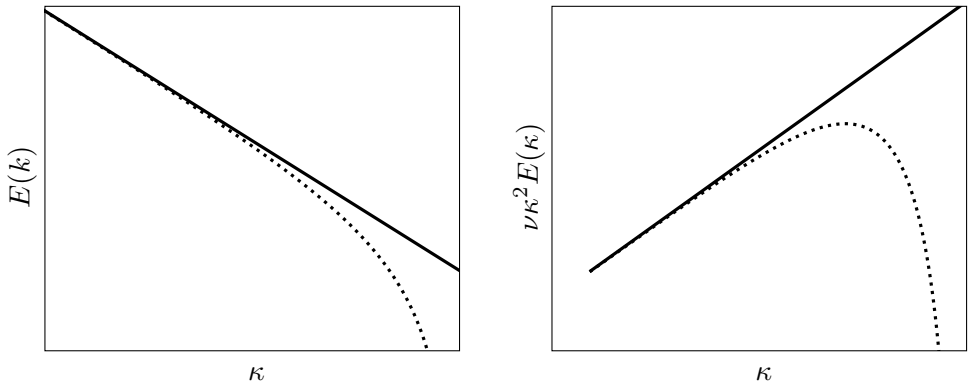

Figure 2.4: Theoretical turbulence energy spectra and dissipation spectra for the equilibrium range. (———), Kolmogorov spectrum; (·····), Kovasznay (1948).

after Kolmogorov introduced his original spectrum. Both spectra and their respective dissipation rate, $\epsilon = \nu\kappa^2 E(\kappa)$, are illustrated in Figure (2.4).

$$E(\kappa) = \beta\epsilon^{\frac{2}{3}}(\kappa\eta)^{-\frac{5}{3}}\left(1-(\kappa\eta)^{\frac{4}{3}}\right)^2 \tag{2.17}$$

2.3 Boundary Layer Theory

In the absence of solid boundaries, the effect of viscosity becomes negligible compared to inertia and pressure forces for sufficiently high Reynolds numbers. By removing the effect of viscosity, one greatly simplifies the mathematical problem of fluid motion (Çengel and Cimbala 2014). However, the inviscid flow solution does not satisfy the no-slip boundary condition at solid boundaries. That is, the relative velocity component tangential to the wall does not vanishes at the wall. Thus, the non-viscous flow equations often yield non-physically results such as zero shear stress along solid boundaries. Since there existed only a few solutions to the equations of viscous fluids, researchers have had to rely on experiments to study most real fluid flows. This changed with the introduction of boundary layer theory.

The existence of a boundary layer was first proposed by Ludwig Prantl in 1904 (Tulapurkara 2005). The idea behind boundary layer theory is that high Reynolds number flows can be split into two sub regions. The bulk region, for which the effect of viscosity can be ignored, referred to as the outer layer; the second region is a thin layer close to any solid boundary where the effect of viscosity cannot be neglected. Since the transition from one region to another is gradual, there exists no clear definition of the boundary layer thickness δ. However, at least for laminar boundary layers, one frequently defines the edge of the boundary layer as the point where the velocity has reached 99% of the free flow velocity U_∞ (Çengel and Cimbala 2014).

H. Blasius derived the first solution of a two-dimensional laminar boundary layer over a flat plate, as illustrated in Figure (2.5). Assuming the streamwise pressure gradient to be zero, he showed that Prantl's boundary layer equations has the solution presented in Equation (2.18) (White 2006).

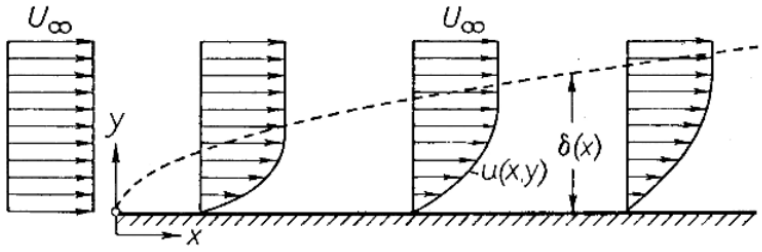

Figure 2.5: Illustration of a boundary layer over a flat plate (Schlichting and Gersten 2016).

$$u = U_\infty \frac{df}{d\eta}, \quad v = \sqrt{\frac{\nu U_\infty}{2x}}\left(\frac{df}{d\eta} - f\right) \tag{2.18}$$

Here, u and v denotes the wall parallel and wall normal velocity component. Further, η denotes the dimensionless similarity variable defined in Equation (2.19) below.

$$\eta = y\sqrt{\frac{U_\infty}{2\nu x}} \tag{2.19}$$

The function $f = f(\eta)$ is the solution to the third order differential equation (2.20), known as the Blasius equation.

$$\frac{d^3 f}{d\eta^3} + f\frac{d^2 f}{d\eta^2} = 0 \tag{2.20}$$

To date an exact analytical solutions to the Blasius equation does not exist. Approximate analytic solutions may be obtained as a series expansion combined with a suitable matching condition of an inner and outer solution, as done by Blasius himself, or by means of numerical computations. Falkner and Skan (1931) extended the similarity solution proposed by Blasius by accounting for the effect of non-zero streamwise pressure gradients. In their equation for the function f (Eq. (2.21)) the effect of dp/dx is measured by the parameter β. Negative β implies an adverse pressure gradient, while positive values denote a favorable pressure gradient (White 2006).

$$\frac{d^3 f}{d\eta^3} + f\frac{d^2 f}{d\eta^2} + \beta\left(1 - \frac{df}{d\eta}^2\right) = 0 \tag{2.21}$$

The concept of a boundary layer was extended to turbulent flows in the late 1920s and early 1930s (Tani 1977). Due to the increased exchange of momentum caused by the turbulent eddies, Turbulent Boundary Layers (TBL) involve larger velocity gradients close to the wall, resulting in a *fuller* velocity profile compared to laminar boundary layers. Further, the additional mixing caused by the turbulent motion is an important source of friction drag encountered by aircrafts and ships' hulls and turbulent flows through ducts and pipes.

A striking difference between TBLs and their laminar counterparts, is that viscosity only affect a small fraction of the actual boundary layer (Schlichting

and Gersten 2016). TBLs are thus usually divided into two regions. A thin layer directly at the wall referred to as the *inner region*, where the viscous contribution to the shear stress is significant, and the *outer region* where the apparent friction is due to the turbulent transport of momentum. The mean velocity profile of a typical TBL is presented in Figure (2.6).

One should note that even though we divide TBLs into different regions, they act as a continuum. At high Reynolds numbers, energy flows from the mean flow to the larger eddies in the outer region. On the other hand, Klebanoff (1955) showed that the bulk of dissipation, both viscous and turbulent, takes place in the inner region. Hence, there must be a constant exchange of turbulent energy form the outer to the inner region.

Due to the complex nature of the turbulent fluctuations, there exist no analytic solution to Prantl's boundary layer equations for turbulent flows. The shape of the velocity profile and other properties of turbulent boundary layers are thus obtained from experiments, physical or numerical, or from semi-empirical expressions. One of the simplest empirical models for the mean velocity profile is the *One-Seventh-Power Law* originally presented by Prandtl (1925). Von Karman (1931) postulated that the velocity profile of a turbulent boundary layer could be described as a logarithmic function of the off-wall distance, commonly called the *Log-Law*. Comparing the *Log-Law* with measurements obtained from direct numerical simulation (Spalart 1988) and experiments (Klebanoff 1955) of turbulent boundary layers shows that the log-profile is valid over a significant portion of the turbulent boundary layer. This portion of the boundary layer is thus called the *Log-Layer*. However, discrepancies are observed in the vicinity

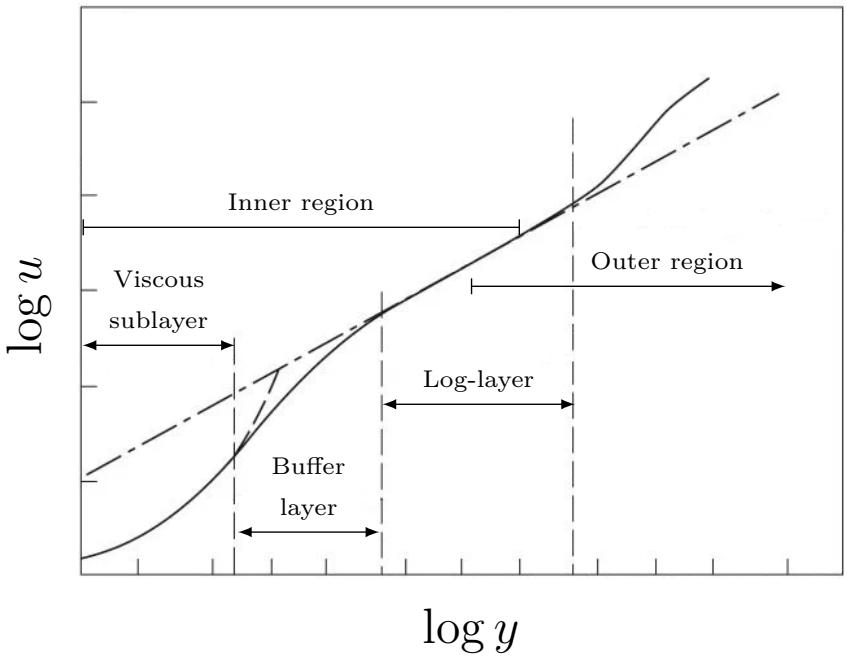

Figure 2.6: Illustration of a the mean velocity in a typical turbulent boundary layer. The relative position of the different layers and regions are indicated.

of the wall, where the velocity increases linearly (Pope 2000). In this linear region, the effect of turbulence is negligible compared with viscous stresses, hence called the *viscous sublayer*. Additionally, the Log-Law deviates from the correct velocity profile at the edge of the boundary layer.

Spalding (1961) created an improved expression for the mean velocity profile. The so-called *Spadlings' Law of The Wall* fits experimental measurements nicely. Both in the *viscous sublayer* and the *Log-Layer*, as well as the transitional *Buffer-region* connecting the two layers (see Figure (2.6)). However, as for the *Log-Law*, it is not valid in the outer region. By studying a large set of boundary layer data, Coles (1956) introduced the *Wake function*, which represents the mean velocity in the outer region. By combining this function with the *Log-Law*, he derived the *Wall-Wake-Law* valid over the whole boundary layer.

CHAPTER 3

Turbulence Modeling

The flow of an incompressible Newtonian fluid is governed by the Navier-Stokes equations and the continuity equation. In their primitive form they are formulated in terms of velocity $\vec{u} = (u_1, u_2, u_3)$ and static pressure $p = P/\rho$. Expressed in Cartesian coordinates $x = (x_1, x_2, x_3)$, the Navier-Stokes and continuity equations are defined as shown in (3.1) and (3.2). In (3.1), it is assumed that the kinematic viscosity is constant. Following the Einstein summation convention, repeated indices imply summation over $1, 2$ and 3.

$$\frac{\partial u_i}{\partial t} + \frac{\partial u_i u_j}{\partial x_j} = -\frac{\partial p}{\partial x_i} + \nu \frac{\partial^2 u_i}{\partial x_j \partial x_j} \tag{3.1}$$

$$\frac{\partial u_i}{\partial x_i} = 0 \tag{3.2}$$

Even though the existence of a unique solution of the Navier-Stokes equations is yet to be proven, numerical simulations are consistent with experimental results, and have become an important tool for scientists and engineers.

The estimated number of grid points necessary to resolve all scales present in a turbulent flow is proportional to $Re^{9/4}$. Hence, Direct Numerical Simulations (DNS) of the Navier-Stokes equations is often unfeasible due to the computational cost required to perform such simulations. In order to overcome this problem, one usually introduces a coarser level description of the flow while modeling the interaction between the resolved and non-resolved scales.

Multiple turbulence models exist today. The most common methods belong to one of two classes: Reynolds-Averaged Navier-Stokes (RANS) and Large Eddy Simulation (LES). The former method is outlined in section (3.1), followed by a description of the core concepts of LES preformed in physical space (Section (3.2)).

3.1 Reynolds Average Naiver-Stokes

Following the concept of Reynolds decomposition, we decompose the primitive variables into a slowly varying mean ($\langle . \rangle$) and a fluctuating part($.^{'}$), according to Equation (3.3).

$$u_i = \langle u_i \rangle + u_i^{'}, \quad p = \langle p \rangle + p^{'} \tag{3.3}$$

Here $\langle . \rangle$ denotes the ensemble average of the velocity and pressure field. We further assume that the primitive variables obey the Reynolds averaging rules summarized below (Tennekes 1972).

$$\langle u_i^{'} \rangle = 0, \quad \Big\langle \langle u_i \rangle u_i^{'} \Big\rangle = \langle u_i \rangle \langle u_i^{'} \rangle = 0 \tag{3.4}$$

Substituting Equation (3.3) into Equation (3.1), taking the ensemble average and enforcing the Reynolds averaging rules we obtain the Reynolds Average Navier-Stokes equation (RANS) (Speziale 1991).

$$\frac{D\langle u_i \rangle}{Dt} = -\frac{\partial \langle p \rangle}{\partial x_i} + \nu \frac{\partial^2 \langle u_i \rangle}{\partial x_j \partial x_j} - \frac{\partial \langle u_i^{'} u_j^{'} \rangle}{\partial x_j} \tag{3.5}$$

The substantial derivative on the left of Equation (3.5) is defined as $D/Dt = \partial/\partial t + \langle u_j \rangle \partial/\partial x_j$. Similarly, one may derive the continuity equation for the mean velocity given in Equation (3.6).

$$\frac{\partial \langle u_i \rangle}{\partial x_i} = 0 \tag{3.6}$$

Equations (3.5) and (3.6) do not form a closed system for the dependent variables $\langle u_i \rangle$ and $\langle p \rangle$. The closure problem of the Reynolds Averaged Navier–Stokes equations have been discussed by several authors (Speziale 1991; Pope 2000).

The last term on the left hand side of (3.5), namely $\partial \langle u_i^{'} u_j^{'} \rangle / \partial x_j$, is the only term distinguishing the RANS equations from its laminar counterpart. Mathematically, this term is equivalent to the stress term. Hence, $\langle u_i^{'} u_j^{'} \rangle$ is usually referred to as the Reynolds stress tensor. Consequently, the effect of the turbulent motions is to add additional "stresses" to what are otherwise the same equations that govern laminar flow. One should note that they are not stresses but are instead additional momentum fluxes due to the turbulent motions. As this is the sole contribution of the turbulent fluctuations to the mean motion, it is useful to derive the transport equation for the individual Reynolds stresses. Following Speziale (1991), we first define the operator $\mathcal{L}$ according to Equation (3.7).

$$\mathcal{L}(u_i^{'}) = \frac{Du_i^{'}}{Dt} + u_j^{'} \frac{\partial \langle u_i \rangle}{\partial x_j} + \frac{\partial p^{'}}{\partial x_i} - \nu \frac{\partial^2 u_i^{'}}{\partial x_j \partial x_j} + \frac{\partial u_i^{'} u_j^{'} - \langle u_i^{'} u_j^{'} \rangle}{\partial x_j} \tag{3.7}$$

Using Equation (3.7) as an ansatz and applying the chain rule, we may derive the transport equation of the second moment $\langle u_i^{'} u_j^{'} \rangle$.

$$\mathcal{L}(\langle u_i^{'} u_j^{'} \rangle) = \langle u_j^{'} \mathcal{L}(u_i^{'}) \rangle + \langle u_i^{'} \mathcal{L}(u_j^{'}) \rangle \tag{3.8}$$

More explicitly, the Reynolds-stress transport equation (3.8) is given by Equation (3.9) (Mansour, Kim and Moin 1988).

$$\begin{aligned} \frac{D}{Dt}\langle u_i^{'} u_j^{'} \rangle = &- \Big(\langle u_j^{'} u_k^{'} \rangle \frac{\partial \langle u_i \rangle}{\partial x_k} + \langle u_i^{'} u_k^{'} \rangle \frac{\partial \langle u_j \rangle}{\partial x_k} \Big) - \Big(\Big\langle u_i^{'} \frac{\partial p^{'}}{\partial x_j} \Big\rangle + \Big\langle u_j^{'} \frac{\partial p^{'}}{\partial x_i} \Big\rangle \Big) \\ &- 2\nu \Big\langle \frac{\partial u_i^{'}}{\partial x_k} \frac{\partial u_j^{'}}{\partial x_k} \Big\rangle - \frac{\partial \langle u_i^{'} u_j^{'} u_k^{'} \rangle}{\partial x_k} + \nu \frac{\partial^2 \langle u_j^{'} u_i^{'} \rangle}{\partial x_k \partial x_k} \end{aligned} \tag{3.9}$$

The terms on the right-hand side of the Equation (3.9) are identified as (Mansour, Kim and Moin 1988)

$$\mathcal{P}_{ij} = -\Big(\langle u_j^{'} u_k^{'}\rangle \frac{\partial\langle u_i\rangle}{\partial x_k} + \langle u_i^{'} u_k^{'}\rangle \frac{\partial\langle u_j\rangle}{\partial x_k}\Big) \qquad \text{Production rate}$$

$$\mathcal{R}_{ij} = \Big(\Big\langle u_i^{'} \frac{\partial p^{'}}{\partial x_j}\Big\rangle + \Big\langle u_j^{'} \frac{\partial p^{'}}{\partial x_i}\Big\rangle\Big) \qquad \text{Pressure redistribution rate}$$

$$\mathcal{E}_{ij} = 2\nu\Big\langle \frac{\partial u_i^{'}}{\partial x_k} \frac{\partial u_j^{'}}{\partial x_k}\Big\rangle \qquad \text{Viscous dissipation rate}$$

$$\mathcal{T}_{ij} = -\frac{\partial\langle u_i^{'} u_j^{'} u_k^{'}\rangle}{\partial x_k} \qquad \text{Turbulent transport rate}$$

$$\mathcal{D}_{ij} = \nu \frac{\partial^2\langle u_j^{'} u_i^{'}\rangle}{\partial x_k \partial x_k} \qquad \text{Viscous diffusion rate}$$

The effect of $\mathcal{T}_{ij}$ and $\mathcal{D}_{ij}$ is to redistribute turbulent energy in space. The effect of $\mathcal{P}_{ij}$ and $\mathcal{E}_{ij}$ becomes evident by taking the half trace of the Reynolds-stress equation, which yields the transport equation of turbulent kinetic energy $k = 1/2\langle u_i^{'} u_i^{'}\rangle$ presented in Equation (3.10).

$$\frac{Dk}{Dt} + u_k^{'} \frac{\partial k}{\partial x_k} + \Big\langle u_i^{'} \frac{\partial p^{'}}{\partial x_i}\Big\rangle - \nu \frac{\partial^2 k}{\partial x_k \partial x_k} = -\langle u_i^{'} u_k^{'}\rangle \frac{\partial\langle u_i\rangle}{\partial x_k} - \nu\Big\langle \frac{\partial u_i^{'}}{\partial x_k} \frac{\partial u_i^{'}}{\partial x_k}\Big\rangle \quad (3.10)$$

The first term on the right hand side stems from the production tensor $\mathcal{P}_{ij}$. This term is in general negative and it thus works as a source of turbulent kinetic energy (Pope 2000). The half trace of $\mathcal{E}_{ij}$ reduce to the second term on the right of Equation (3.10). Since the term is obviously non-negative it can only reduce the amount of turbulent kinetic energy present in the flow, and hence it operates as a sink in the transport equation for k.

The redistributive properties of $\mathcal{R}_{ij}$ is easily revealed by considering fully developed homogeneous turbulence, for which the Reynolds-stress equation reduces to Equation (3.11) below.

$$0 = \mathcal{P}_{ij} - \mathcal{R}_{ij} - \mathcal{E}_{ij} \quad (3.11)$$

Examining the above transport equation for the normal stresses $\langle u_1^{'} u_1^{'}\rangle, \langle u_2^{'} u_2^{'}\rangle$ and $\langle u_3^{'} u_3^{'}\rangle$ one observe that the only non zero production term is located in the equation for $\langle u_1^{'} u_1^{'}\rangle$. Hence the only net source of turbulent kinetic energy is $\langle u_1^{'} u_1^{'}\rangle$. As $\mathcal{P}_{22} = \mathcal{P}_{33} = 0$, there is no production in the budgets of $\langle u_2^{'} u_2^{'}\rangle$ and $\langle u_3^{'} u_3^{'}\rangle$. However, in homogeneous turbulence, it follows from the continuity equation that the trace of $\mathcal{R}_{ii}$ is exactly zero (Pope 2000). Thus $-\mathcal{R}_{11} = \mathcal{R}_{22} + \mathcal{R}_{33}$, consequently the pressure term serves to redistribute turbulent kinetic energy from the most energetic Reynolds stresses to the smaller stresses.

3.2 Large Eddy Simulation

In Large Eddy Simulation, one resolves the large three-dimensional unstable turbulent motions, which contain most of the fluid kinetic energy, while modeling

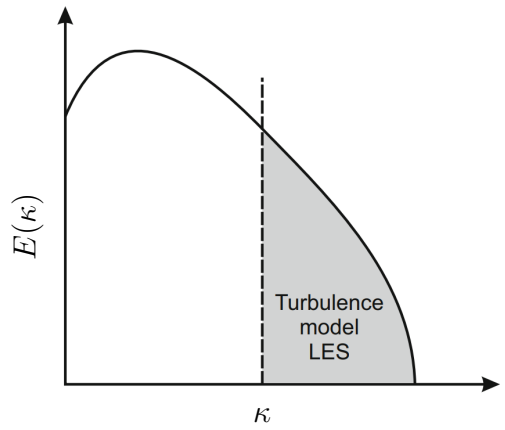

Figure 3.1: Sketch of the energy distribution in a turbulent flow as a function of wave number and the range for which turbulent motions are modeled using LES (Imtiaz and Akhtar 2019).

the remaining smaller structures down to the Kolmogorov scales, as illustrated in Figure (3.1). As the method resolves the large-scale turbulent motion, it is expected to be more accurate than RANS-models for flows where large scale turbulence is significant. However, as one omits resolving the smaller scales (which are assumed to have a more universal behavior and are thus easier to model) LES has a reduced computational cost compared to DNS. Based on this, LES should theoretically produce high fidelity data at a reduced computational cost.

Filtering

A common way to derive the theoretical model for the LES problem is to apply a low-pass spatial filter to the momentum (Eq. (3.1)) and continuity (Eq. (3.2)) equations. The true solution is then approximated by a velocity field $\bar{u}$ and pressure field $\bar{p}$, which represent the solution of the filtered equations. As all small-scale motions are removed from the resulting velocity and pressure field, the filtered equations can be solved accurately on a relatively coarse grid. Following Leonard (1975), we derive the filtered momentum and continuity equations by applying a low-pass spatial filter, in the form of a convolution product, to Equations (3.1) and (3.2). Letting $G_{\Delta x_f}(x)$ represent an arbitrary filter function of width Δx_f, then the filtered field of any quantity $\phi(\vec{x}, t)$ are obtained according to Equation (3.12).

$$\bar{\phi} = \int \phi(\vec{y}, t) G_{\Delta x_f}(|\vec{x} - \vec{y}|)\, \mathrm{d}\vec{y} \tag{3.12}$$

The filter function in Equation (3.12) is expressed as a function of space only, as these are the most commonly used in LES. However, temporal filtered LES has also been presented (Pruett 2007). To derive the filtered equations the applied filter must:

- Be linear.

- Commutes with both spacial and temporal derivatives.
- Conserve constant values.

For properly chosen filter functions, the filtering operation represented in Equation (3.12) satisfy all three criteria (see Sagaut (2006) for details).

The residual field, also called the subgrid scale field, $\phi^{'}$, is defined as the departure of $\bar{\phi}$ from the unfiltered field.

$$\phi^{'} \equiv \phi - \bar{\phi} \tag{3.13}$$

Using the above definition, we end up with the Reynolds like decomposition of u and p stated below.

$$u = \bar{u} + u^{'}, \qquad p = \bar{p} + p^{'} \tag{3.14}$$

Even though the decomposition given in (3.14) looks similar to the Reynolds decomposition, they differ in two important ways (Pope 2000).

- The filtered field $(\bar{.})$ is random.
- The filtered residual field $(.^{'})$ is in general non-zero, $\bar{f}' \neq 0$.

Explicit filtering of the Navier-Stokes equation is rarely a part of the solution procedure when performing Large Eddy Simulations. Instead, one usually solves the filtered system of equations directly, where the primitive variables are assumed filtered by the spatial discretization of the domain. As this procedure does not contain any filtering operation, it is usually referred to as implicit filtering. Although numerical differential operators have some low pass filtering effects there are issues related to consistency associated with the filtering process when employing implicit filtering techniques (Lund 2003).

Filtered Navier-Stokes and Continuity Equation

Application of a filter to Equation (3.2) yields

$$\frac{\partial \bar{u}_i}{\partial x_i} = 0, \tag{3.15}$$

from which we find that the residual velocity field $u^{'}$ is divergence free, i.e.,

$$\frac{\partial u_i^{'}}{\partial x_i} = \frac{\partial}{\partial x_i}\Big(u_i - \bar{u}_i\Big) = 0. \tag{3.16}$$

Similarly, we obtain the momentum equation for the filtered velocity by applying a filter to Equation (3.1).

$$\frac{\partial \bar{u}_i}{\partial t} + \frac{\partial}{\partial x_j}\big(\overline{u_i u_j}\big) = -\frac{\partial \bar{p}}{\partial x_i} + \nu \frac{\partial^2 \bar{u}_i}{\partial x_j \partial x_j} \tag{3.17}$$

The filtered product $\overline{u_i u_j}$ is different from the product of the filtered velocities $\bar{u}_i \bar{u}_j$ and is unknown. As a remedy, this term is usually expressed as the difference between the filtered velocities and the subgrid stress tensor T_{ij} (Lesieur, Métais and Comte 2005).

$$\begin{aligned}\overline{u_i u_j} &= \bar{u}_i\bar{u}_j - (\bar{u}_i\bar{u}_j - \overline{u_i u_j}) \\ &= \bar{u}_i\bar{u}_j - T_{ij}\end{aligned} \tag{3.18}$$

By utilizing the above-mentioned decomposition as shown in (3.18) the momentum equation for the filtered velocity $\bar{u}$ becomes

$$\frac{\partial \bar{u}_i}{\partial t} + \frac{\partial}{\partial x_j}\left(\bar{u}_i\bar{u}_j\right) = -\frac{\partial \bar{p}}{\partial x_i} + \nu\frac{\partial^2 \bar{u}_i}{\partial x_j \partial x_j} + \frac{\partial}{\partial x_j}\Big(T_{ij}\Big) \tag{3.19}$$

In Equation (3.19), T_{ij} describes all momentum exchange between the resolved and unresolved scales. As originally proposed by Leonard (1975), the subgrid stress tensor T_{ij} can be decomposed as shown in Equation (3.20).

$$\begin{aligned}T_{ij} =& \bar{u}_i\bar{u}_j - \overline{u_i u_j} \\ =& \bar{u}_i\bar{u}_j - \overline{(\bar{u}_i + u_i^{'})(\bar{u}_j + u_j^{'})} \\ =& \mathcal{L}_{ij} + \mathcal{C}_{ij} + \mathcal{R}e_{ij}^{sgs}\end{aligned} \tag{3.20}$$

Here $\mathcal{L}_{ij} = \bar{u}_i\bar{u}_j - \overline{\bar{u}_i\bar{u}_j}$ is known as the Leonard tensor (Leonard 1975). $\mathcal{C}_{ij} = -\Big(\overline{\bar{u}_i u_j^{'}} + \overline{\bar{u}_j u_i^{'}}\Big)$ denotes the cross stress tensor, which represent the interaction between the resolved and unresolved velocity fields. The Reynolds like stress term $\mathcal{R}e_{ij}^{sgs} = -\overline{u_i^{'}u_j^{'}}$ represents the interaction of the subgrid scales.

As the subgrid-scale tensors are unknown one needs to introduce proper models for T_{ij} to obtain a closed set of equations for $\bar{u}_i$.

The Filtered Strain Rate and Spin Tensors

The filtered velocity gradient forms a second order tensor and may thus be decomposed into symmetric and antisymmetric parts according to (3.21).

$$\frac{\partial \bar{u}_i}{\partial x_j} = \frac{1}{2}\left(\frac{\partial \bar{u}_i}{\partial x_j} + \frac{\partial \bar{u}_j}{\partial x_i}\right) + \frac{1}{2}\left(\frac{\partial \bar{u}_i}{\partial x_j} - \frac{\partial \bar{u}_j}{\partial x_i}\right) = \bar{S}_{ij} + \bar{W}_{ij} \tag{3.21}$$

Here $\bar{S}_{ij}$ denotes the symmetric strain-rate tensor, while $\bar{W}_{ij}$, commonly called the spin tensor, is its antisymmetric part, that is $\bar{W}_{ij} = -\bar{W}_{ji}$. From Newtons stress law it follows that the viscous stresses are linearly dependent on the strain-rate tensor, while the antisymmetric spin tensor holds the same information as the vorticity field (Pope 2000).

Conservation of Kinetic Energy

The transfer of energy between the filtered and subgrid scale is an important issue in the modeling of turbulence. The filtered kinetic energy field $\bar{k} = \frac{1}{2}\overline{u_k u_k}$ can be expressed in the following manner

$$\bar{k} = \underbrace{\frac{1}{2}\bar{u_k}\bar{u_k}}_{k_f} + \underbrace{\frac{1}{2}\overline{u_k u_k} - \frac{1}{2}\bar{u_k}\bar{u_k}}_{k_r} \tag{3.22}$$

where k_f is the kinetic energy of the filtered velocity field and k_r denotes the residual kinetic energy. Multiplying the momentum equation of the filtered velocities by $\bar{u}_i$ the conservation equation for the filtered kinetic energy is obtained.

$$\frac{\partial k_f}{\partial t} + \bar{u}_j \frac{\partial k_f}{\partial x_j} + \frac{\partial \bar{u}_i p}{\partial x_i} - 2\nu \frac{\partial \bar{u}_i \bar{S}_{ij}}{\partial x_j} - \frac{\partial \bar{u}_i T_{ij}}{\partial x_j} = \underbrace{-2\nu \bar{S}_{ij}\bar{S}_{ij}}_{\epsilon_{k_f}} \underbrace{- T_{ij}\bar{S}_{ij}}_{\mathcal{P}_{k_r}} \tag{3.23}$$

The left-hand side of Equation (3.23) represents transport, while the two terms on the right-hand side represent the transfer of energy. More precise, ϵ_{k_f} denotes the viscous dissipation of the resolved velocity field, while the last term $\mathcal{P}_{k_r}$ is the rate of transfer of kinetic energy between the resolved and subgrid-scale. As the term appears as a sink in Equation (3.23), $\mathcal{P}_{k_r}$ is usually called the rate of production of residual kinetic energy. However, in contrast to ϵ_{k_f}, $\mathcal{P}_{k_r}$ is caused by inviscid interaction and may become negative. Implying a transfer of energy from the subgrid- to the resolved-scale.

Closure Problem

As already stated the subgrid-stress tensor is unknown in the LES formulation. In order to close the set of equations for the filtered velocity field, a model for the residual stresses is needed. Similar to RANS, one usually solves the closure problem by adopting a Boussinesq like hypothesis, i.e., we seek a relation between the residual stresses and the rate of strain of the filtered velocity field. This is commonly written as an eddy viscosity closure according to

$$T_{ij} = 2\nu_e \bar{S}_{ij} + \frac{1}{3} T_{kk} \delta_{ij}, \tag{3.24}$$

where the ν_e denotes the so-called eddy viscosity. Introducing Equation (3.24) into the momentum equation for the resolved velocity field yields the eddy viscosity closed LES formulation.

$$\frac{\partial \bar{u}_i}{\partial t} + \frac{\partial}{\partial x_j}\left(\bar{u}_i \bar{u}_j\right) = -\frac{\partial}{\partial x_i}\left(\bar{p} - \frac{1}{3} T_{kk}\right) + \nu \frac{\partial^2 \bar{u}_i}{\partial x_j \partial x_j} + \frac{\partial}{\partial x_j}\left(2\nu_e \bar{S}_{ij}\right) \tag{3.25}$$

Equation (3.25) still contains the yet unknown eddy viscosity. We therefore need to find an explicit expression for ν_e to finalize the closure. A multitude of models have been proposed, the best known being the Smagorinsky model. Smagorinsky (1963) adopts the mixing-length hypothesis to obtain a model for the eddy viscosity as a product of the filter width Δ, and a characteristic velocity scale based on the second invariant of the filtered stress-strain tensor $\left|\bar{S}\right| = (2\bar{S}_{ij}\bar{S}_{ij})^{\frac{1}{2}}$. The Smagorinsky eddy viscosity reads

$$\nu_e = (C_s \Delta)^2 \left|\bar{S}\right|. \tag{3.26}$$

Due to its simplicity, Equation (3.26) has become a widely used model for the eddy viscosity. However, the appropriate value of the Smagorinksy constant, C_s, differs for different flow regimes, e.g where as $C_s \approx 0.17$ gives a realistic description of isotropic turbulence, the constant should equal zero to model

the absence of residual shear stresses in laminar flow regimes. The dynamic Smagorinsky model proposed by Germano et al. (1991) solves this problem by determining the Smagorinksy constant locally via double filtering. Following this methodology Lilly (1992) derived the following modified version of the dynamic Smagorinsky model

$$\nu_e = \frac{\Delta^2}{2} \frac{\left(\tilde{\bar{\Delta}}^2 \left|\tilde{\bar{S}}\right| \tilde{\bar{S}}_{ij} - \Delta^2 \widetilde{|\bar{S}|\bar{S}_{ij}}\right)\left(\tilde{\bar{u}}_i \tilde{\bar{u}}_i - \widetilde{\bar{u}_i \bar{u}_i}\right)}{\left(\tilde{\bar{\Delta}}^2 \left|\tilde{\bar{S}}\right| \tilde{\bar{S}}_{kl} - \Delta^2 \widetilde{|\bar{S}|\bar{S}_{kl}}\right)\left(\widetilde{\Delta}^2 \left|\tilde{\bar{S}}\right| \tilde{\bar{S}}_{kl} - \Delta^2 \widetilde{|\bar{S}|\bar{S}_{kl}}\right)} |\bar{S}| \tag{3.27}$$

where $\tilde{(\cdot)}$ denotes the additional test filter with filter width $\widetilde{\Delta}$, usually taken to be 2 times the size Δ. Dynamic Smagorinsky models tend to produce large negative values for ν_e, yielding a non-physical growth of the filtered kinetic energy. Consequently, LES computations applying Equation (3.27) are in general unstable (Pope 2000). Germano et al. (1991) showed that one could avoid extreme values of the eddy viscosity by averaging the numerator and denominator in the expression for ν_e. While the averaging process removes the local minima of ν_e, transfer of energy from the residual to the resolved velocity field due to negative values of ν_e can occur. Hence, to eliminate this so-called backscatter, some dynamic eddy-viscosity models perform clipping of ν_e, that is, setting the eddy viscosity to zero at locations where the computed values are negative (B. Vreman, Geurts and Kuerten 1997).

A. Vreman (2004) proposed an explicit eddy viscosity model that correctly predicts small viscous dissipation in transitional and near-wall regions not involving ad hoc clipping or averaging procedures. By investigating the behavior of several functionals of the second invariant of the velocity gradient and comparing their behavior with the theoretical transfer rate of energy, $\mathcal{P}_{k_r}$, Vreman derived the following dynamic eddy viscosity model

$$\nu_e = C_v \sqrt{\frac{B_\beta}{\frac{\partial \bar{u}_i}{\partial x_j}\frac{\partial \bar{u}_i}{\partial x_j}}}, \tag{3.28}$$

where

$$B_\beta = \beta_{11}\beta_{22} - \beta_{12}^2 + \beta_{11}\beta_{33} - \beta_{13}^2 + \beta_{22}\beta_{33} - \beta_{23}^2, \tag{3.29}$$

and

$$\beta_{ij} = \Delta_m^2 \frac{\partial \bar{u}_m}{\partial x_i}\frac{\partial \bar{u}_m}{\partial x_j}. \tag{3.30}$$

The Vreman model constant C_v is related to the Smagorinksy constant by, $C_v, \approx 2.5 C_s$. Similar to the Smagorinsky model, the model presented by Vreman does not need more than the local filter width and the velocity gradient and have essentially the same computational cost as the less accurate Smagorinsky scheme. Due to the model's relatively high accuracy combined with its reasonable computational cost, the Vreman model is a suitable candidate for LES of complex flows.

3.3 Wall Modeled Large Eddy Simulation

Solid boundaries will always induce a large computational cost, due to the advent of turbulent boundary layers, independent on how one chooses to model

the near-wall region. In Wall-Modeled Large Eddy Simulation, one seeks to minimize this additional cost by resolving the energetic motion in the outer layer, while modeling the fluid motion in the inner region. Hence, omitting the need for resolving the small-scale turbulent structures within the boundary layer.

Following the taxonomy given in X. I. Yang and S. T. Bose (2017), one may divide WMLES models into three subcategories dependent on how they formulate the boundary conditions: Dirichlet-type, Neumann-type, or Mixed-type. The Dirichlet-type wall models assign a streamwise slip velocity u_{slip} to a virtual surface located a predefined distance above the solid boundary (Chung and Pullin 2009; Bazilevs and Hughes 2007). The Neumann-type models, such as the equilibrium models proposed by Deardorff (1970) and Schumann (1975), provides the shear stress, while the velocity is not explicitly modeled. The Mixed-type, also known as Robin-type boundary condition, provides the wall condition as a weighted combination of Dirichlet and Neumann boundary conditions as stated in Equation (3.31). Here l_p denotes the slip length, and x_n is the wall-normal coordinate (S. Bose and Moin 2014). Piomelli and Balaras (2002) provides a comprehensive review of the most commonly used wall-models.

$$u_i - l_p \frac{\partial u_i}{\partial x_n} = 0 \quad \text{for } i = 1, 2, 3 \tag{3.31}$$

Wall-Stress Models

The most commonly used wall models are the so-called Wall-Stress Models (WSM). This class of wall models omits the need to resolve the near-wall turbulence by replacing the classical no-slip boundary condition with a Neumann condition in terms of the wall stress. In general, the problem presented by wall-stress modeled LES can be stated as follows: given the instantaneous velocity field $\vec{u}$ a distance h_{wm} above the wall (usually the first grid point off

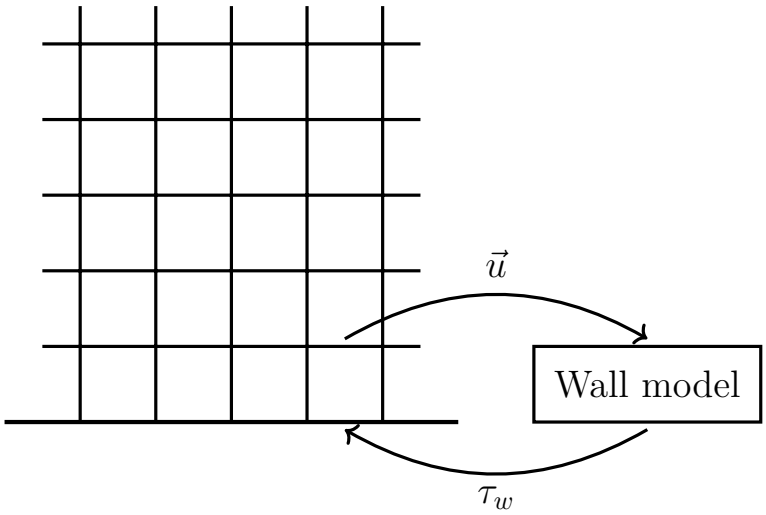

Figure 3.2: The principle of wall-stress-modeled LES. The wall-model is fed the instantaneous velocity obtained from the LES and returns the wall stress.

the wall), find an approximation of the local and instantaneous wall shear stress τ_w at the wall (Larsson et al. 2016). Figure (3.2) illustrates the principle of wall-stress modeled LES.

Most models classified as WSM determines the wall stress by applying the principle of conservation of linear momentum. Assuming the boundary layer to be sufficiently thin and that the interaction between the near-wall region and the outer region is weak, the filtered momentum equation reduces to the Turbulent Boundary Layer Equation (TBLE) given in Equation (3.32).

$$\frac{\partial \bar{u}_i}{\partial t} + \frac{\partial}{\partial x_j}\left(\bar{u}_i \bar{u}_j\right) = -\frac{\partial \bar{p}}{\partial x_i} + \nu \frac{\partial^2 \bar{u}_i}{\partial x_j \partial x_j} + \frac{\partial}{\partial x_j}\Big(T_{ij}\Big) \quad \text{for} \quad i = 1, 3 \tag{3.32}$$

Here, x_1 and x_3 denotes the wall-parallel coordinates, with the corresponding velocity components u_1 and u_3. At the wall, a no-slip boundary condition is applied, while the wall parallel velocity components u_1 and u_3 are matched to the LES solution at the outer boundary (Piomelli and Balaras 2002).

Equilibrium Wall Models

The simplest WSM are the equilibrium models, for which one further assume the pressure gradient and convective transport to exactly balance each other. Substituting the subgrid stress tensor with the Boussinesq eddy viscosity assumption (3.24) the simplified TBLE (3.32), assuming two-dimensional flow, becomes Equation (3.33).

$$\frac{\partial}{\partial x_n}\Big(\nu_e \frac{\partial \bar{u}_p}{\partial x_n}\Big) + \nu \frac{\partial^2 \bar{u}_p}{\partial x_n^2} = 0 \tag{3.33}$$

Here $\bar{u}_p$ is the wall-parallel velocity and x_n denotes the wall-normal coordinate. Equation (3.33) can be solved directly to obtain the friction velocity u_τ, defined in Equation (3.34), from which we may obtain the local wall shear stress.

$$u_\tau \equiv \sqrt{\frac{\tau_w}{\rho}}, \quad \text{where} \quad \tau_w = \rho \nu \frac{\partial \bar{u}_p}{\partial x_n}\Big|_{x_n = x_{n,wall}}. \tag{3.34}$$

Alternatively, one may use the approximated solution of (3.33) given in Equation (3.35) (Deardorff 1970, Larsson et al. 2016, Schumann 1975). Equation (3.35) is commonly referred to as the *Law of the Wall*. From experiments, the von Kármán constant K is found to be ≈ 0.4 and the constant $B \approx 5.0$ (Schlichting and Gersten 2000).

$$u^+_{wm} = \begin{cases} y^+ & y^+ \lesssim 5 \\ K^{-1} \ln y^+ + B & y^+ \gtrsim 30 \end{cases} \tag{3.35}$$

The normalized velocity u^+_{wm} and off wall distance y^+ are made dimensionless in terms of the wall units ν and u_τ, according to Equation (3.36).

$$u^+_{wm} = \frac{u_p}{u_\tau} \quad \text{and} \quad y^+ = \frac{y u_\tau}{\nu} \tag{3.36}$$

As equation (3.35) couples the wall-shear stress to the flow velocity algebraically, it is simple to implement and considerably cheaper, in terms

of computational cost, compared to solving the TBLE directly. The coupling of the assumed velocity profile given in (3.35) leads to the matching condition $||\bar{u}||_{y=h_{wm}} = u_{wm}$, which one can solve for the friction velocity u_τ using either fixed-point iteration or Newton's method. The standard practice is to estimate the wall-stress by solving the wall model over the first off-wall gird cell, that is $h_{wm} = \Delta y$. However, as pointed out by Kawai and Larsson (2012) there are nothing requiring the wall-model to be applied between the first grid point and the wall, only that the wall-model is still valid at the point $y = h_{wm}$.

In general, for most algebraic closure models, the *Law of the Wall* is enforced locally and instantaneously, and the impermeability condition is applied across the solid boundary (S. T. Bose and Park 2018).

The Log-layer Mismatch

It is well known that WMLES wrongly predicts the normalized mean velocity profile, the results deviating as much as 20% from the correct value. These discrepancies, known as the *Log-Layer Mismatch* (LLM), occur independent of grid topology, subgrid model and wall-model. Numerical experiments have shown both positive mismatch, consistent over prediction of u^+, (Kawai and Larsson 2012; X. I. Yang, Park and Moin 2017) and negative mismatch, consistent under prediction of u^+ (J. Lee, Cho and Choi 2013; Nicoud, Baggett et al. 2001). The effect of positive mismatch is illustrated in Figure (3.3). Larsson et al. (2016) points out that compressible flow solvers using staggered grids generally under-predict the mean velocity profile, while solvers using co-located grids usually produce a positive mismatch. Hence, LLM seems to be affected by the numerical scheme at hand as well as the wall model.

Up to the present date, there exist no single solution to the LLM problem. Several remedies, based on different assumptions, have been proposed which all seems to reduce the *Log-Layer Mismatch*. Kawai and Larsson (2012)

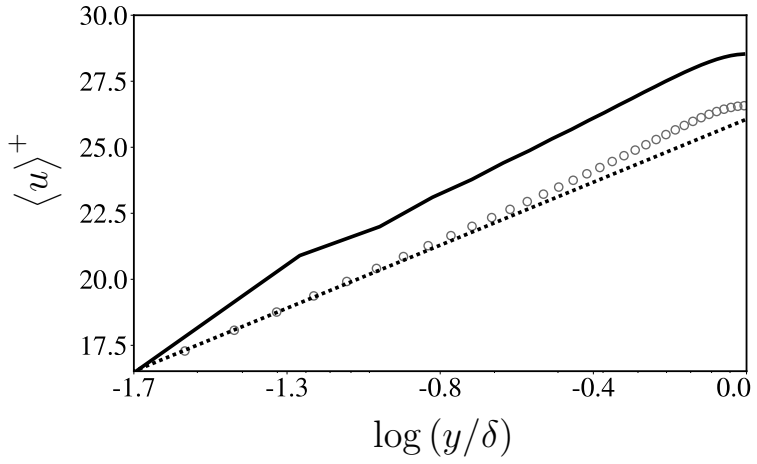

Figure 3.3: Example of positive mismatch. (———), Mean velocity profile obtained by wall-modeled LES for a fully turbulent channel flow; (·····), *The law of the wall* with $K = 0.41$ and $B = 5.2$; (◯), DNS data (M. Lee and R. Moser 2015).

hypothesized that LLM is caused by feeding the wall-model with erroneous data. They argued that the LES solution close to the wall (i.e. the first few grid points off the wall) is plagued by numerical and modeling errors. Thus, wall-models operating on the raw LES velocity at the wall-adjacent grid point, which has been the established practice, necessarily yields an inaccurate wall stress. This being independent of the accuracy of the wall-model itself. Based on this reasoning, they argued that one may resolve the LLM problem by fixing h_{wm} and then refine the grid sufficiently, until numerical and subgrid errors are negligibly small at the sampling point.

Another solution to the LLM problem has been proposed by Bou-Zeid, Meneveau and Parlange (2004). They noted that the *Log-law* imposes an average wall-stress proportional to $\langle \bar{u} \rangle^2$, whereas the standard algebraic model relates the average wall-stress and velocity by $\langle \tau_w \rangle \propto \langle \bar{u}^2 \rangle$. From the Cauchy–Schwarz inequality, it follows that the modeled wall stress will exceed the expected value. As a remedy, they proposed a two-dimensional spatial filter at a scale corresponding to that of the LES resolution. One should note that the explanation given by Bou-Zeid, Meneveau and Parlange (2004) explains a negative mismatch, but do not address the problem of positive mismatch. Furthermore, X. I. Yang, Park and Moin (2017) did not find any correlation between the occurrence of LLM and the relative value of $\langle \bar{u}^2 \rangle$ and $\langle \bar{u} \rangle^2$. Still, spatial filters seem to resolve the LLM problem as results obtained by Bou-Zeid, Meneveau and Parlange (2004), X. Yang et al. (2015) and X. I. Yang, Park and Moin (2017) successfully solved the LLM problem by applying spatial filtering.

As an alternative explanation, X. I. Yang, Park and Moin (2017) suggests that, the mismatch is caused by an incorrect prediction of the near-wall Reynolds shear stress $\langle u'v' \rangle$, due to an unphysically high correlation between the wall-adjacent LES velocity and the wall model, which in turn leads to an overestimate of the velocity gradient. Following this argument, they proposed feeding the wall-model with the temporally filtered velocity at the first off-wall cell. This mechanism does provide a unified explanation for the previous remedies mentioned so far, as all methods would reduce the artificial correlation. However, as noted by S. T. Bose and Park (2018), this argument does not explain negative mismatch.

PART II

Numerical Experiments

CHAPTER 4

Numerical setup

The following chapter outlines the specifics of the numerical model applied in the present study. As the choice of a computational domain and grid topology is essential for any CFD study, this chapter supplies the reader with a detailed description of the computational domain, computational grid and boundary conditions. Next, we introduce the wall model employed together with the different filtering schemes tested in this thesis. The chapter concludes with some general remarks regarding practical problems one may encounter if one wishes to leave the traditional approach of feeding the wall model with the LES solution sampled at the first off-wall grid point.

The simulations are carried out using the compressible, low-mach, finite volume-based solver developed by Cascade Technologies (Ambo et al. 2020). The solver employed is second order in space and time. The coupling between the pressure and velocity is accomplished by approximating the flow as isentropic.

The Vreman eddy viscosity model (B. Vreman, Geurts and Kuerten 1997) is used for modelling the subgrid stresses due to its favorable properties described in Chapter 3.2. The primitive variables $\vec{u}$ and p are not explicitly filtered. Instead, the pressure and velocity field are assumed to be implicitly filtered by the discretization procedure. We apply a Cartesian coordinate system x, y, z and denote the stremwise (x), wall-normal (y) and spanwise (z) velocity components as u, v, w respectively. The superscript $(.^+)$ indicates normalization in terms of the kinematic viscosity ν and friction velocity u_τ. Furthermore, $\langle . \rangle$ denote the average across time and space, while $(.')$ is used to indicate fluctuations with respect to the average. The Cascade grid generator Stitch, which applies the properties of clipped Voronoi-diagrams to discretize the numerical domain (Brès et al. 2018), is used to generate the grids.

4.1 Fully Developed Turbulent Channel Flow

To study the different wall modeling strategies and their suitability for different mesh topologies we consider a fully developed turbulent flow between two parallel planes, as sketched in Figure (4.1). Impermeability and stress boundary conditions are imposed at the walls, and periodic boundary conditions are applied in the streamwise and spanwise directions. Hence, the flow that exits at the downstream boundary of the domain is fed back at the upstream boundary. The computational domain is of size $24\delta \times 2\delta \times 9\delta$, where $\delta = 0.5\ m$ denotes the channel halfwidth. To encourage the transition from laminar to turbulent

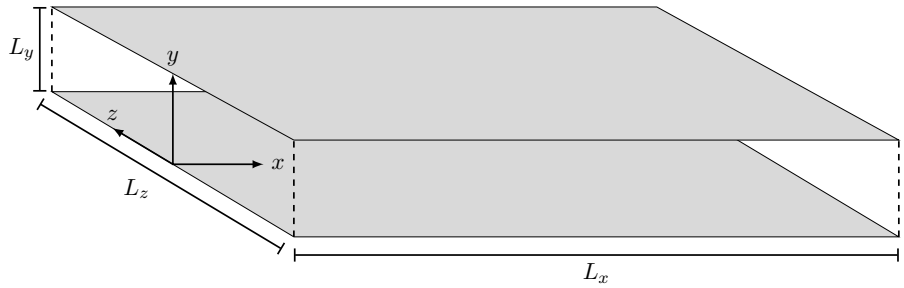

Figure 4.1: Sketch of the plane channel and the Cartesian coordinate system. L_x, L_y and L_z denotes the channel length, width and height respectively.

flow we provide the channel with a perturbed velocity field as initial condition. Further, the flow is driven by a time-independent momentum source term, which is added to the streamwise momentum equation. Physically, this is equivalent to a flow driven by a constant pressure gradient. To ensure that the flow behaves as an incompressible fluid, and to suppress the advent of spurious pressure waves due to the periodic boundary conditions, the fluid speed of sound, c, is set sufficiently large. In the present case $c = 1000\ m/s$ was found to yield satisfactory results.

As the flow is driven by a prescribed pressure gradient, the mean wall-stress is known. Hence, we set the friction velocity based Reynolds number, defined in Equation (4.1), to ≈ 5200 by adjusting the kinematic viscosity ν.

$$Re_\tau = \frac{u_\tau \delta}{\nu} \tag{4.1}$$

In terms of the bulk velocity U_b, which represent the average velocity through the channel, this corresponds to a Reynolds number Re_b approximately equal to 130000.

$$Re_b = \frac{U_b \delta}{\nu}, \quad \text{where} \quad U_b = \frac{1}{2\delta} \int_0^{2\delta} u \, \mathrm{d}y. \tag{4.2}$$

All numerical simulations employ a fixed time-step of $\Delta t = 0.001s$, to ensure that the instantaneous Courant number is sufficiently small. Hence the

Table 4.1: Main simulation parameters for the turbulent channel flow.

Friction velocity based Reynolds number, Re_τ	5200
Bulk velocity based Reynolds number, Re_b	130000
Kinematic viscosity, ν	4.8×10^{-5}
Fluid density, ρ	1.0
Fluid speed of sound, c	1000
Friction velocity, u_τ	0.5
Wall shear stress, τ_w	0.25
Domain size ($L_x \times L_y \times L_z$)	$24\delta \times 2\delta \times 9\delta$
Time step Δt	10^{-3}
Bulk velocity, U_b	13.5
Flow through time, T_f	0.89

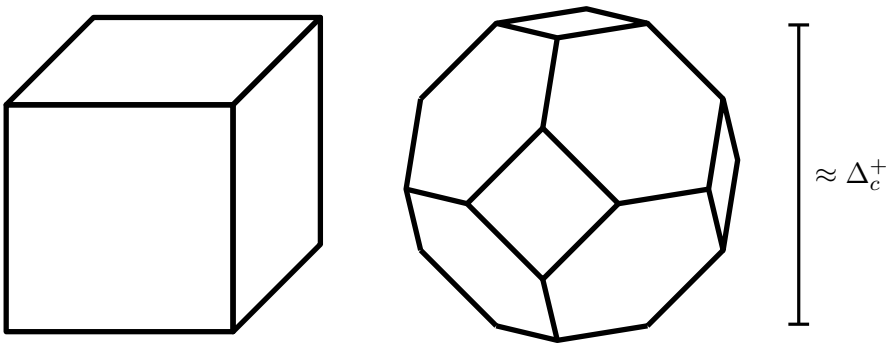

Figure 4.2: Illustration of the different grid cells. (Left) Hexahedron gird cell; (Right) Truncated octahedron cell.

temporal resolution of turbulence is grid and filter independent. To remove any transient turbulent structures, each simulation were run for at least 100 T_f, where $T_f = L_x/U_b$ denotes the average flow through time, before gathering of statistical data. The main parameters are summarized in Table (4.1).

The present study considers two different cell lattices: Hexahedron (Hex) and Truncated Octahedron (Oct). Both are illustrated in Figure (6.5). Besides the two cell types, three different grid resolutions are considered. As the near-wall resolution of the computational domain is the dominating factor, the three grid refinement levels are defined in terms of their wall normal resolution Δ_c^+. Here Δ_c^+ denotes the average wall normal extent of the boundary cells. The grids tested have $\Delta_c^+ = 300$, $\Delta_c^+ = 200$ and $\Delta_c^+ = 100$. All test cases have a uniform cell structure, i.e.. $\Delta x = \Delta y = \Delta z \approx \Delta_c^+$. This corresponding to a spatial resolutions ranging from 0.25×10^6 to 7.59×10^6 cells. Hence, each filtering strategy is tested on six different grids. The number of grid cells for each mesh, together with the computational cost C_{cost} is reported in Table (4.2). Following Mukha, Bensow and Liefvendahl (2021) C_{cost} is estimated by how many hours it would take one processor to advance the solution by one T_f. We note that this metric assumes linear growth of computational effort, neglecting parallelization overhead. The data presented in Table (4.2) shows that simulations on hexahedral and truncated octahedral meshes have comparable computational cost in terms of the near wall resolution.

Table 4.2: The dimensionless average wall normal cell size Δ^+, number of cells N_{cells} in millions and the computational cost C_{cost} for the mesh topologies tested in the current thesis.

Δ_c^+	Hexahedron		Octahedron	
	N_{cells}	C_{cost}	N_{cells}	C_{cost}
300	0.276	0.27	0.253	0.24
200	0.949	1.28	0.927	1.45
100	7.593	18.89	4.689	19.8

4.2 Treatment of Solid Boundaries

All cases addressed in the thesis employ an algebraic wall model. Since Equation (3.35) is not C^1 continuous, we depart from the traditional *Law of the wall*. Instead employing the piecewise algebraic expression given in Equation (4.3), with $K = 0.41$, $B = 5.2$ and $\hat{y} \approx 23.32$.

$$u^+_{wm} = \begin{cases} y^+ + \left(2\hat{y}\right)^{-1}\Big(\left(K\hat{y}\right)^{-1} - 1.0\Big)\hat{y}^2 & y^+ \leq \hat{y} \\ K^{-1}\ln y^+ + B & y^+ > \hat{y} \end{cases} \tag{4.3}$$

Matching Location

Following the methodology of Kawai and Larsson (2012) the strategy of feeding the wall model with the instantaneous LES solution u_{LES} sampled some distance above the wall, as illustrated in Figure (4.3), is tested. As pointed out by Larsson et al. (2016), the wall-model thickness h_{wm} should be independent of the LES grid to ensure that the wall model is grid independent. Hence, the velocity u_{wm} is sampled at a fixed distance, e.g. 20 % of the local boundary layer thickness, instead of the n-th off-wall grid point, i.e,

$$u_{wm}(x, z, t) = u_{LES}(x, y, z, t)\big|_{y=h_{wm}}. \tag{4.4}$$

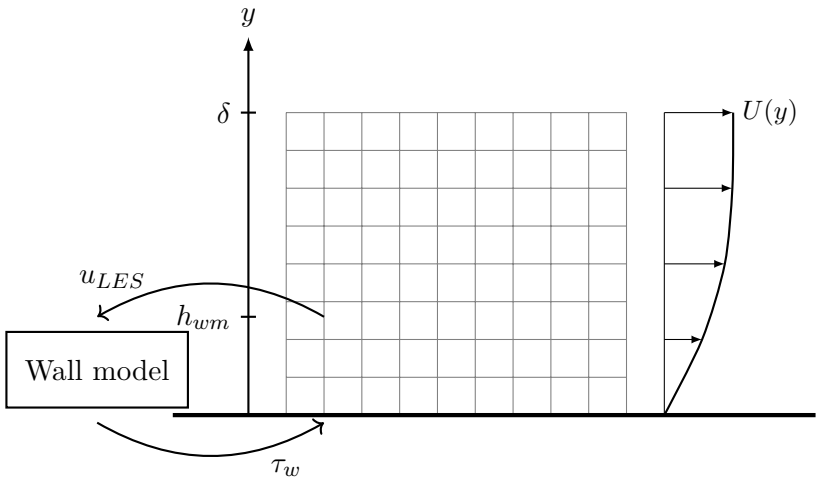

Figure 4.3: Illustration of the wall normal filtering scheme. The wall model models the flow over a layer of thickness h_{wm}. It is fed the instantaneous velocity obtained from the LES solution, and returns the instantaneous wall stress at the solid boundary to the LES, which then uses this as the wall boundary condition.

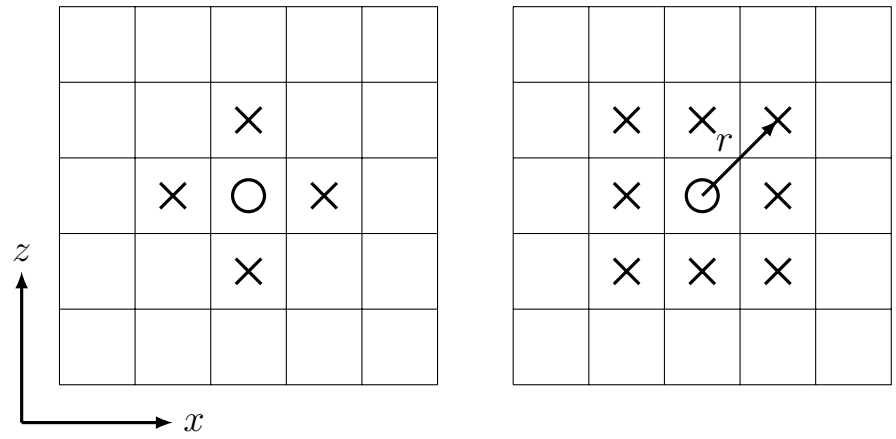

Figure 4.4: Illustration of the two wall parallel filters applied to the boundary cell (◯) for a hexahedrion mesh. (×) marks the neighboring cells that are included in the filtering scheme. (Left): 5-points stencil. Right: 9-point stencil. r represent the distance from the center cell to the neighboring cells.

Spatial Filtering

Two spatial filtering techniques are tested, namely a five-point-stencil and a nine-point-stencil filter. The two filters, illustrated in Figure (4.4), are performed within the wall parallel plane located at the first off-wall grid point. The wall-model velocity, u_{wm}, is computed according to Equation (4.5). The spatial filtering weights w^i are computed using two different schemes, a uniform weighting scheme for which the weights w^i are constant, and a quadratic scheme. For the latter scheme $w^i \propto 1/r^2$, where r denoting the distance between the center and neighboring control volumes. The center cell is given a weight of 0.5.

$$u_{wm} = \sum_i w^i u^i_{LES}, \quad \text{where} \sum_i w^i = 1. \tag{4.5}$$

Temporal Filtering

As proposed by X. I. Yang, Park and Moin (2017) the temporal filtering scheme presented in Equation (4.6) is tested.

$$u^n_{wm} = (1-\epsilon)u^{n-1}_{wm} + \epsilon u^n_{LES} \tag{4.6}$$

Here, u_{LES} is the instantaneous velocity obtained by the LES at the first off-wall grid point, and the superscript n denotes the time step index of the LES solution. According to X. I. Yang, Park and Moin (2017) the weight ϵ is defined as $\Delta t/T_{tf}$, where Δt is the simulation time step and T_{tf} represent the filtering time scale. The time scale T_{tf} can be estimated locally, e.g. as a fraction of the local convective time scale, or globally in terms of characteristic flow or simulation properties. Herein the latter is applied, defining T_{tf} in terms of the computational time step as $T_{tf} = m\Delta t$.

4.3 Numerical Implementation

Presently (May 2022) none of the filtering schemes presented in Section (4.2) are implemented in the finite volume-based solver developed by Cascade Technology. Thus, the implementation of these filtering procedures has been a part of this thesis. Even though the general principle of each filterer is quite simple, there are challenges related to the implementation of the different schemes. As the issues related to the implementation of these schemes are mostly code-specific, only some general remarks regarding the challenges met in the implementation of the different strategies are made.

An issue one might encounter if one wishes to feed the wall model with a velocity sampled at a pre-defined distance h_{wm} or at the n^{th} off-wall grid point, is that the matching location may not be well defined by the grid topology. Thus, in most circumstances, it will be necessary to introduce some kind of interpolation procedure to obtain the LES solution at the required matching location. This problem is efficiently solved by introducing an interpolation stencil during the initialization initialisation process. Similar issues may arise when employing spatial filtering scheme. For flows past complex bodies, discretized using unstructured grids, it is not given that neighboring cells in the same wall parallel plane as the boundary node are themselves boundary cells. Which cells to include in the filtering process in such cases have no simple answer and must be resolved by the user on a case-by-case basis.

For all but the temporal filterer, we need to access non-local data, either from neighboring cells or from some off-wall cell, which may render these methods impractical, especially for flows involving complex wall geometries. At the moment, a Message Passing Interface (MPI) library is a key ingredient for most CFD tools. Hence, some or all of the cells needed by the filtering scheme, may reside on different MPI processors. As this will complicate the implementation, it may be tempting to avoid this issue by only considering cells on the same processor. This is however, a bad idea as this would make the wall model dependent on the domain decomposition, and the results will depend on the number of processors available. Further, unpublished work by Johan Larsson have shown that this may result in convergence issues (Larsson 2022). There are at least two reliable solutions to this problem:

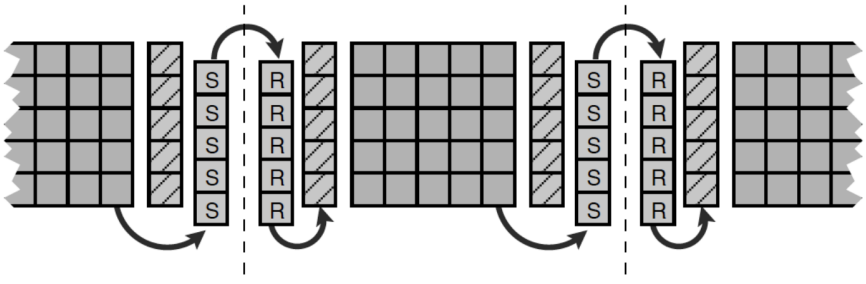

Figure 4.5: Illustration of communication between MPI processes in two dimensions. The cells labeled with S and R represents the intermediate send and receive buffers respectably (Hager and Wellein 2011).

- Build a MPI communicator during the initializing of the computational domain or during the pre-processing step.
- Modify the domain decomposition to ensure that all relevant cells are on the same processor.

This thesis employ the former strategy. That is, during the initialization of the computational grid the position of all non-local cell ID's used by the filter are located. Then local send and receive buffers, for which non-local data are transferred to and from the MPI processes, are constructed. For each time step during the simulation both buffers are updated, as illustrated in Figure (4.5), before the wall shear stress is computed. For details on parallel programming, message passing and MPI see Hager and Wellein (2011) and Gropp (1999).

As the current implementation of the non-local filtering schemes requires additional communication between different MPI processes, some communication overhead is unavoidable. Through careful domain decomposition and by employing non-blocking communication when possible, one can reduce the overhead due to the non-local communication. However, compared to the computational cost of solving the linear systems of equations, this overhead is negligible in most cases. On the other hand, the additional startup cost due to the construction of the MPI communicator, may become significant when the number of boundary nodes increases. A good approach to reducing the initialization overhead is to construct the virtual topology such that each domain has an equal numbers of boundary cells. In addition, one may further reduce the startup cost by constructing efficient algorithms for locating the position of the non-local cell data. As code optimization is beyond the scope of the present thesis, the effect of such strategies have not been investigated. Nonetheless, the startup procedure is only performed once and will, in general, not affect the overall efficiency of the solver.

CHAPTER 5

Numerical Results

In the following chapter we present results from WMLES of the internal flow presented in Section (4.1). Simulations are performed using different types of grid topologies and refinement levels. Furthermore, the effect of changing h_{wm} and filtering the wall model input, employing both spacial and temporal filters, are considered (see Section 4.2 for further details).

As a reference for estimating the error of the quantities of interest we use the DNS results presented by M. Lee and R. Moser (2015). The magnitude of LLM will be presented as the relative error, in percent, of the normalized mean streamwise velocity profile with respect to the reference DNS.

$$LLM_{\%} = \frac{\left\| \langle u_{LES} \rangle^{+} - \langle u_{DNS} \rangle^{+} \right\|_2}{\left\| \langle u_{DNS} \rangle^{+} \right\|_2} \cdot 100 \tag{5.1}$$

Here, $\|.\|_2$ is defined according to Equation (5.2), and is estimated using Simpson's rule. As the spatial sampling rate of the DNS data is significantly higher than what is obtained by WMLES, the reference data are obtained by averaging the DNS profile across the extent of the LES grid cell.

$$\|.\|_p = \left(\int_0^{\delta} (.)^p \right)^{1/p} \tag{5.2}$$

In a fully developed channel, the flow is homogeneous in the streamwise and the spanwise directions. Hence we only report results of the non-zero stresses $\langle u'u' \rangle, \langle v'v' \rangle, \langle w'w' \rangle$, and $\langle u'v' \rangle$ (Mansour, Kim and Moin 1988) or quantities derived from them. When relevant, we also report the error distribution $err()$ defined in Equation (5.3).

$$err([.]) = \frac{\langle [.](y)_{LES} \rangle - \langle [.](y)_{DNS} \rangle}{\langle [.](y)_{DNS} \rangle} \cdot 100 \tag{5.3}$$

5.1 Non-Filtered Algebraic Wall Model

LLM is influenced by a combination of the numerical scheme at hand, the subgrid model employed, as-well as the wall model. Hence, the first step in the present investigation of LLM is to obtain a baseline data set which we can use to measure the effect of the strategies investigated herein. For this purpose we reproduce the LLM in a turbulent channel flow by feeding the algebraic model

Table 5.1: $LLM_{\%}$ in simulations employing the non-filtered algebraic wall model.

Δ_c^+	Hex	Oct
100	7.14	3.34
200	5.43	1.78
300	3.84	1.78

with the instantaneous LES solution sampled at the first off-wall grid point. Furthermore, as the grid topology and refinement level also affect the predictive accuracy of WMLES, the baseline simulation is carried out for several mesh topologies and refinement levels.

The mean streamwise velocity, obtained using the standard algebraic wall modeling approach, is presented in Figure (5.1). As the flow is driven by a constant pressure gradient, the mean wall-stress is always correctly predicted. Hence, LLM manifests itself as an erroneous shift of the mean velocity profile, as clearly shown in the figure, where a significant positive mismatch is observed for all simulations. The mean velocity at a distance y^* above the wall is given by Equation (5.4), thus this erroneous upshift seems to indicates that the wall model over-predicts the mean velocity gradient close to the wall.

$$\left\langle u(y^*)\right\rangle = \int_0^{y^*} \left\langle \frac{du}{dy} \right\rangle \mathrm{d}y \tag{5.4}$$

Comparing the results obtained on the different grids, the simulations on the truncated octahedral grids are allover the most accurate. The results presented in Table (5.1) show that $LLM_{\%}$ is approximately 2 for the latter grid topolgy, while $LLM_{\%} \approx 5$ for the solutions on the hexahedra grids. Refining the mesh does not improve the predictions of $\left\langle u\right\rangle^+$, on the contrary, it degrades

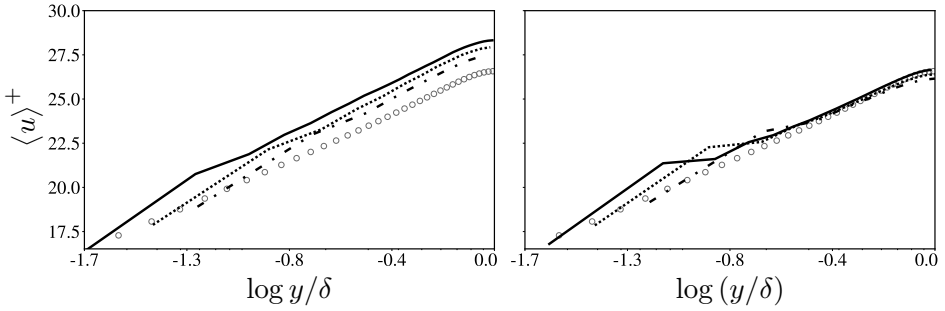

Figure 5.1: Mean velocity profile computed using the non-filtered algebraic wall-model and the reference DNS data obtained by M. Lee and R. Moser (2015). (Left) Hexaedral grid cells; (Right) Octahedral grid cells. (———), $\Delta_c^+ = 100$; (·····), $\Delta_c^+ = 200$; (-·-·-·-), $\Delta_c^+ = 300$; (◯), DNS data.

the accuracy. On the other hand, increasing the grid density results in an better description of the shape of the velocity profile. This indicates that the numerical model yields better predictions of the velocity gradient as the cell size decreases.

Figure (5.2) shows the relative error of the mean velocity profile for simulations with characteristic cell size $\Delta_c^+ = 100$. Again, we observe that the solution on the truncated octahedron mesh is the most accurate. However, the simulations carried out on hexahedra meshes yield more accurate predictions of the mean flow velocity in the near wall region. This seems to be a general trend for all simulation performed herein. The reason why is not clear to the author. One reason might be that the topology of the truncated octahedral cells better coincide with the anisotropic motion in the core region, producing more accurate results in the wake, whereas the faces of the hexahedra meshes are better oriented with the planar flow in the near-wall region.

The error of the turbulent kinetic energy is also presented in Figure (5.2). In line with the findings of Mukha, Bensow and Liefvendahl (2021), the figure shows that the overall accuracy of the kinetic energy is significantly lower than what is observed for the mean velocity. The same trends are observed for both grids. However, whereas the truncated octahedron grids generally over-predict k, the simulations computed on the hexahedral mesh under-predicts the turbulent kinetic energy. The large error observed close to the center of the channel is due to the relatively small value of k in this region. Thus the relative error is a less reliable measure close to the centerline of the channel.

The diagonal terms of the Reynolds stress tensor and the turbulent kinetic energy are presented in Figure (5.3). In general, refining the mesh improves the estimates of all quantities. The trends observed for the mean velocity profile are also applicable for the diagonal elements of the Reynolds stress tensor and its trace. Simulations performed using truncated octahedral grid cells yielded better results in the wake, while hexahederal meshes produced better estimates of the Reynolds stresses in the near-wall region.

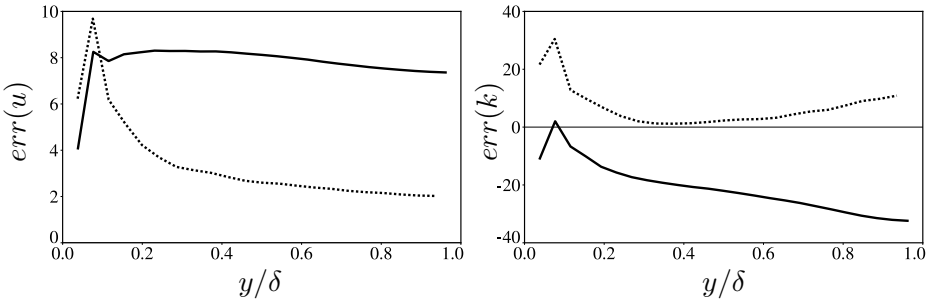

Figure 5.2: Relative error of the mean velocity profile (Left) and the turbulent kinetic energy (Right) in simulations applying the non-filtered algebraic wall-model with $\Delta_c^+ = 100$. (———), Hexahedron grid; (·····), Truncated octahedron grid.

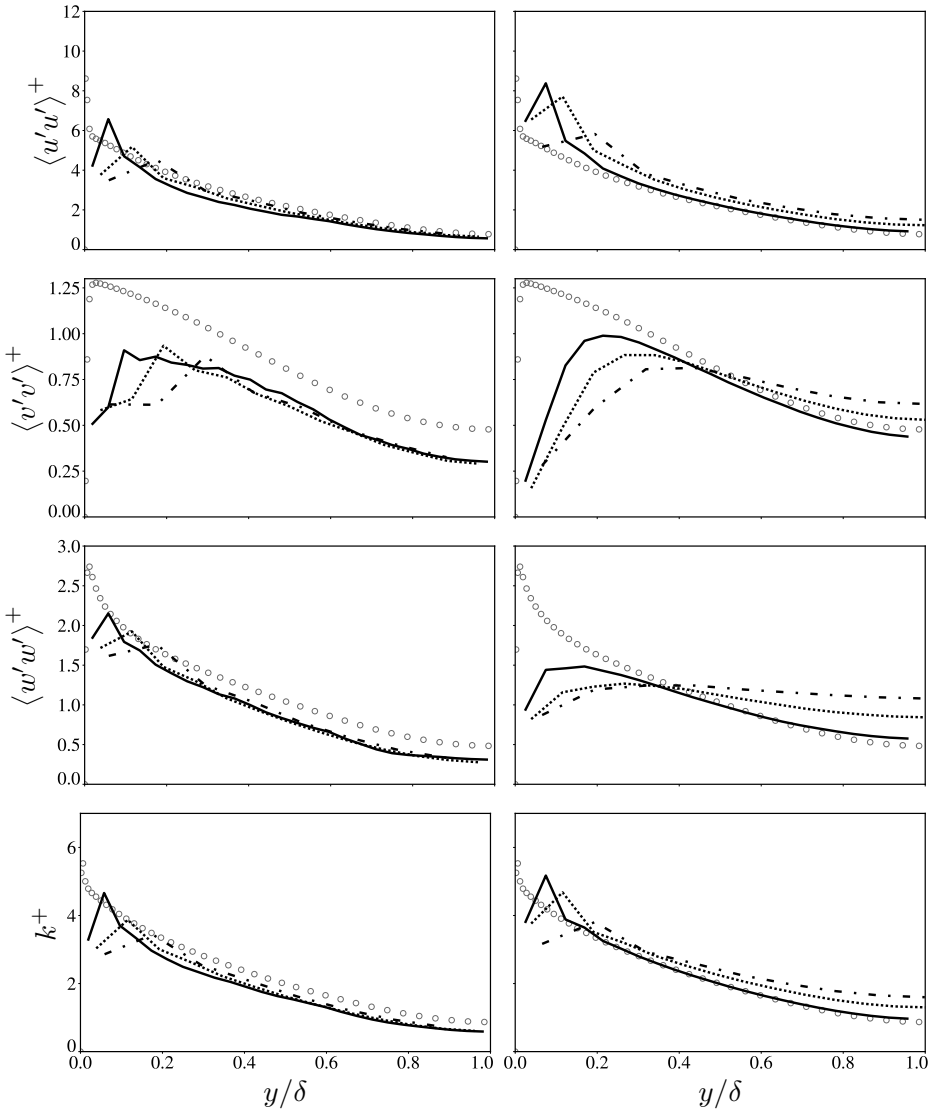

Figure 5.3: The diagonal components of the Reynolds stress tensor and the turbulent kinetic energy computed using the non-filtered algebraic wall-model and the reference DNS data obtained by M. Lee and R. Moser (2015). (Left) Hexahedral grid cells; (Right) Octahedral grid cells. (———), $\Delta_c^+ = 100$; (·····), $\Delta_c^+ = 200$; (-·-·-·-), $\Delta_c^+ = 300$; (◯), DNS data.

Figure (5.4) presents the Reynolds shear stress for simulations on hexahedra and truncated octahedra meshes. According to Pope (2000) the streamwise momentum equation yields the expression in Equation (5.5) for the total shear stress.

$$-\rho\langle u'v'\rangle + \rho\nu\left\langle \frac{du}{dy}\right\rangle = \langle\tau_w\rangle\left(1-\frac{y}{\delta}\right) \tag{5.5}$$

Outside the *log-layer* the velocity gradient $\langle du/dy\rangle$ is negligible. Hence in the core of the channel we may approximate the force balance as Equation (5.6).

$$-\rho\langle u'v'\rangle = \langle\tau_w\rangle\left(1-\frac{y}{\delta}\right) \tag{5.6}$$

As the mean wall shear is correctly predicted for the present channel flow, no significant error is thus expected in this region. This is clearly seen in Figure (5.4).

In the near wall region, significant errors are observed regardless of grid type and mesh refinement level. From Equation (5.5) it follows that erroneous prediction of the Reynolds shear stress could lead to an incorrect wall normal velocity gradient. Hence, one may argue that LLM is caused by erroneous prediction of the near-wall Reynolds stresses. The results presented below somewhat support this claim as the largest discrepancies of the near-wall Reynolds shear stress are observed in the simulations with the largest LLM for both the hexahedra and truncated octehedra mesh topologies. However, this argument does not explain the differences observed when comparing the results obtained on the two different mesh topologies, as the solution on hexahedral meshes more accurately predict $\langle u'v'\rangle$ while LLM$_{\%}$ are worse for these simulations. One should, however, note that these discrepancies might be due to other, unknown, numerical artifacts caused by the different grid topologies.

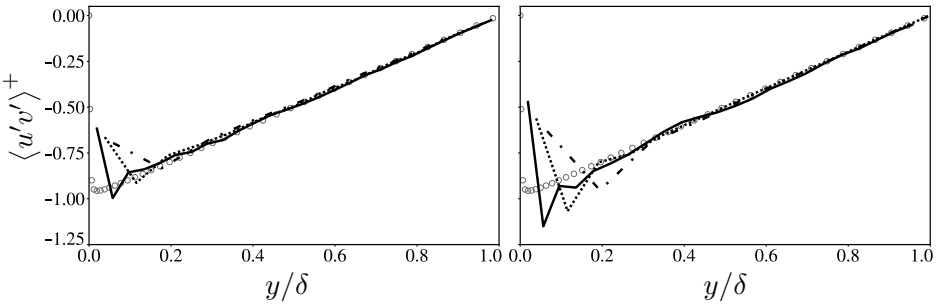

Figure 5.4: Reynolds shear stress computed using the non-filtered algebraic wall-model and the reference DNS data obtained by M. Lee and R. Moser (2015). (Left) Hexaedron grid cells; (Right) Octahedron grid cells. (———), $\Delta_c^+ = 100$; (·····), $\Delta_c^+ = 200$; (-·-·-·-), $\Delta_c^+ = 300$; (◯), DNS data.

The choice of subgrid stress model will, to some extent, affect the LES (Fureby et al. 1997, De Santis et al. 2020). Results obtained by X. I. Yang and S. T. Bose (2017) show that the choice of eddy viscosity closure model affect the predicted velocity field in a turbulent channel. In particular the turbulence intensity in the near wall region. Incorrect prediction of the eddy-viscosity ν_e, especially in the near wall region might therefore be the root source for the discrepancies observed so far. Integrating the equilibrium model, presented in Equation (3.33), and enforcing the shear stress condition $(\nu + \nu_e)du/dy = \tau_w/\rho$ at the wall, one finds that the wall shear stress and the mean velocity profile are related by Equation (5.7).

$$\Big(\nu + \nu_e\Big)\frac{\partial \bar{u}}{\partial y}\Big|_{y=h_{wm}} = \frac{\tau_w}{\rho} \tag{5.7}$$

Imposing the *Law of the wall* locally and instantaneously, and matching it with the instantaneous LES velocity at $y = h_{wm}$ yields the following expression for the wall shear stress:

$$\tau_w = \rho\left(\frac{K}{\ln\big(h^+_{wm}\big) + B}\right)^2 \bar{u}^2_{y=h_{wm}}. \tag{5.8}$$

By solving Equation (5.8) with respect to $\bar{u}_{y=h_{wm}}$ and differentiating with respect to y one obtains Equation (5.9).

$$\frac{\partial \bar{u}}{\partial y}\Big|_{y=h_{wm}} = \frac{u_\tau}{K h_{wm}} \tag{5.9}$$

Substituting Equation (5.8) and (5.9) into (5.7) yields the relation below.

$$\bar{u}_{y=h_{wm}} = \sqrt{\Big(1 + \nu^+_e\Big)\frac{1}{h^+_{wm}}}\frac{\ln h^+_{wm} + B}{K^{3/2}}u_\tau \tag{5.10}$$

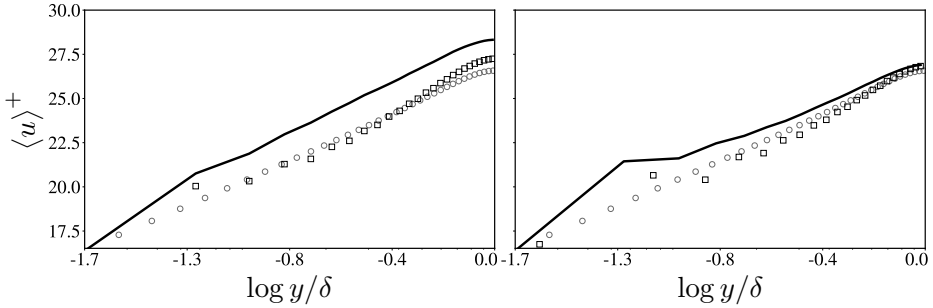

Figure 5.5: Mean velocity profile from simulations applying the non-filtered algebraic wall-model obtained on a mesh with characteristic grid size $\Delta^+_c = 100$. (Left) Hexaedron grid cells; (Right) Truncated Octahedron grid cells. (———), Vreman subgrud model; (□), No subgrid model; (◯), DNS data.

Table 5.2: $LLM_{\%}$ in simulations employing the algebraic wall model over a distance h_{wm} on grids with characteristic cell size $\Delta_c^+ = 100$.

h_{wm}	Hex	Oct
$\Delta_c/2$	7.14	3.34
0.10δ	1.24	2.85
0.20δ	1.89	2.71

From equation (5.10) it follows that a larger eddy viscosity necessarily leads to an increase of the velocity at the matching location $y = h_{wm}$. Therefore, turning of the subgrid model, setting ν_e to zero, should reduce the predicted velocity, at least in the near-wall region. This is clearly seen in Figure (5.5), which shows the mean velocity profile obtained from simulations with and without the Vreman subgrid model.

5.2 Effect of Matching Location

First, the effect of solving the wall model over a range surpassing the distance from the wall to the first off-wall grid point is tested. There is a general agreement in the WMLES community that moving the matching location away from the wall improves the wall model performance. However, the author is not aware of any agreements on where to place the matching location. It is thus of interest to investigate the effect of changing the value of h_{wm}. Following the recommendations of Larsson et al. (2016) simulations using matching locations at 10 and 20 percent of the local boundary layer thickness are performed. Noting that the channel flow can be viewed as two turbulent boundary layers with a constant thickness equal to the the channel halfwidth, δ. Normalized in terms of the viscous wall units, the two matching locations tested in this thesis are thus located at a distance $\lesssim 1000^+$ units above the wall, well within the range where the use of the *Law of the wall* is reasonable.

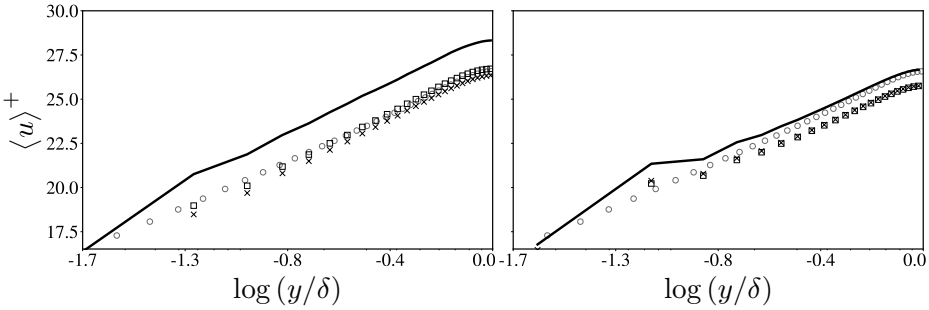

Figure 5.6: Mean velocity profile from simulations applying the algebraic wall model with different matching location obtained on a mesh with characteristic grid size $\Delta_c^+ = 100$. (Left) Hexaedron grid cells; (Right) Octahedron grid cells. (———), First off-wall grid point; (□), $h_{wm} = 0.10\delta$; (×), $h_{wm} = 0.20\delta$; (◯), DNS data.

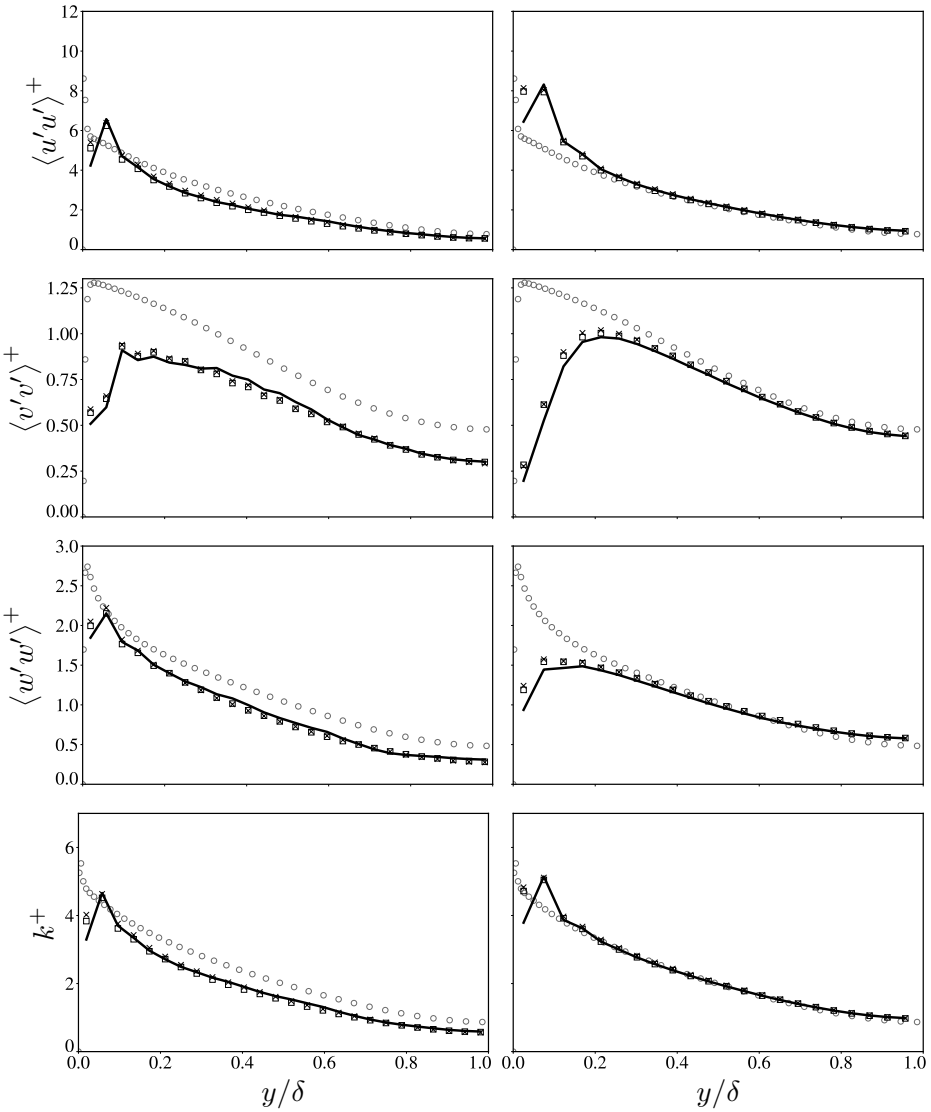

Figure 5.7: The diagonal components of the Reynolds stress tensor and the turbulent kinetic energy computed applying the algebraic wall model with different matching location h_{wm}. The grid has a characteristic cell size $\Delta_c^+ = 100$. (Left) Hexaedron grid cells; (Right) Octahedron grid cells. (———), First off-wall grid point; (□), $h_{wm} = 0.10\delta$; (×), $h_{wm} = 0.20\delta$; (◯), DNS data.

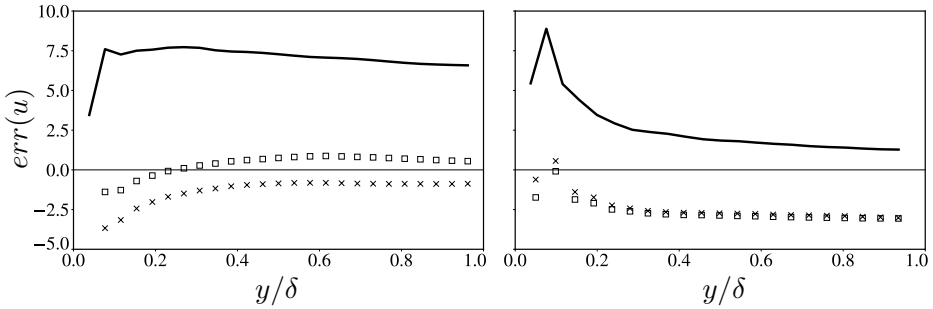

Figure 5.8: Relative error of the mean velocity profile computed applying the algebraic wall model with different matching location h_{wm}. The grid has a characteristic cell size $\Delta_c^+ = 100$. (Left) Hexaedron grid cells; (Right) Octahedron grid cells. (———), First off-wall grid point; (□), $h_{wm} = 0.10\delta$; (×), $h_{wm} = 0.20\delta$; (◯), DNS data.

The computed mean velocity profiles obtained on grids with $\Delta_c^+ = 100$ are presented in Figure (5.6). For the hexahedra grid we observe that the numerical results converge towards the DNS data when the wall model is fed the LES velocity sampled a distance $h_{wm} > \Delta_c/2$ above the wall. As reported in Table (5.2), the *Log-Layer Mismatch* is greatly reduced when moving the matching locations away from the wall. The resolved Reynolds stresses presented in Figure (5.7) are less sensitive, with only minor differences observed.

For the truncated octahedra grid one observes a similar down-shift of the predicted mean velocity $\langle u \rangle^+$ when abandoning the traditional practise of using $h_{wm} = \Delta y/2$. As shown by the relative error found in Figure (5.8), the estimated mean velocity is reduced by $\approx 5\% - 7\%$ regardless of grid topology. Close to the wall this down-shift clearly improves the accuracy. On the other hand, for simulations on the truncated octahedra meshes, the accuracy in the outer region worsens when employing $h_{wm} > \Delta_c/2$. At the center of the channel the mean velocity is under-predicted by approximately 2.5% compared to the

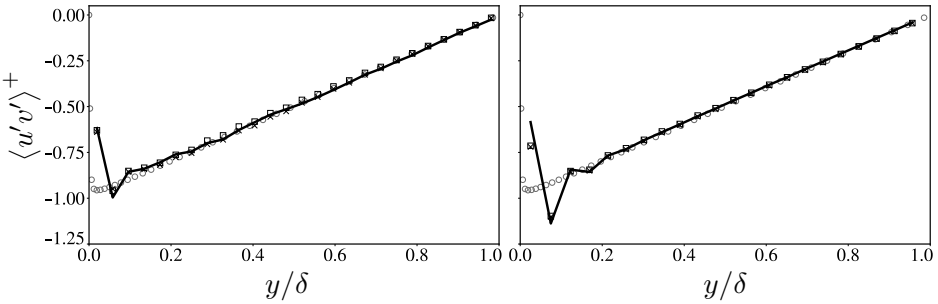

Figure 5.9: Reynolds shear stress computed applying the algebraic wall model with different matching location h_{wm}. The grid has a characteristic cell size $\Delta_c^+ = 100$. (Left) Hexaedron grid cells; (Right) Truncated Octahedron grid cells. (———), First off-wall grid point; (□), $h_{wm} = 0.10\delta$; (×), $h_{wm} = 0.20\delta$; (◯), DNS data.

Table 5.3: $LLM_{\%}$ in simulations employing the algebraic wall model fed the time filtered velocity at the first off-wall grid point. The grid has a characteristic cell size $\Delta_c^+ = 100$.

ϵ	Hex	Oct
1.0	7.14	3.34
0.5	6.44	1.49
0.25	5.22	1.47
0.1	5.44	1.43

DNS solution. However, the results presented in Table (5.2) show that the over all error, in terms of $LMM_{\%}$, is reduced with both $h_{wm} = 0.10\delta$ and $h_{wm} = 0.20\delta$. Similar to simulation on the hexahedra meshes, we observe no significant changes in the Reynolds stresses, as shown in Figure (5.7).

The resolved Reynolds shear stresses are shown in Figure (5.9). As for the diagonal components, changing the matching location seems to have little effect on the overall prediction of the Reynolds shear stress. Furthermore, we observe little to no correlation between the predicted near-wall shear stress and the $LLM_{\%}$.

5.3 Temporal Filtering

Next, the effect of the temporal filtering scheme presented by X. I. Yang, Park and Moin (2017) is considered. Figure (5.10) shows the computed mean velocity profiles obtained employing the temporal filter presented in Equation (4.6) with $\epsilon = 0.5, 0.25$ and 0.1 together with the non-filtered solution, equivalent to setting $\epsilon = 1.0$. The results presented are obtained on grids with characteristic cell size $\Delta^+ = 100$.

As found by X. I. Yang, Park and Moin (2017) we observe that the use of the present filtering technique reduces the strength of LLM. From the results presented in Table (5.3) we make the following observations; $LMM_{\%}$ drops with

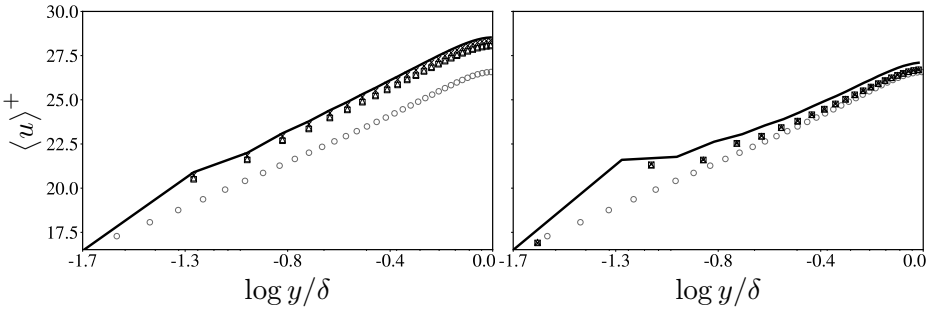

Figure 5.10: Mean velocity profile from simulations applying the algebraic wall model with time filtered input obtained on a mesh with characteristic grid size $\Delta_c^+ = 100$. (Left) Hexaedron grid cells; (Right) Truncated Octahedron grid cells. (———), Non filtered data ($\epsilon = 1.0$); (△), $\epsilon = 0.1$; (□), $\epsilon = 0.25$; (×), $\epsilon = 0.5$; (○), DNS data.

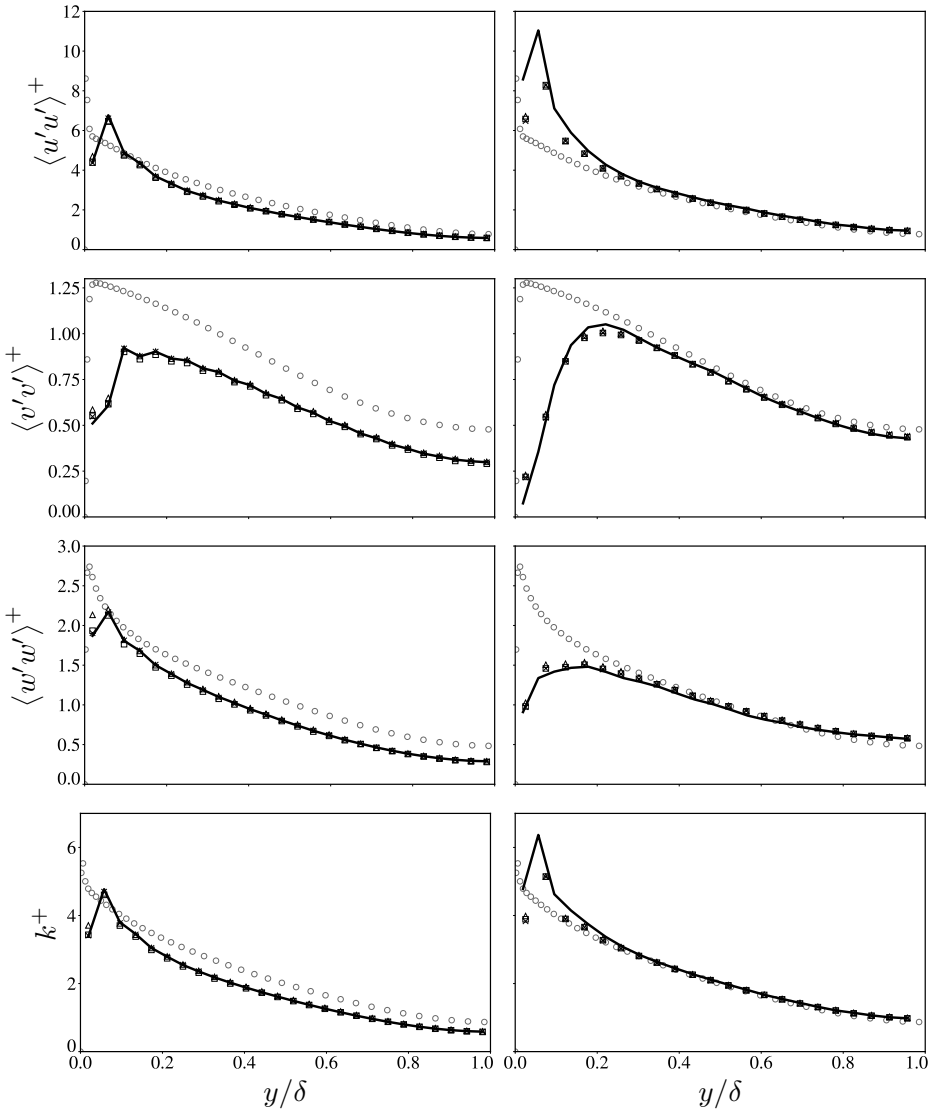

Figure 5.11: The diagonal components of the Reynolds stress tensor and the turbulent kinetic energy computed applying the algebraic wall model with time filtered input. The grid has a characteristic cell size $\Delta_c^+ = 100$. (Left) Hexaedron grid cells; (Right) Octahedron grid cells. (———), Non filtered data ($\epsilon = 1.0$);(△), $\epsilon = 0.1$; (□), $\epsilon = 0.25$; (×), $\epsilon = 0.5$; (○), DNS data.

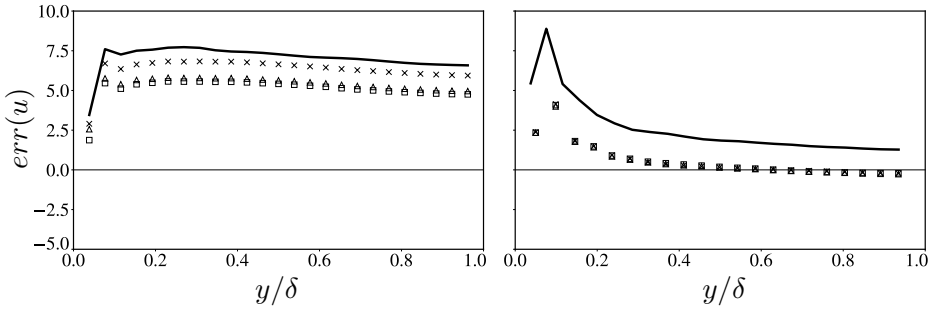

Figure 5.12: Relative error of the mean velocity profile from simulations applying the algebraic wall model with time filtered input obtained on a mesh with characteristic grid size $\Delta_c^+ = 100$. (Left) Hexaedron grid cells; (Right) Truncated Octahedron grid cells. (———), Non filtered data ($\epsilon = 1.0$);(△), $\epsilon = 0.1$; (□), $\epsilon = 0.25$; (×), $\epsilon = 0.5$.

≈ 2 percentage points with $\epsilon = 0.25$, regardless of the mesh topology. Further decreasing the filtering weights seems to have little effect on the strength of LLM, the magnitude remained small as we further decreased ϵ. The simulations carried out on the octahedra meshes seem to be less sensitive to the value of the filter weight compared to the results obtained from the hexahedra meshes. For the former, $LLM_{\%}$ decreases with less than ≈ 0.1 percentage points for $\epsilon < 0.5$. As noted by X. I. Yang, Park and Moin (2017), the observed reduction of LLM can not be explained by numerical error at the sampling point, as this remedy uses the LES solution sampled at the first off-wall grid point. The Reynolds normal stresses, found in Figure (5.12), are again found to be less affected by the filtering than the mean streamwise velocity.

Both the results presented in Table (5.3) and Figure (5.12) show that the predicted mean velocity profile from the simulations on the hexahedral grid slightly worsen when ϵ is decreased from 0.25 to 0.1. At this stage it is unknown to the author if this is due to unfortunate rounding errors or if this is a general

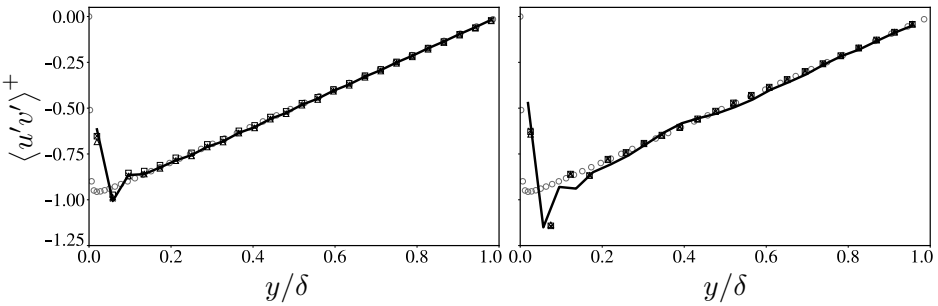

Figure 5.13: Reynolds shear stress computed using the algebraic wall model with time filtered input. The grid has a characteristic cell size $\Delta_c^+ = 100$. (Left) Hexaedron grid cells; (Right) Truncated Octahedron grid cells. (———), Non filtered data ($\epsilon = 1.0$); (△), $\epsilon = 0.1$; (□), $\epsilon = 0.25$; (×), $\epsilon = 0.5$; (◯), DNS data.

trend for the present filtering scheme when the filter weight becomes sufficiently small. Hence, it would be of interest to investigate the asymptotic behavior $\epsilon \to 0$ of the temporal filtering scheme. As simply setting the temporal weight to zero, or to a value close to zero, might give unreliable results due to numerical errors. The asymptotic analysis of the temporal filter uses Equation (4.6) as an ansatz.

By rewriting (4.6), the temporal filtered velocity fed to the wall model can be expressed according to Equation (5.11) when $n \to \infty$. That is, the wall model velocity u_{wm} at an arbitrary time step can be viewed as a weighted sum of all previous velocities fed to the wall model. The relative importance of the m^{th} time step being proportional to $\epsilon(1-\epsilon)^{n-m}$.

$$u^n_{wm} = \epsilon u^n_{LES} + (1-\epsilon)\epsilon u^{n-1}_{LES} + (1-\epsilon)^{n-2}\epsilon u^{n-2}_{LES} + (1-\epsilon)^3 \epsilon u^{n-3}_{LES} + ... \quad (5.11)$$

When $\epsilon \to 0$ the relative importance of two successive terms, m and $m+1$, approaches unity as shown below.

$$\lim_{\epsilon \to 0} \frac{\epsilon(1-\epsilon)^{n-(m+1)}}{\epsilon(1-\epsilon)^{n-m}} = \lim_{\epsilon \to 0} \frac{1}{(1-\epsilon)} = 1 \quad (5.12)$$

The infinite sum presented in Equation (5.11) can therefore be approximated as a uniform weighted sum of u^i_{LES} for sufficiently small ϵ. Thus, for sufficiently small ϵ, the temporal filtered wall model velocity u_{wm} can be approximated as the average of u_{LES}, according to Equation (5.13).

$$u_{wm} \approx \langle u_{LES} \rangle \quad (5.13)$$

Assuming the streamwise velocity to be non-negative, which is reasonable for the current case, Equation (5.14) follows from Equation (5.13) and (5.8). That is, as the filtering weight ϵ tends to zero, the time filtering scheme presented in Equation (4.6) is equivalent to fixing the modelled wall shear to the time average of τ_w.

$$\langle \tau_w \rangle = \rho \left(\frac{\kappa}{\ln(y^+) + B} \right)^2 \langle u_{wm} \rangle^2 \quad (5.14)$$

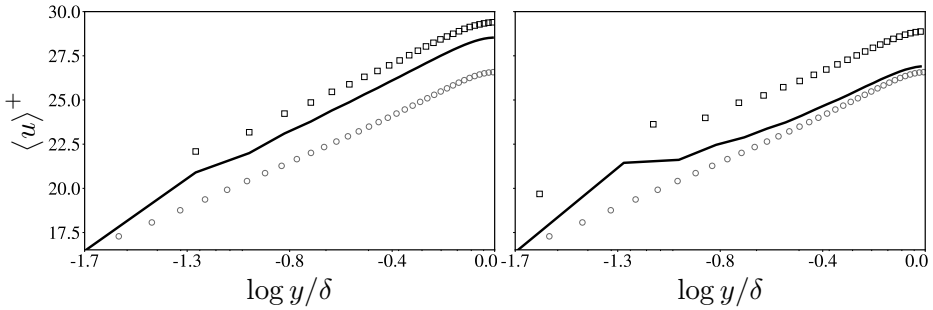

Figure 5.14: Mean velocity profile for simulations with fixed wall stress at solid boundaries on a mesh with characteristic grid size $\Delta_c^+ = 100$. (Left) Hexaedron grid cells; (Right) Truncated Octahedron grid cells. (———), Non filtered data ($\epsilon = 1.0$); (□), $\tau_{wm} = \langle \tau_w \rangle$; (◯), DNS data.

Table 5.4: $LLM_{\%}$ in simulations employing the algebraic wall model over a distance h_{wm} on grids with characteristic cell size $\Delta_c^+ = 100$.

Weighting	5-point stencil	9-point stencil
Uniform	7.13	6.63
Quadratic	6.72	6.98

Following the above analysis, we therefore investigate the asymptotic behavior, $\epsilon \to 0$, by modeling the wall stress according to Equation (5.15). We note that the flow is driven by a prescribed pressure gradient, which allows us to compute the mean wall shear stress apriori. Hence, we may employ such a simple wall model.

$$\tau_{wm} = \langle \tau_w \rangle \tag{5.15}$$

As seen in Figure (5.14) LLM worsens when employing the theoretical mean wall stress as a boundary condition. Both for the hexahedra and truncated octahedra grid topologies. Thus, one should expect that LLM increase when employing the temporal filtering scheme with small ϵ.

5.4 Spatial Filtering

Lastly, the effect of spatially filtering of the wall model input velocity is considered. The mean velocity profile obtained for simulations on a hexahedra mesh with characteristic cell size $\Delta_c^+ = 100$, employing the 5-point and 9-point stencils, with both uniform and quadratic weighting, are presented in Figure (5.15). In contrast to what was reported by Bou-Zeid, Meneveau and Parlange (2004) and X. I. Yang, Park and Moin (2017), the streamwise velocity profile computed with the filtered wall model deviates from the assumed logarithmic profile. As shown in Table (5.4), LLM remains large regardless of filter type.

The resolved Reynolds stresses are presented in Figure (5.16) and (5.17). As for the mean velocity profile, the spatial filtering of the wall model velocity seems to have little effect on the overall estimate of the resolved Reynolds

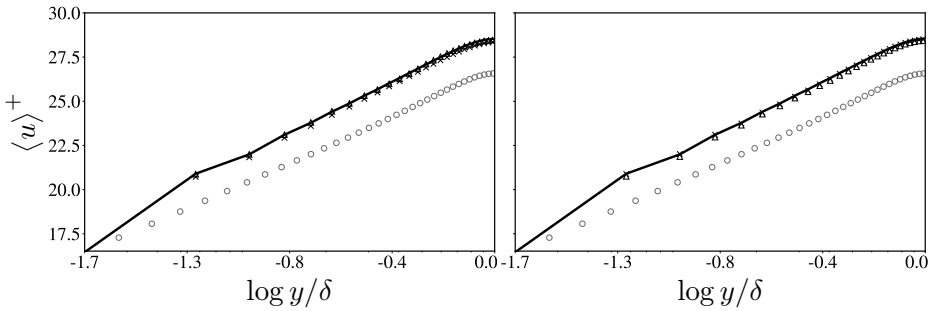

Figure 5.15: Mean velocity profile obtained with the spatially filtered wall model on a hexahedra mesh with characteristic grid size $\Delta_c^+ = 100$. (Left) 5-point stencil; (Right) 9-point stencil. (———), Non-filtered wall model; (△), Uniform weighting scheme; (×), Quadratic weighting scheme; (◯), DNS data.

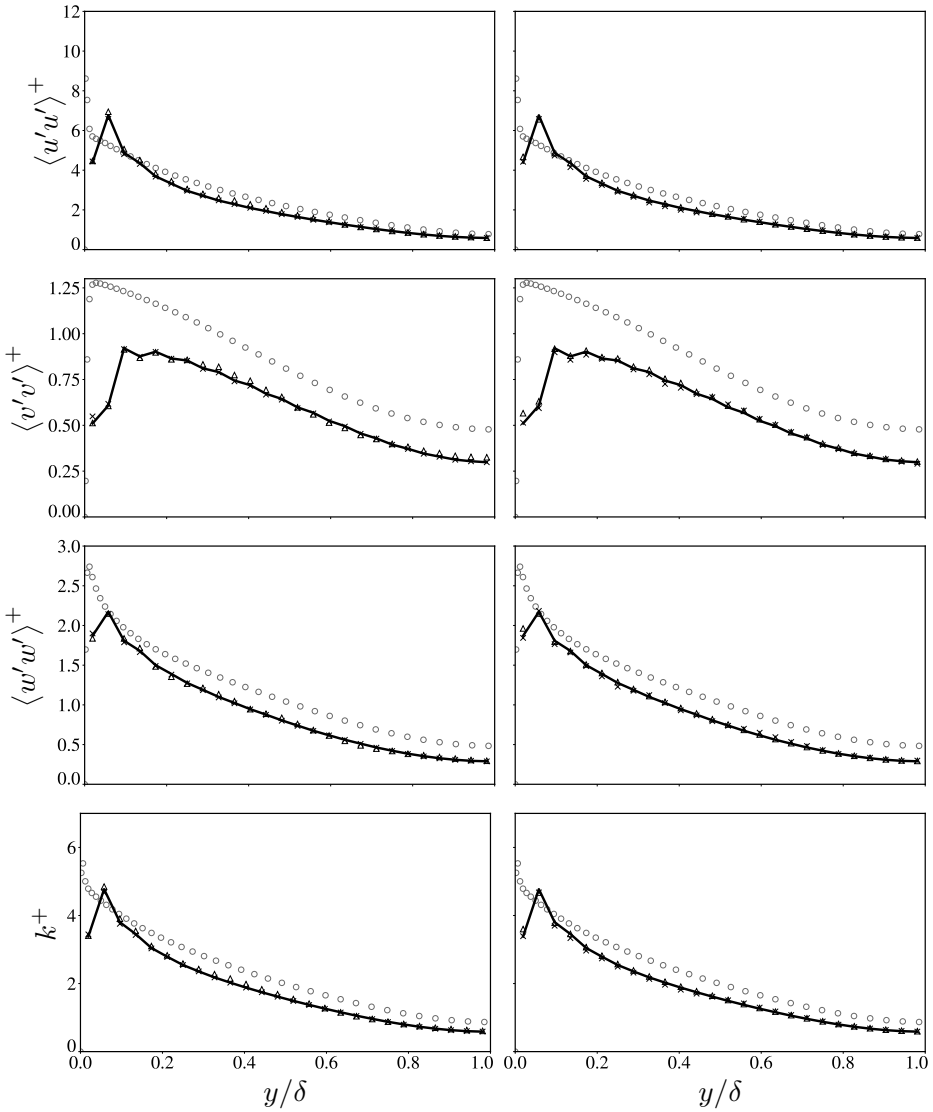

Figure 5.16: The diagonal components of the Reynolds stress tensor and the turbulent kinetic energy computed spatially filtered wall model on a hexahedra mesh with characteristic grid size $\Delta_c^+ = 100$. (Left) 5-point stencil; (Right) 9-point stencil. (———), Non-filtered wall model; (△), Uniform weighting scheme; (×), Quadratic weighting scheme; (◯), DNS data.

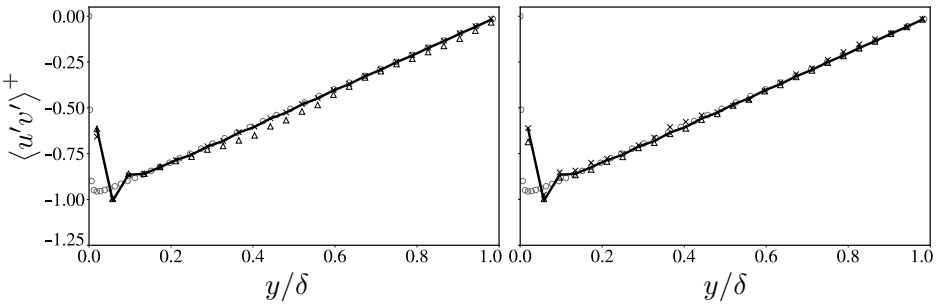

Figure 5.17: Reynolds shear stress computed using spatially filtered wall model on a hexahedra mesh with characteristic grid size $\Delta_c^+ = 100$. (Left) 5-point stencil; (Right) 9-point stencil. (———), Non-filtered wall model; (△), Uniform weighting scheme; (×), Quadratic weighting scheme; (◯), DNS data.

stresses. Although not shown, similar experiments were carried out on grids with truncated octehedra cell lattices. For these experiments a 7-point stencil was employed and both the uniform and quadratic weighting scheme was tested. Again, no noticeable improvement of the *Log-layer mismatch* was observed.

PART III

Discussion and Conclusions

CHAPTER 6

Discussion

The results presented in the previous chapter show that WMLES is influenced by the subgrid model, the grid topology, as well as the wall modelling approach. Of the two grid topologies tested the truncated octahedral seems to be the overall most accurate. However, the hexahedral meshes outperformed the octahedral grids in the near-wall region, both regarding the computed mean velocity and the Reynolds stresses. Generally, refining the mesh turned out to increase the magnitude of LLM while improving the velocity gradient. Simulations performed without the Vreman eddy viscosity model gave lower predictions of the mean velocity compared to simulations with subgrid modeling, independent of grid topology.

The results indicate that one may improve the accuracy of WMLES by departing from the traditional wall modeling approach. For all strategies tested, both the filtering schemes and the shifting of the matching location seems to reduce the measured LLM. The latter being the most effective remedy. Of the filtering techniques, the temporal filter seems to be the most effective. However, none of the techniques seem to solve the problem completely.

The present chapter seeks to explain how grid topology, wall modelling strategy and eddy viscosity affect the near wall behavior of the WMLES solution and why they affect the magnitude of LLM. To reduce the scope of the following chapter the analysis only considers the cases summarized in Table (6.1). However, these are found to give a representative picture of the general trends observed for the remaining simulations performed in this thesis.

6.1 Effect of Subgrid Modeling

The results presented in Section (5.1) indicate that one may reduce the magnitude of LLM in a turbulent channel by setting ν_e to zero, when employing the current numerical scheme. However, closer scrutiny of the mean velocity profiles presented in Figure (5.5) shows that turning off the subgrid model deteriorates the accuracy of the computed velocity gradient. Furthermore, turning off the subgrid model also worsens the predicted Reynolds stresses, as seen in Figure (6.1).

Figure (6.1) shows the turbulent kinetic energy and the Reynolds shear stress for simulations with and without employing the Vreman subgrid model. In the center of the channel the simulations are indistinguishable. The Vreman subgrid model is defined in terms of the filtered strain rate tensor, $\bar{S}_{ij}$, which for a fully developed channel flow is proportional to the mean streamwise velocity

Table 6.1: Descriptions and abbreviations for the simulations studied in the present chapter. If not specified the simulation is carried out on a hexahedral mesh with characteristic cell size $\Delta_c^+ = 100$.

Abbreviation	Description
NFil	Non-filtering algebraic wall model on a hexahedral mesh with characteristic cell size $\Delta_c^+ = 100$
NFil-0	Non-filtering algebraic wall model (not employing the Vreman subgrid model)
NFil-200	Non-filtering algebraic wall model on a hexahedral mesh with characteristic cell size $\Delta_c^+ = 200$
NFil-Oct	Non-filtering algebraic wall model on a truncated octahedral mesh with characteristic cell size $\Delta_c^+ = 100$
WN	Algebraic wall model fed the LES solution sampled a distance $h_{wm} = 0.05\delta$ above the wall
WP	Algebraic wall model fed the average velocity computed using a nine-point-stencil employing the uniform weighting scheme
TEMP	Algebraic wall model employing a temporal filter with $\epsilon = 0.25$
FIXED	Employing a fixed wall shear stress ($\tau_{wm} = 0.25$) as a boundary condition

gradient. Since $\langle du/dy \rangle$ is negligible in the *outer-layer* the solution should, at least in theory, be less sensitive to the subgrid model at the core of the channel. Closer to the wall the solutions diverge, and large discrepancies are observed for the simulation without subgrid modeling. This is somewhat expected as the viscous shear stress dominates at the wall. Further, since the eddy viscosity computed by the Vreman model is non-negative, turning off the model should lead to a decrease of the viscous dissipation rate and viscous diffusion rate, which may explain the increase of the turbulent kinetic energy observed in the near wall region.

It is not obvious to the author why the simulations employing the Vreman modelling produce the largest mismatch, as one expects the modeling of the subgrid stresses to improve the accuracy of the numerical scheme. As turning off the subgrid model, in general, degrades the solutions of all flow quantities except for the mean velocity profile, the observed reduction of LLM might be caused by fortunate cancellations of errors. Alternatively, as noted by Nicoud, Toda et al. (2011), the turbulent stresses should decay cubically in the vicinity of solid boundaries. However, they showed that the asymptotic behavior of the Vreman modeled is linear in terms of the wall normal distance. Hence, the discrepancies observed when employing the Vreman model can possible be

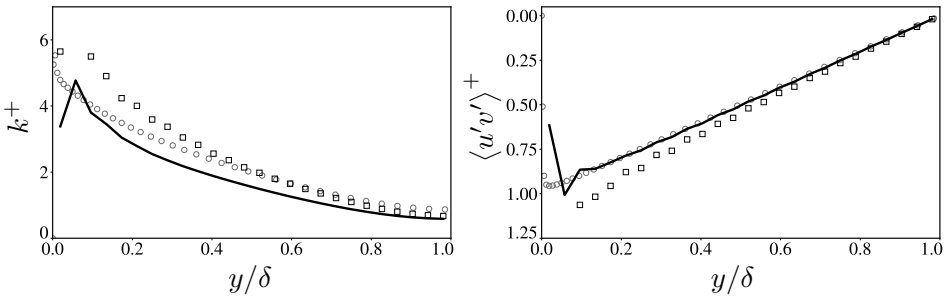

Figure 6.1: The turbulent kinetic energy (Left), and Reynolds shear stress (Right) in simulations applying the non-filtered algebraic wall-model with and without subgrid modeling on a hexahedral mesh with $\Delta_c^+ = 100$. (———), (NFil); (□), (NFil-0); (◯), DNS data.

attributed to over-predictions of the eddy viscosity in in the near-wall region for the girds employed in this theses. It should be emphasised that this does not discredit the Vreman subgrid model in general.

6.2 Near-Wall Flow Behavior

As the near-wall behavior of WMLES is crucial to the predicted velocity field, this section is dedicated to the discussion of the statistics sampled at the first off-wall grid point or at the matching location h_{wm}, presented in Table (6.2).

As noted by Bou-Zeid, Meneveau and Parlange (2004), the mean shear stress imposed by the algebraic wall model is proportional to $\langle u^2 \rangle$, while the *Log-Law* is validated in an average sense. That is, the true wall stress $\langle \tau_w^{Log-Law} \rangle$ scales as $\langle u \rangle^2$. Since $\langle u^2 \rangle$ and $\langle u \rangle^2$ are in general unequal they argued that the magnitude of LLM is proportional to $\langle u^2 \rangle / \langle u \rangle^2$. However, the results presented in Table (6.2) show only negligible changes of the relative magnitudes for all but the simulation with shifted matching location. Thus we can conclude that the reasoning of Bou-Zeid, Meneveau and Parlange (2004) do not, in general, explain the occurrence of LLM.

The results presented in Table (6.2) indicate that employing spatial and temporal filtering strategies reduces, to some extent, the magnitude of LLM. As neither of the two filtering schemes introduce any additional information of the LES solution away from the wall, the effect of these filters can not be attributed to an increased accuracy of the LES at sampling point(s). Filtering may remove some numerical noise, improving the quality of u_{wm}. However, it is not believed that this is the main mechanisms for the observed reduction of LLM, since filtering of incorrect data will, in general, yield poor results. The improvements observed thus imply that LLM is not solely attributed to the local resolution of the WMLES. It is therefore reasonable to conclude that the argument made by Kawai and Larsson (2012) does not suffice as an explanation for LLM.

From the streamwise momentum equation for a fully developed channel flow at sufficiently high Reynolds numbers it follows that the mean total shear stress is balanced by the mean pressure gradient according to Equation (6.1).

Table 6.2: Summary of relevant near wall quantities. All quantities presented are normalized in terms of wall units.

	NFil	WN	WP	TEMP	FIXED
$LLM_{\%}$	7.14	1.24	6.63	5.22	10.58
$\left\langle \tau_{wm} u'_{y=\Delta_c/2} \right\rangle^+$	0.47	0.09	0.35	0.41	$4.65{\cdot}10^{-10}$
$\left\langle u \right\rangle^+_{y=\Delta_c/2}$	16.37	15.27	16.44	16.41	18.01
$\left\langle u'v' \right\rangle^+_{y=\Delta_c/2}$	-0.62	-0.64	-0.68	-0.65	-0.67
$\left\langle \nu_e \right\rangle^+_{y=\Delta_c/2}$	12.22	13.48	12.66	12.62	12.90
$\frac{\left\langle u^2 \right\rangle}{\left\langle u \right\rangle^2}\Big\vert_{y=h_{wm}}$	1.017	1.009	1.016	1.017	-
$\left\langle \frac{du}{dy} \right\rangle^+_{y=\Delta_c/2}$	0.0232	0.0209	0.0217	0.0221	0.0203

$$\tau^+_{Total} = -\left\langle u'v' \right\rangle^+ + \left\langle (1+\nu_e^+)\frac{du}{dy}^+ \right\rangle = \left\langle \tau_w \right\rangle^+ \left(1 - \frac{y}{\delta}\right) \tag{6.1}$$

Evaluating the momentum balance at the first off-wall grid point, noting that the mean wall shear stress is equal for all simulations performed herein, it follows that a decrease of the Reynolds shear stress at $y = \Delta_c/2$ leads to an increase of the near-wall viscous shear stress. Following this line of thought X. I. Yang, Park and Moin (2017) argued that LLM is a consequence of wrongly predicting the Reynolds shear stress $\left\langle u'v' \right\rangle$ in the near-wall region caused by unphysically high correlations of the instantaneous LES solution and the modelled wall stress. Hence LLM can be remedied by disrupting the coupling of the wall stress and the velocity field.

The results presented in Table (6.2) show that one may reduce the coupling between the modeled wall stress and the local LES solution $\left\langle \tau_{wm} u'_{y=\Delta_c/2} \right\rangle$ by filtering the wall model velocity or by shifting the matching location further from the wall. However, the results show no clear correlation between the magnitude of the Reynolds shear stress and $\left\langle \tau_{wm} u'_{y=\Delta_c/2} \right\rangle$. Further, the magnitude of $\left\langle u'v' \right\rangle$ seems to have little to no effect on the near-wall velocity gradient.

As a part of their argumentation, X. I. Yang, Park and Moin (2017) assumed that the eddy viscosity at the first off-wall grid point remains almost constant independent of the wall modeling approach. The LES eddy viscosity at the first off-wall grid point, reported in Table (6.2), shows that this is not the case for the present WMLES. In general we observe that the filtered WMLES solutions, which predict smaller values of $\left\langle u'v' \right\rangle_{y=\Delta_c/2}$ produce larger values of ν_e. Hence, it seems that changes in the Reynolds shear stress is balanced by the magnitude of $\left\langle du/dy \right\rangle$ as-well as the value of the eddy viscosity. Closer scrutiny of the near wall statistics presented above shows that the simulations with the smallest velocity gradients coincide with the simulations with the smallest correlation between the modeled wall stress and the instantaneous LES solution. Thus the results indicate that the near wall velocity gradient is related to $\left\langle \tau_{wm} u'_{y=\Delta_c/2} \right\rangle$,

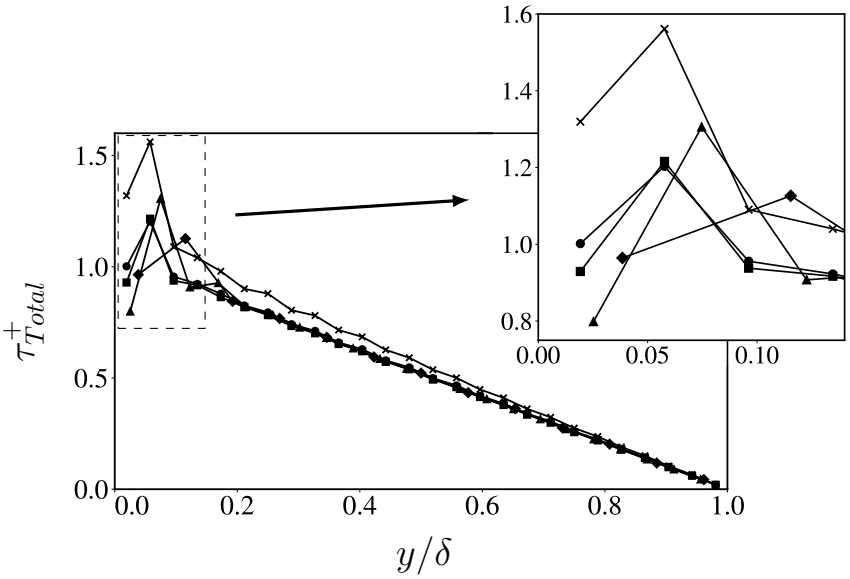

Figure 6.2: The total shear stress balance obtained from WMLES of the turbulent channel. (—■—), NFil; (—◆—), NFil-200; (—×—), NFil-0; (—▲—), NFil-Oct; (—●—), WP.

but not by way of the Reynolds shear stress as suggested by X. I. Yang, Park and Moin (2017).

The total shear stress profiles from WMLES are shown in Figure (6.2). The WMLES satisfy the momentum equation at the core of the channel, independent of wall model, subgrid model, and grid topology. On the other hand, large discrepancies are observed in the near-wall region. The greatest errors are observed in the simulations without subgrid modeling. A distinct peak is observed for all simulations at the second off-wall grid point. There seems to be no relation between the magnitude of this peak and discrepancies in the predicted velocity profile. The results however indicate that LLM may be connected with the absolute change in the total shear stress from the first to the second off-wall grid point. In general, an increase of $\left|\tau^+_{Total}|_{y=3\Delta_c/2} - \tau^+_{Total}|_{y=\Delta_c/2}\right|$ imply a rise of the near-wall LLM.

As noted in Section (5.3) LLM worsens when employing the theoretical mean wall stress as a boundary condition. However, as shown in Table (6.2), the simulation with fixed wall shear at the boundary yields the smallest velocity gradient at the first off-grid point. In Figure (6.3) the normalized mean velocity gradient is plotted over the *Log-layer* in terms of the overshoot Φ_m, defined in Equation (6.2) (Brasseur and Wei 2010).

$$\Phi_m = K\frac{y}{u_\tau}\left\langle\frac{d\bar{u}}{dy}\right\rangle \tag{6.2}$$

Clear discrepancies in Φ_m shows up for the WMLES independent of wall modelling approach. In general, the WMLES overpredict the velocity gradient within the *Log-layer* except at the first off-wall grid point, where all but the non-filtered solution significantly underpredict $\langle du/dy\rangle$. The solution employing

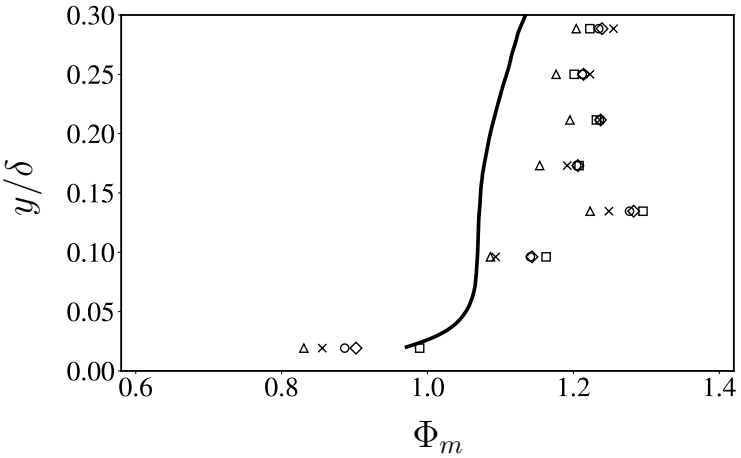

Figure 6.3: Comparison of the overshoot from WMLES and DNS simulations plotted against the wall normal distance normalized with respect to the boundary layer thickness. Data are presented for measurements obtained within the *Log-layer*. (———), DNS data obtained by M. Lee and R. Moser (2015); (□), NFil; (×), WN; (○), WP; (◇), TEMP; (△), FIXED.

a fixed shear stress at the wall consistently yields the smallest value of Φ_m. Hence, we may not attribute the rise in LLM when employing this boundary condition to an increased near-wall velocity gradient. However, the mean near-wall velocity presented in Table (6.2) shows that $\langle u \rangle_{y=\Delta_c/2}$ is $\approx 10\%$ larger for the solution with a fixed wall stress condition compared to the remaining WMLES solutions.

Using the formulation for the streamwise velocity fluctuations presented in Marusic, Mathis and Hutchins (2010) as an ansatz, Mathis et al. (2013) derived a predictive model for the normalized fluctuating wall stress, $\tau_{wp}^{+} = \tau_{wp}/(\rho u_\tau^2)$, only requiring the velocity obtained from the *Log-layer*. By tuning the modelling parameters using DNS data, they found that the proposed model was able to reconstruct a realistic time-series of the wall stress. As the proposed model only needs the off-wall velocity to predict the instantaneous wall shear stress, it seems likely that the fluctuating wall shear stress and the near-wall velocity are, to some extent, correlated. This correlation implies that the wall stress respond immediately to changes in the velocity, instantaneously draining the near-wall region of turbulent kinetic energy. As pointed out by X. I. Yang, Park and Moin (2017), by employing a fixing shear stress boundary condition one removes all correlation between the wall model and the instantaneous LES solution. Thus, by fixing the wall shear stress, one inevitably make the near-wall LES solution too energetic, which might explain the unreasonable high velocity close to the wall.

6.3 Revisiting the *Log-Law*

Next, the effect of employing an algebraic wall model based on the *The Law of The Wall* is considered. Employing the algebraic wall model given in Equation (4.3), it follows that the modeled instantaneous wall shear stress can be computed

as shown below.

$$\tau_{wm} = \rho \frac{u_{wm}^2}{\Big(C + 0.5K^{-1} \ln \tau_{wm}\Big)^2} \tag{6.3}$$

Here the constant C, defined in Equation (6.4), is introduced for reasons of convenience.

$$C = B + K^{-1} \ln \frac{h_{wm}}{\nu\sqrt{\rho}} \tag{6.4}$$

As shown in Appendix (A) one may rewrite Equation (6.3) as (6.5) by first decomposing the wall shear stress into a mean and a fluctuating part, $\tau_{wm} = T_{wm} + \tau_{wm}^{'}$, and Taylor expanding the natural logarithm $\ln\Big(T_{wm} + \tau_{wm}^{'}\Big)$ around $\tau_{wm}^{'} = 0$.

$$T_{wm} + \tau_{wm}^{'} = \rho \frac{u_{wm}^2}{\Big(C + 0.5K^{-1}\Big(\ln T_w + \tau_{wm}^{'}/T_w + \cdots\Big)\Big)^2} \tag{6.5}$$

One should note that the Taylor series of $\ln\left(T_{wm} + \tau_{wm}^{'}\right)$ converges if and only if the normalized fluctuations $|\tau_{wm}^{'}/T_{wm}| < 1$ (Ahlfors 1966), which is in general true for WMLES. After some simple algebraic manipulations and averaging of the above equation, it follows that the modelled mean wall shear stress can be expressed as Equation (6.6).

$$\begin{aligned} T_{wm} =& \rho \frac{\Big\langle u_{wm} \Big\rangle^2 + \Big\langle u_{wm}' u_{wm}' \Big\rangle}{\Big(C + 0.5K^{-1} \ln T_{wm}\Big)^2} \\ &+ \Big\langle \tau_{wm}^{'} \tau_{wm}^{'} \Big\rangle \frac{\Big(C/2 + 0.25K^{-1}\Big(1 - \frac{3}{2}\ln T_{wm}\Big)\Big)}{KT_{wm}\Big(C + 0.5K^{-1}\ln T_{wm}\Big)^2} + \mathcal{O}({\tau_{wm}^{'}}^3) \end{aligned} \tag{6.6}$$

The *Log-Law* was developed to be used, and is in principle only valid, in an average sense (Bou-Zeid, Meneveau and Parlange 2004). Thus the theoretical mean shear stress $\Big\langle \tau_w^{Log-Law} \Big\rangle$ can be approximated according to Equation (6.7).

$$\Big\langle \tau_w^{Log-Law} \Big\rangle = \rho \frac{\Big\langle u_{wm} \Big\rangle^2}{\Big(C + 0.5K^{-1} \ln \tau_w^{Log-Law}\Big)^2} \tag{6.7}$$

Assuming the higher order fluctuations of the wall stress $\tau_{wm}^{'}$ to be negligible, it follows from Equation (6.6) and (6.7) that the modeling error of the mean wall stress is given by Equation (6.8).

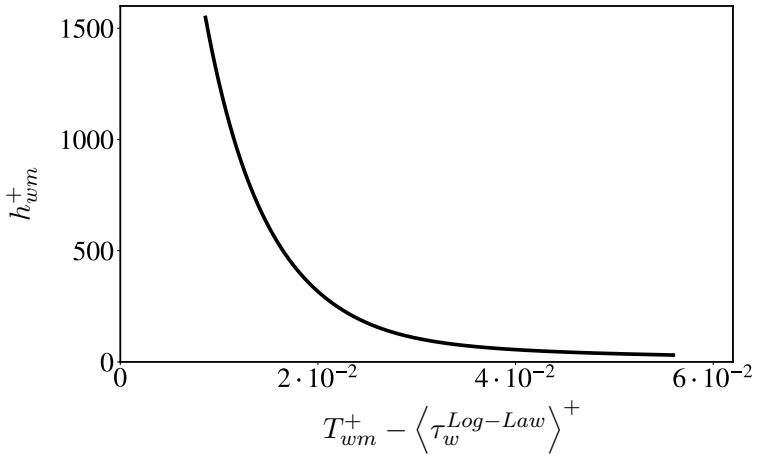

Figure 6.4: The modeling error computed from the DNS data obtained by M. Lee and R. Moser (2015) as a function of the wall model height. The error is computed over the range for which the *Log-Law* is assumed valid.

$$T_{wm} - \left\langle \tau_w^{Log-Law} \right\rangle \approx \rho \frac{\left\langle u'_{wm} u'_{wm} \right\rangle}{\left(C + 0.5 K^{-1} \ln T_{wm} \right)^2} \tag{6.8}$$

Figure (6.4) presents the normalized modeling error $T^+_{wm} - \left\langle \tau_w^{Log-Law} \right\rangle^+$ computed with the DNS data obtained by M. Lee and R. Moser (2015) as a function of the wall model height h^+_{wm}. Since the wall model velocity u_{wm} is undefined in the DNS, the velocity fluctuations $\left\langle u'_{wm} u'_{wm} \right\rangle$ are estimated from the fluctuations of the wall parallel velocity components sampled at $y = h_{wm}$, that is, $\left\langle u'_{wm} u'_{wm} \right\rangle = \left\langle u'u' \right\rangle\big|_{y=h_{wm}} + \left\langle w'w' \right\rangle\big|_{y=h_{wm}}$. The error is computed over the range $h^+_{wm} > 30$ and $h_{wm} < 0.3\delta$, where the *Log-Law* is assumed valid.

The results presented in Figure (6.4) show that the modeling error decreases monotonically with increasing wall model height. This is in line with the observations made by Kawai and Larsson (2012, that LLM decreases as h_{wm} increases. One should note that the analysis presented in this section only considers the wall model formulation of the *Law of The Wall*. The discrepancies observed can thus not be attributed to subgrid modeling errors or to poorly

Table 6.3: The modeling error computed from WMLES data. The modeling error and $LLM_{\%}$ for the the solutions employing the algebraic wall model and the Vreman subgrid model are presented.

	NFil	WN	WP	TEMP
$LLM_{\%}$	7.14	1.24	6.63	5.22
$T^+_{wm} - \left\langle \tau_w^{Log-Law} \right\rangle^+$	$2.53 \cdot 10^{-2}$	$1.57 \cdot 10^{-2}$	$2.46 \cdot 10^{-2}$	$2.40 \cdot 10^{-2}$

resolved LES solutions in the near-wall region as implied by Kawai and Larsson (2012) and Wu and Meyers (2013). Hence, the results suggest that the algebraic wall model introduces unavoidable modeling errors. Note that the error is non-negative, meaning that the computed wall stress applying the instantaneous LES solution is generally too large.

Table (6.3) shows the modeling error for four different wall modeling approaches. Similar to the results obtained with the DNS data, increasing the wall model height also reduces the modeling error in WMLES. However, no appreciable changes are observed when comparing the modeling errors for the non-filtered, the spatial filtered and the temporal filtered solutions.

In general, for $y^+ > \Delta_c^+/2$, the relative magnitude of the turbulent fluctuation, $\propto \langle u^{'} u^{'} \rangle / \langle u \rangle^2$, decreases monotonically with increasing wall distance. Thus, by moving the matching location beyond the first off-wall grid point one makes the modelled wall shear stress less sensitive to the fluctuations of the velocity field. I.e. one reduces the contribution of $\langle u'_{wm} u'_{wm} \rangle$ to the total modelled wall stress. From Equation (6.8) it follows that the modeling error should decrease. However, by rewriting the expression for the magnitude of the turbulent fluctuation according to Equation (6.9), it follows that the modeling error is proportional to $\langle u^2 \rangle / \langle u \rangle^2$, which is exactly the argument made by Bou-Zeid, Meneveau and Parlange (2004). As noted earlier, this is not a complete explanation for the occurrence of LLM. It is therefore believed that the higher order fluctuating wall stresses are nonnegligible and should be included in further analysis.

$$\frac{\langle u^{'} u^{'} \rangle}{\langle u \rangle^2} = \frac{\langle u^2 \rangle - \langle u \rangle^2}{\langle u \rangle^2} = \frac{\langle u^2 \rangle}{\langle u \rangle^2} - 1 \tag{6.9}$$

6.4 The Discretized Equations

All conclusions made so far are based on the continuous transport equations. However, the velocity field obtained by WMLES resides in a discrete space. The solution is thus valid only in a discrete sense. It is therefore meaningful to investigate the problem of LLM in terms of the discretized equations that the WMLES solution satisfies.

Assuming the density ρ to be constant, the semi-discrete form of the numerical scheme presented in Ambo et al. (2020), can be expressed according to Equation (6.10).

$$V_{cv} \frac{\partial \tilde{u}_i}{\partial t} + \sum_{IF} \tilde{u}^f \frac{\tilde{u}_i^{cv} + \tilde{u}_i^{nbr}}{2} + V_{cv} \frac{\partial \tilde{p}}{\partial x_i} + \sum_{BF} \tilde{\tau}_i A_{bf} + \sum_{IF} \tilde{\nu}^f \frac{\tilde{u}_i^{cv} - \tilde{u}_i^{nbr}}{2} = 0 \tag{6.10}$$

Here $\tilde{u}, \tilde{p}$ and $\tilde{\tau}$ denote the instantaneous values of the discrete velocity field, pressure and wall shear, respectively. Further, IF, BF and nbr denote the internal faces, boundary faces with area A_{bf}, and the velocity in the grid cells adjacent to the control volume cv, respectively. The volume of the grid cell is denoted by V_{cv}, and $\tilde{\nu}^f$, defined in Equation (6.11), represents the kinematic viscosity at an internal face with area A_f and is a function of time and space.

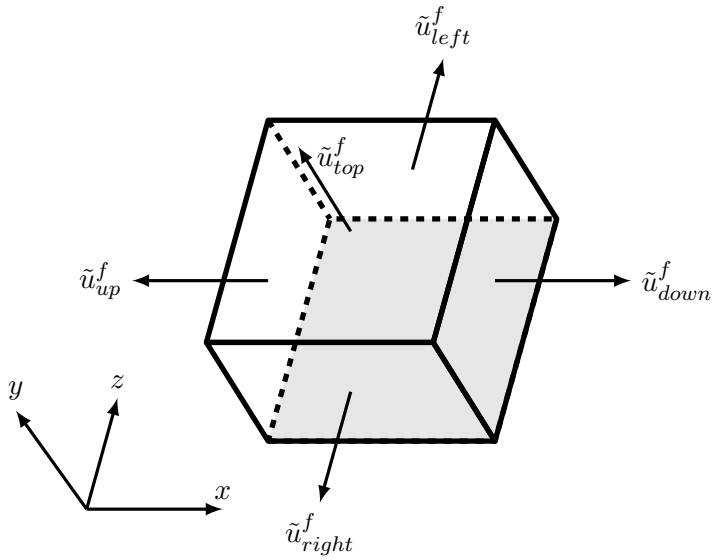

Figure 6.5: Illustration of a hexahedron boundary cell and the streamwise flux velocities $\tilde{u}^f_{up}$ and $\tilde{u}^f_{down}$, the spanwise flux velocities $\tilde{u}^f_{left}$ and $\tilde{u}^f_{right}$ and wall normal flux velocity $\tilde{u}^f_{top}$.

$$\tilde{\nu}^f = \frac{A_f}{\Delta x}\left(\nu + \tilde{\nu}^f_e\right) \tag{6.11}$$

In the above equation, Δx denotes the the cell size and $\tilde{\nu}^f_e$ is the face eddy viscosity. The flux velocity $\tilde{u}^f$, is defined on the face, as illustrated in Figure (6.5), and satisfies the divergence free constraint given in Equation (6.12).

$$\sum_{IF} \tilde{u}^f = 0. \tag{6.12}$$

Even though it is referred to as a velocity, $\tilde{u}^f$ is in reality a mass flux, hence $\tilde{u}^f \propto \tilde{u}^{cv} A_f$. Ignoring the pressure projection step, assuming it is used to enforce Equation (6.12), the semi-discrete RANS equation can be expressed as shown below.

$$V_{cv}\frac{\partial U^{cv}_i}{\partial t} + \sum_{IF}\frac{U^f U^{cv}_i + U^f U^{nbr}_i}{2} + \sum_{IF}\frac{\left\langle u^f u^{cv}_i\right\rangle + \left\langle u^f u^{nbr}_i\right\rangle}{2} + \sum_{IF} N^f \frac{U^{cv}_i - U^{nbr}_i}{2\Delta x_i}$$
$$+ \sum_{IF}\left(\left\langle \nu^f u^{cv}_i\right\rangle - \left\langle \nu^f u^{nbr}_i\right\rangle\right) + V_{cv}\frac{\partial P}{\partial x_i} + \sum_{BF} T_i A_f = 0 \tag{6.13}$$

In the above equation capital letters denote the temporal average, while lower case letters denote the fluctuating fields. Subtracting the semi-discrete RANS equations from Equation (6.10), applying the chain rule, and averaging, yields the numerical transport equation for the Reynolds stresses presented in Equation (6.14). A detailed description of the derivation is found in Appendix (C).

$$V_{cv}\frac{\partial R_{ij}}{\partial t} + \tilde{\mathcal{A}}_{ij} = -\tilde{\mathcal{P}}^s_{ij} - \tilde{\mathcal{P}}^\tau_{ij} - \tilde{\mathcal{R}}_{ij} - \tilde{\mathcal{T}}_{ij} - \tilde{\mathcal{V}}_{ij} \tag{6.14}$$

Here, $\tilde{\mathcal{A}}_{ij}, \tilde{\mathcal{P}}^s_{ij}, \tilde{\mathcal{R}}_{ij}$ and $\tilde{\mathcal{T}}_{ij}$, defined below, represent the numerical equivalents to the advection, production, turbulent transport and pressure redistribution terms found in the continuous transport equation of the Reynolds stress tensor. $\tilde{\mathcal{V}}_{ij}$[1] represents the viscous terms, that is the numerical viscous dissipation rate and viscous diffusion rate. The term $\tilde{\mathcal{P}}^\tau_{ij}$ acts like a production term for the turbulent energy and is caused by correlations between the wall shear and the velocity at the first off-wall gird point. Due to the no-slip and impermeability conditions, the fluctuating velocity field vanishes at the wall, thus $\langle u_j \tau_i \rangle\big|_{y=y_{wall}}$ is zero in real fluid flows. The term is therefore a product of the discretisation process. It is, however, not given that this term should be zero in WMLES as the numerical model computes the correlation between the wall stress and the velocity at $y = \Delta_c/2$. As argued earlier, these quantities may, to some degree, be correlated in real fluid flows. What the value should be can only be determined by DNS or experiments and is not within the scope of this thesis.

$$\tilde{\mathcal{A}}_{ij} = \sum_{IF} U^f \frac{\langle u^{cv}_j u^{nbr}_i \rangle + \langle u^{cv}_i u^{nbr}_j \rangle}{2} \qquad \text{Advection}$$

$$\tilde{\mathcal{P}}^s_{ij} = \sum_{IF} \left(\langle u^f u^{cv}_j \rangle \frac{U^{nbr}_i}{2} + \langle u^f u^{cv}_i \rangle \frac{U^{nbr}_j}{2} \right) \qquad \text{Production}$$

$$\tilde{\mathcal{P}}^\tau_{ij} = \sum_{BF} \langle u^{cv}_j \tau_i + u^{cv}_i \tau_j \rangle A_f \qquad \text{Production due to wall shear}$$

$$\tilde{\mathcal{R}}_{ij} = V_{cv} \left(\left\langle u^{cv}_j \frac{\partial p}{\partial x_i} \right\rangle + \left\langle u^{cv}_i \frac{\partial p}{\partial x_j} \right\rangle \right) \qquad \text{Velocity-pressure gradient}$$

$$\tilde{\mathcal{T}}_{ij} = \sum_{IF} \frac{\langle u^f u^{cv}_j u^{nbr}_i \rangle + \langle u^f u^{cv}_i u^{nbr}_j \rangle}{2} \qquad \text{Turbulent transport rate}$$

Next, the semi-discrete RANS equation for a fully-developed channel flow on a structured Cartesian grid is considered. In this case the mean velocity field reduces to $U = (U(y), 0, 0)$. The flow is homogeneous in the streamwise and spanwise directions, which implies that the stresses $\langle u_1 u_3 \rangle$ and $\langle u_2 u_3 \rangle$ are exactly zero. Furthermore, the flux velocity $\tilde{u}_f$ at the internal faces of a boundary node is defined according to Equation (6.15).

$$\begin{aligned}
\tilde{u}^f_{up} &= \frac{1}{2}\left(\tilde{u}^{cv}_1 + \tilde{u}^{up}_1\right) A_f \\
\tilde{u}^f_{down} &= \frac{1}{2}\left(\tilde{u}^{cv}_1 + \tilde{u}^{down}_1\right) A_f \\
\tilde{u}^f_{left} &= \frac{1}{2}\left(\tilde{u}^{cv}_3 + \tilde{u}^{left}_3\right) A_f \\
\tilde{u}^f_{right} &= \frac{1}{2}\left(\tilde{u}^{cv}_3 + \tilde{u}^{right}_3\right) A_f \\
\tilde{u}^f_{top} &= \frac{1}{2}\left(\tilde{u}^{cv}_2 + \tilde{u}^{top}_2\right) A_f
\end{aligned} \tag{6.15}$$

[1] Due to time limitations this term has not been derived.

The superscripts $(.^{up})$, $(.^{down})$, $(.^{left})$, $(.^{right})$, and $(.^{top})$ denote the velocity in the cells sharing the face for which the respective flux velocity is defined. The kinematic viscosity $\tilde{\nu}^f$ can be decomposed in a similar fashion. Noting that the only two non-zero mean flux velocities are U^f_{up} and U^f_{down}, the streamwise semi-discrete RANS equation can be approximated as Equation (6.16). For more details on the derivation of the semi-discrete RANS equations see Appendix (B).

$$\begin{aligned} 4U_1^{cv}U_1^{cv} + 2\langle u_1^{cv}u_1^{cv}\rangle + \frac{\langle u_2^{cv}u_1^{cv}\rangle + \langle u_2^{top}u_1^{top}\rangle}{2} \\ + 2\langle u_1^{up}u_1^{cv}\rangle + \frac{\langle u_2^{top}u_1^{cv}\rangle + \langle u_2^{cv}u_1^{top}\rangle}{2} \\ + \frac{\langle \nu^{top}u_1^{cv}\rangle - \langle \nu^{cv}u_1^{top}\rangle}{\Delta x} + 2V\frac{V_{cv}}{A_f}\frac{\partial P}{\partial x_1} + 2T_1 = 0 \end{aligned} \quad (6.16)$$

Equation (6.16) suggests that the near-wall mean velocity is equally affected by the Reynolds shear stress at the first and second off-wall grid points. As indicated by the results presented in Figure (6.2), the occurrence of LLM seems more likely associated with the change of $\langle u^{'}v^{'}\rangle$ in the near-wall region rather than point values. Since the results presented so far show that the coupling between the modeled wall stress and the local LES solution is related to the near-wall gradient of the mean velocity, it seems reasonable to reformulate parts of the argument made by X. I. Yang, Park and Moin (2017) as follows. Defects observed in the velocity profile are due to wrongly predicting the near-wall gradient of the Reynolds shear stress. The unphysical high correlation between the modeled wall stress and the LES solution being the root source of these errors. It is important to note that this argument may explain why the near-wall velocity gradient is wrongly predicted, however, in light of the results presented in Section (6.2), it does not provide a general explanation of how LLM occurs.

An interesting feature differentiating the semi-discrete RANS and its continuous counterpart, is that the former contains two point correlations of the velocity. Since the spatial and temporal resolutions of WMLES greatly influence the small scale eddy behavior, it is difficult to estimate the magnitude of these correlations without performing numerical experiments. However, it is believed that the two-point correlations in Equation (6.16) are, in general, dissimilar to the one-point correlation usually considered.

The nonlocal nature of the semi-discrete RANS equation imply that WMLES simulations are affected not only by the grid resolution, but also by the discretization strategy. For instance, by employing a staggered grid one implicitly defined the cell to cell interaction differently than when employing co-located grids. One thus end up studying a slightly different set of transport equations, which might, to some extent, explain why LLM is code-dependent as noted by Larsson et al. (2016).

CHAPTER 7

Conclusions and Further Work

This thesis presents a thorough evaluation of *Log-Layer Mismatch* in wall modelled LES. The effects of grid topology and refinement level, eddy viscosity, and the wall modelling approach have been investigated. The effects of spatial filtering and temporal filtering of the wall model input, as well as the effect of shifting the matching location has been evaluated in the case of a turbulent channel at $Re_\tau = 5200$.

The results clearly show that that WMLES is influenced by the subgrid model, the grid topology, as well as the wall modelling approach. Comparison with the mean velocity profile obtained from DNS showed that the simulations on the truncate octahedral meshes yielded the most accurate results. However, the hexahedral grids gave, in general, better descriptions of the flow at the first off-wall grid point. The choice of cell lattice did not have a significant impact on the computational cost. Refining the mesh turned out to increase the magnitude of LLM while improving the computed velocity gradient. Simulations performed without the Vreman eddy viscosity model deteriorated the accuracy of most flow statistics. The observed reduction of LLM is therefore attributed to fortunate cancellations of errors

The results indicate that one may improve the accuracy of WMLES by departing from the traditional wall modeling approach. All strategies tested seem to reduce the strength of LLM to some extent, while the predicted Reynolds stresses were found to be less sensitive to the wall modelling approach. The remedy proposed by Kawai and Larsson (2012), to provide the wall model with LES data sampled at a distance h_{wm} above the wall, were found to be the most effective of the strategies tested. Comparing the results obtained with $h_{wm} = 0.10\delta$ and $h_{wm} = 0.20\delta$ showed that the exact modelling height is of less importance, as long as the wall model was fed data obtained above the first off-wall grid point. However, the implementation of the scheme is not trivial, especially for flows past complex bodies, discretized using unstructured grids. Of the two filtering techniques the temporal filter with $\epsilon = 0.25$ was found to be the best, further reducing the filtering weight resulted in a small rise of LLM. The spatial filter was found to have little effect on the overall solution, independent of filtering stencil or weighing scheme.

All remedies reduced the coupling between the modeled wall stress and the local LES solution. However, $\left\langle \tau_{wm} u'_{y=\Delta_c/2} \right\rangle$ showed no clear correlation with the magnitude of the near-wall Reynolds shear stress, nor LLM. Hence, the argument made by X. I. Yang, Park and Moin (2017), that LLM is due to underprediction of the Reynolds stresses, does not explain the cause of

LLM. Furthermore, employing the theoretical mean wall shear stress at the boundary gave the smallest near-wall velocity gradient while producing the largest mismatch. Hence, overprediction of the velocity gradient within the *Log-layer* does not suffice as an explanation for LLM. Closer study of the algebraic wall model indicates that by enforcing the Law of The Wall locally and instantaneously additional modeling errors are introduced. However, the modeling errors does not, in general, explain why LLM occurs. Analysis of the semi-discrete transport equations in the near-wall region showed that the computed velocity field relies on data from adjacent control volumes. As the continuous transport equations are local in time and space, the analysis implying that arguments for LLM based on the continuous equations does not provide a complete explanation of the phenomenon. Furthermore, the nonlocal nature of the semi-discrete RANS gives an explanation for why certain numerical schemes generally produce negative mismatch, while some solvers experience positive mismatch.

A logical extension of this thesis is to investigate how the wall modeling strategies tested perform in flows involving complex bodies. Another possible direction for future work is to quantify all terms in the semi-discrete RANS equations in fundamental flow problems such as zero-pressure-gradient flat-plate turbulent boundary layers or fully developed turbulent channel flow. Both to see how the non-local effects of the discretized equations affects the WMLES solution, and whether these equations can provide greater insight into the problem of LLM.

Appendices

APPENDIX A

Modeled Wall Stress

From the *Log-law* it follows that the wall shear can be computed according to Equation (A.1).

$$\tau_{wm} = \rho \frac{u_{wm}^2}{\Big(C + 0.5K^{-1} \ln \tau_{wm}\Big)^2} \tag{A.1}$$

Here, the coefficient C is defined according to Equation (A.2).

$$C = B + K^{-1} \ln \frac{h_{wm}}{\nu\sqrt{\rho}} \tag{A.2}$$

By decompose the wall shear stress into a mean and fluctuating part, $\tau_{wm} = T_{wm} + \tau_{wm}^{'}$, Equation (A.1) can be expressed as (A.3) below.

$$\Big(T_{wm} + \tau_{wm}^{'}\Big) = \rho \frac{u_{wm}^2}{\Bigg(C + 0.5K^{-1}\Big(\ln T_{wm} + \tau_{wm}^{'}/T_{wm} + \cdots\Big)\Bigg)^2} \tag{A.3}$$

Here we have expressed $\ln\left(T_{wm} + \tau_{wm}^{'}\right)$ in terms of its Taylor expansion around $\tau_{wm}^{'}) = 0$ as shown below.

$$\ln\left(T_{wm} + \tau_{wm}\right) = \ln T_{wm} + \tau_{wm}/T_{wm} - \tau_{wm}^2/2T_{wm}^2 + ...$$

Solving Equation (A.3) with respect to ρu_{wm}^2 we obtain,

$$\begin{aligned}\rho u_{wm}^2 = \Big(T_{wm}+\tau_{wm}^{'}\Big)\Bigg(C^2+CK^{-1}\Big(\ln T_{wm}+\tau_{wm}^{'}/T_{wm}-{\tau_{wm}^{'}}^2/2T_{wm}^2+\mathcal{O}({\tau_{wm}^{'}}^3)\Big)\Bigg) \\ + 0.25K^{-2}\Big(T_{wm}+\tau_{wm}^{'}\Big)\Big(\ln {T_{wm}}^2 + 2\tau_{wm}^{'}\ln T_{wm}/T_{wm} + {\tau_{wm}^{'}}^2/T_{wm}^2 \\ - \ln T_{wm}{\tau_{wm}^{'}}^2/T_{wm}^2 + \mathcal{O}({\tau_{wm}^{'}}^3)\Big)\end{aligned}$$

which imply that,

$$
\begin{aligned}
\rho u_{wm}^2 =& T_{wm}\Big(C^2 + CK^{-1}\Big(\ln T_{wm} + \tau_{wm}^{'}/T_{wm} - {\tau_{wm}^{'}}^2/2T_{wm}^2 + \mathcal{O}({\tau_{wm}^{'}}^3)\Big)\Big) \\
&+ \tau_{wm}^{'}\Big(C^2 + CK^{-1}\Big(\ln T_{wm} + \tau_{wm}^{'}/T_{wm} - {\tau_{wm}^{'}}^2/2T_{wm}^2 + \mathcal{O}({\tau_{wm}^{'}}^3)\Big)\Big) \\
&+ 0.25K^{-2}T_{wm}\Big(\ln {T_{wm}}^2 + 2\tau_{wm}^{'}\ln T_{wm}/T_{wm} + {\tau_{wm}^{'}}^2/T_{wm}^2 - \ln T_{wm}{\tau_{wm}^{'}}^2/2T_{wm}^2 + \mathcal{O}({\tau_{wm}^{'}}^3)\Big) \\
&+ 0.25K^{-2}\tau_{wm}^{'}\Big(\ln {T_{wm}}^2 + 2\tau_{wm}^{'}\ln T_{wm}/T_{wm} + {\tau_{wm}^{'}}^2/T_{wm}^2 - \ln T_{wm}{\tau_{wm}^{'}}^2/2T_{wm}^2 + \mathcal{O}({\tau_{wm}^{'}}^3)\Big).
\end{aligned}
$$

Averaging of the above equation yields,

$$
\begin{aligned}
\rho\Big\langle u_{wm}^2\Big\rangle =& T_{wm}\Big(C^2 + CK^{-1}\ln T_{wm}\Big) - CK^{-1}\Big\langle\tau_{wm}^{'}\tau_{wm}^{'}\Big\rangle/2T_{wm} + \mathcal{O}({\tau_{wm}^{'}}^3) \\
&+ CK^{-1}\Big\langle\tau_{wm}^{'}\tau_{wm}^{'}\Big\rangle/T_{wm} + \mathcal{O}({\tau_{wm}^{'}}^3) \\
&+ 0.25K^{-2}\Big(T_{wm}\ln {T_{wm}}^2 + \Big\langle\tau_{wm}^{'}\tau_{wm}^{'}\Big\rangle/T_{wm} - \Big\langle\tau_{wm}^{'}\tau_{wm}^{'}\Big\rangle\ln T_{wm}/2T_{wm} + \mathcal{O}({\tau_{wm}^{'}}^3)\Big) \\
&+ 0.25K^{-2}2\Big\langle\tau_{wm}^{'}\tau_{wm}^{'}\Big\rangle\ln T_{wm}/T_{wm} + \mathcal{O}({\tau_{wm}^{'}}^3)
\end{aligned}
$$

which again imply,

$$
\begin{aligned}
\rho\Big\langle u_{wm}^2\Big\rangle =& T_{wm}\Big(C^2 + CK^{-1}\ln T_{wm}\Big) + CK^{-1}\Big\langle\tau_{wm}^{'}\tau_{wm}^{'}\Big\rangle/2T_{wm} \\
&+ 0.25K^{-2}\Big(T_{wm}\ln {T_{wm}}^2 + \Big\langle\tau_{wm}^{'}\tau_{wm}^{'}\Big\rangle/T_{wm}\Big(1 - \frac{3}{2}\ln T_{wm}\Big)\Big) + \mathcal{O}({\tau_{wm}^{'}}^3).
\end{aligned}
$$

After some simple manipulation it follows that,

$$
\begin{aligned}
\rho\Big\langle u_{wm}^2\Big\rangle =& T_{wm}\Big(C + 0.5K^{-1}\ln T_{wm}\Big)^2 \\
&+ K^{-1}\Big\langle\tau_{wm}^{'}\tau_{wm}^{'}\Big\rangle/T_{wm}\Big(C/2 + 0.25K^{-1}\Big(1 - \frac{3}{2}\ln T_{wm}\Big)\Big) + \mathcal{O}({\tau_{wm}^{'}}^3).
\end{aligned}
$$

Solving for T_{wm} we obtain Equation (A.4).

$$
\begin{aligned}
T_{wm} =& \rho\frac{\Big\langle u_{wm}^2\Big\rangle}{\Big(C + 0.5K^{-1}\ln T_{wm}\Big)^2} \\
&+ \Big\langle\tau_{wm}^{'}\tau_{wm}^{'}\Big\rangle\frac{\Big(C/2 + 0.25K^{-1}\Big(1 - \frac{3}{2}\ln T_{wm}\Big)\Big)}{KT_{wm}\Big(C + 0.5K^{-1}\ln T_{wm}\Big)^2} + \mathcal{O}({\tau_{wm}^{'}}^3)
\end{aligned}
\tag{A.4}
$$

Decompose the wall model velocity into a mean and fluctuating part, $u_{wm} = \Big\langle u_{wm}\Big\rangle + u_{wm}^{\prime}$, Equation (A.4) can be written as Equation (A.5).

$$
\begin{aligned}
T_{wm} =& \rho \frac{\left\langle u_{wm} \right\rangle^2}{\left(C + 0.5K^{-1} \ln T_{wm} \right)^2} + \rho \frac{\left\langle u'_{wm} u'_{wm} \right\rangle}{\left(C + 0.5K^{-1} \ln T_{wm} \right)^2} \\
&+ \left\langle \tau'_{wm} \tau'_{wm} \right\rangle \frac{\left(C/2 + 0.25K^{-1} \left(1 - \frac{3}{2} \ln T_{wm} \right) \right)}{K T_{wm} \left(C + 0.5K^{-1} \ln T_{wm} \right)^2} + \mathcal{O}(\tau'^3_{wm}).
\end{aligned}
\tag{A.5}
$$

Since the theoretical mean shear stress $\left\langle \tau_{wm}^{Log-Law} \right\rangle$ can be approximated as,

$$
\left\langle \tau_{wm}^{Log-Law} \right\rangle = \rho \frac{\left\langle u_{wm} \right\rangle^2}{\left(C + 0.5K^{-1} \ln T_{wm} \right)^2} \tag{A.6}
$$

it follows from Equation (A.5) that wall model error is given by Equation (A.7).

$$
\begin{aligned}
T_{wm} - \left\langle \tau_{wm}^{Log-Law} \right\rangle =& \rho \frac{\left\langle u'_{wm} u'_{wm} \right\rangle}{\left(C + 0.5K^{-1} \ln T_{wm} \right)^2} \\
&+ \left\langle \tau'_{wm} \tau'_{wm} \right\rangle \frac{\left(C/2 + 0.25K^{-1} \left(1 - \frac{3}{2} \ln T_{wm} \right) \right)}{K T_{wm} \left(C + 0.5K^{-1} \ln T_{wm} \right)^2} + \mathcal{O}(\tau'^3_{wm})
\end{aligned}
\tag{A.7}
$$

APPENDIX B

Derivation of the Semi-Discrete Reynolds Average Navier-Stokes

Assuming the density ρ to be constant, the governing semi-discrete equation for the velocity is of the form

$$V_{cv}\frac{\partial \tilde{u}_i}{\partial t}+\sum_{IF}\tilde{u}^f\frac{\tilde{u}_i^{cv}+\tilde{u}_i^{nbr}}{2}+V_{cv}\frac{\partial \tilde{p}}{\partial x_i}+\sum_{BF}\tilde{\tau}_i A_{bf}+\sum_{IF}\tilde{\nu}^f\frac{\tilde{u}_i^{cv}-\tilde{u}_i^{nbr}}{2}=0 \quad \text{(B.1)}$$

Here, $\tilde{u}, \tilde{p}$ and $\tilde{\tau}$ denote the instantaneous value of the discrete velocity field, pressure and wall shear, respectively. Further, IF, BF and nbr denote the internal faces, boundary faces with area A_{bf}, and the velocity in the grid cells adjacent to the control volume cv, respectively. The volume of the grid cell is denoted by V_{cv}, and $\tilde{\nu}^f$, defined in Equation (B.2), represent the kinematic viscosity at an internal face with area A_f and is a function of time and space.

$$\tilde{\nu}^f=\frac{A_f}{\Delta x}\left(\nu+\tilde{\nu}_e^f\right) \quad \text{(B.2)}$$

In the above equation, Δx denotes the the cell size and $\tilde{\nu}_e^f$ is the face eddy viscosity. The flux velocity $\tilde{u}^f$, is defined on the faces of the control volume, and satisfies the divergence free constraint given in Equation (B.3).

$$\sum_{IF}\tilde{u}^f=0. \quad \text{(B.3)}$$

Even though it is refereed to as a velocity, $\tilde{u}^f$ is in reality a mass flux, hence $\tilde{u}^f \propto \tilde{u}^{cv}A_f$. Ignoring the pressure projection step, assuming it is used to enforce Equation (B.3), and decomposing the fluctuating fields according to Equation (B.4),

$$\begin{aligned}\tilde{u}_i &= U_i+u_i\\ \tilde{u}^f &= U^f+u^f\\ \tilde{p} &= P+p\\ \tilde{\tau}_i &= T_i+\tau_i\\ \tilde{\nu}^f &= N^f+\nu^f\end{aligned} \quad \text{(B.4)}$$

Equation (B.1) can be expressed as

$$V_{cv}\frac{\partial}{\partial t}\left(U_i^{cv}+u_i^{cv}\right)+\sum_{IF}\left(U^f+u^f\right)\frac{U_i^{cv}+u_i^{cv}+U_i^{nbr}+u_i^{nbr}}{2} + V_{cv}\frac{\partial}{\partial x_i}\left(P+p\right)+\sum_{BF}\left(T_i+\tau_i\right)A_{bf} + \sum_{IF}\left(N^f+\nu^f\right)\frac{U_i^{cv}+u_i^{cv}-U_i^{nbr}-u_i^{nbr}}{2}=0. \quad \text{(B.5)}$$

Apply the averaging operator $\langle . \rangle$ to (B.5), noting that $\langle \Phi_i \rangle = \Phi_i$, $\langle \phi_i \rangle = 0$ and $\langle \Phi_i \phi_i \rangle = \langle \Phi_i \rangle \langle \phi_i \rangle = 0$, we obtain the semi-discrete Reynolds Averaged Navier-Stokes equation (B.6).

$$V_{cv}\frac{\partial U_i^{cv}}{\partial t}+\sum_{IF}\frac{U^f U_i^{cv}+U^f U_i^{nbr}}{2}+\sum_{IF}\frac{\langle u^f u_i^{cv}\rangle+\langle u^f u_i^{nbr}\rangle}{2} + \sum_{IF}N^f\frac{U_i^{cv}-U_i^{nbr}}{2}+\sum_{IF}\frac{\langle \nu^f u_i^{cv}\rangle-\langle \nu^f u_i^{nbr}\rangle}{2}+V_{cv}\frac{\partial P}{\partial x_i}+\sum_{BF}T_i A_{bf}=0 \quad \text{(B.6)}$$

Next, we considering the semi-discrete equation presented above for a full-developed channel flow at the first off-wall grid point on a structured Cartesian grid. In this case the mean velocity field reduce to $U=(U(y),0,0)$. Furthermore, the flow is homogeneous in the streamwise and spanwise directions, which implies that the stresses $\langle u_1 u_3 \rangle$ and $\langle u_2 u_3 \rangle$ are exactly zero. Finally, noting that each control volume only have two faces with a non-zero mean flux velocity U^f, denoted as U^f_{up} and U^f_{down}, the semi-discrete RANS equation can be expressed according to Equation (B.7).

$$V_{cv}\frac{\partial U_i^{cv}}{\partial t}+U^f_{up}\frac{U_i^{cv}+U_i^{up}}{2}+U^f_{down}\frac{U_i^{cv}+U_i^{down}}{2}+\sum_{IF}N^f\frac{U_i^{cv}-U_i^{nbr}}{2} + \sum_{IF}\frac{\langle u^f u_i^{cv}\rangle+\langle u^f u_i^{nbr}\rangle}{2}+\sum_{IF}\frac{\langle \nu^f u_i^{cv}\rangle-\langle \nu^f u_i^{nbr}\rangle}{2}+V_{cv}\frac{\partial P}{\partial x_i}+T_i A_f=0 \quad \text{(B.7)}$$

The superscripts $(.^{up})$ and $(.^{down})$ denotes the velocities in the cells sharing a face with a non-zero mean flux velocity. Further, the flux velocity, $\tilde{u}^f$, can be expressed according to Equation (B.8).

$$
\begin{aligned}
\tilde{u}^f_{up} &= \frac{1}{2}\Big(\tilde{u}^{cv}_1 + \tilde{u}^{up}_1\Big)A_f \\
\tilde{u}^f_{down} &= \frac{1}{2}\Big(\tilde{u}^{cv}_1 + \tilde{u}^{down}_1\Big)A_f \\
\tilde{u}^f_{left} &= \frac{1}{2}\Big(\tilde{u}^{cv}_3 + \tilde{u}^{left}_3\Big)A_f \\
\tilde{u}^f_{right} &= \frac{1}{2}\Big(\tilde{u}^{cv}_3 + \tilde{u}^{right}_3\Big)A_f \\
\tilde{u}^f_{top} &= \frac{1}{2}\Big(\tilde{u}^{cv}_2 + \tilde{u}^{top}_2\Big)A_f
\end{aligned}
\tag{B.8}
$$

Here the superscripts $(.^{left})$, $(.^{right})$, and $(.^{top})$ denotes the velocity in the cells sharing the face for which the velocity fluxes $(\tilde{.})^f_{left}$, $(\tilde{.})^f_{right}$ and $(\tilde{.})^f_{top}$ are defined. Similarly, the face kinematic viscosity at the internal faces are defined in Equation (B.9).

$$
\begin{aligned}
\tilde{\nu}^f_{up} &= \Big(\tilde{\nu}^{cv} + \tilde{\nu}^{up}\Big)\frac{A_f}{\Delta x} \\
\tilde{\nu}^f_{down} &= \Big(\tilde{\nu}^{cv} + \tilde{\nu}^{down}\Big)\frac{A_f}{\Delta x} \\
\tilde{\nu}^f_{left} &= \Big(\tilde{\nu}^{cv} + \tilde{\nu}^{left}\Big)\frac{A_f}{\Delta x} \\
\tilde{\nu}^f_{right} &= \Big(\tilde{\nu}^{cv} + \tilde{\nu}^{right}\Big)\frac{A_f}{\Delta x} \\
\tilde{\nu}^f_{top} &= \Big(\tilde{\nu}^{cv} + \tilde{\nu}^{top}\Big)\frac{A_f}{\Delta x}
\end{aligned}
\tag{B.9}
$$

Here the control volume kinematic viscosity is defined as $\tilde{\nu}^{cv} = \nu + \tilde{\nu}^{cv}_e$. Introducing the the decomposing of the flux velocity and kinematic viscosity presented in Equation (B.8) and (B.9) yields the transport equation below.

$$
\begin{aligned}
V_{cv}\frac{\partial U^{cv}_i}{\partial t} &+ \Big(U^{cv} + U^{up}\Big)A_f\frac{U^{cv}_i + U^{up}_i}{4} + \Big(U^{cv} + U^{down}\Big)A_f\frac{U^{cv}_i + U^{down}_i}{4} \\
&+ \Big(N^{cv} + N^{up}\Big)\frac{U^{cv}_i - U^{up}_i}{2} + \Big(N^{cv} + N^{down}\Big)\frac{U^{cv}_i - U^{down}_i}{2} \\
&+ \Big(N^{cv} + N^{left}\Big)\frac{U^{cv}_i - U^{left}_i}{2} + \Big(N^{cv} + N^{right}\Big)\frac{U^{cv}_i - U^{right}_i}{2} \\
&+ \Big(N^{cv} + N^{top}\Big)\frac{U^{cv}_i - U^{top}_i}{2} \\
&+ \frac{\big\langle \nu^{cv}u^{cv}_i\big\rangle + \big\langle \nu^{up}u^{cv}_i\big\rangle - \big\langle \nu^{cv}u^{up}_i\big\rangle - \big\langle \nu^{up}u^{up}_i\big\rangle}{2}\frac{A_f}{\Delta x} \\
&+ \frac{\big\langle \nu^{cv}u^{cv}_i\big\rangle + \big\langle \nu^{down}u^{cv}_i\big\rangle - \big\langle \nu^{cv}u^{down}_i\big\rangle - \big\langle \nu^{down}u^{down}_i\big\rangle}{2}\frac{A_f}{\Delta x} \\
&+ \frac{\big\langle \nu^{cv}u^{cv}_i\big\rangle + \big\langle \nu^{left}u^{cv}_i\big\rangle - \big\langle \nu^{cv}u^{left}_i\big\rangle - \big\langle \nu^{left}u^{left}_i\big\rangle}{2}\frac{A_f}{\Delta x} \\
&+ \frac{\big\langle \nu^{cv}u^{cv}_i\big\rangle + \big\langle \nu^{right}u^{cv}_i\big\rangle - \big\langle \nu^{cv}u^{right}_i\big\rangle - \big\langle \nu^{right}u^{right}_i\big\rangle}{2}\frac{A_f}{\Delta x}
\end{aligned}
$$

$$
\begin{aligned}
&+\frac{\langle \nu^{cv}u_i^{cv}\rangle+\langle \nu^{top}u_i^{cv}\rangle-\langle \nu^{cv}u_i^{top}\rangle-\langle \nu^{top}u_i^{top}\rangle}{2}\frac{A_f}{\Delta x}\\
&+\frac{\langle u_1^{cv}u_i^{cv}\rangle+\langle u_1^{up}u_i^{cv}\rangle+\langle u_1^{cv}u_i^{up}\rangle+\langle u_1^{up}u_i^{up}\rangle}{4}A_f\\
&+\frac{\langle u_1^{cv}u_i^{cv}\rangle+\langle u_1^{down}u_i^{cv}\rangle+\langle u_1^{cv}u_i^{down}\rangle+\langle u_1^{down}u_i^{down}\rangle}{4}A_f\\
&+\frac{\langle u_3^{cv}u_i^{cv}\rangle+\langle u_3^{left}u_i^{cv}\rangle+\langle u_3^{cv}u_i^{left}\rangle+\langle u_3^{left}u_i^{left}\rangle}{4}A_f\\
&+\frac{\langle u_3^{cv}u_i^{cv}\rangle+\langle u_3^{right}u_i^{cv}\rangle+\langle u_3^{cv}u_i^{right}\rangle+\langle u_3^{right}u_i^{right}\rangle}{4}A_f\\
&+\frac{\langle u_2^{cv}u_i^{cv}\rangle+\langle u_2^{top}u_i^{cv}\rangle+\langle u_2^{cv}u_i^{top}\rangle+\langle u_2^{top}u_i^{top}\rangle}{4}A_f+V_{cv}\frac{\partial P}{\partial x_i}+T_iA_f=0
\end{aligned}
$$

Noting that for a fully developed channel flow temporal derivatives vanishes and $U^{cv}=U^{nbr}$. Furthermore, the turbulence is homogeneous in the wall parallel plane, assuming the two point correlations $\langle u_1^{cv}u_3^{nbr}\rangle=\langle u_2^{cv}u_3^{nbr}\rangle=0$, it follows from the above equation that the semi-discrete RANS equation for the streamwise direction becomes,

$$
\begin{aligned}
4U^{cv}U^{cv}&+2\langle u_1^{cv}u_1^{cv}\rangle+\frac{\langle u_2^{cv}u_1^{cv}\rangle+\langle u_2^{top}u_1^{top}\rangle}{2}\\
&+2\langle u_1^{up}u_1^{cv}\rangle+\frac{\langle u_2^{top}u_1^{cv}\rangle+\langle u_2^{cv}u_1^{top}\rangle}{2}\\
&+\frac{\langle \nu^{top}u_1^{cv}\rangle-\langle \nu^{cv}u_1^{top}\rangle}{\Delta x}+2\frac{V_{cv}}{A_f}\frac{\partial P}{\partial x_1}+2T_1=0.
\end{aligned}
\tag{B.10}
$$

The wall-normal transport equation becomes,

$$
\begin{aligned}
&\langle u_1^{cv}u_2^{cv}\rangle+\frac{\langle u_1^{up}u_2^{cv}\rangle+\langle u_1^{cv}u_2^{up}\rangle}{2}+\frac{\langle u_2^{cv}u_2^{cv}\rangle+\langle u_2^{top}u_2^{top}\rangle}{4}\\
&+\frac{\langle u_2^{top}u_2^{cv}\rangle+\langle u_2^{cv}u_2^{top}\rangle}{4}+\frac{\langle \nu^{top}u_2^{cv}\rangle-\langle \nu^{cv}u_2^{top}\rangle}{2\Delta x}+\frac{V_{cv}}{A_f}\frac{\partial P}{\partial x_1}=0,
\end{aligned}
\tag{B.11}
$$

while the spanwise transport equation reduce to Equation (B.12) below,

$$
\langle u_3^{cv}u_3^{cv}\rangle+\frac{\langle u_3^{cv}u_3^{left}\rangle+\langle u_3^{cv}u_3^{right}\rangle}{2}+\frac{\langle \nu^{top}u_2^{cv}\rangle-\langle \nu^{cv}u_2^{top}\rangle}{2\Delta x}+T_3=0. \tag{B.12}
$$

APPENDIX C

Derivation of the Semi-Discrete Reynolds Stress Transport Equation

From Appendix (B) it follows that the semi-discrete Reynolds Averaged Navier-Stokes equation can be written as Equation (C.1)

$$V_{cv}\frac{\partial U_i^{cv}}{\partial t}+\sum_{IF}\frac{U^f U_i^{cv}+U^f U_i^{nbr}}{2}+\sum_{IF}\frac{\langle u^f u_i^{cv}\rangle+\langle u^f u_i^{nbr}\rangle}{2} + \mathcal{V}_i+V_{cv}\frac{\partial P}{\partial x_i}+\sum_{BF}T_i A_{bf}=0 \quad \text{(C.1)}$$

Here, $\mathcal{V}_i$ denotes the viscous terms. Subtract the above equation from the semi-discrete transport equation (Eq. B.1) we get the transport equation for the fluctuating velocity field,

$$\begin{aligned}V_{cv}\frac{\partial}{\partial t}\left(U_i^{cv}+u_i^{cv}\right)+\sum_{IF}\left(U^f+u^f\right)\frac{U_i^{cv}+u_i^{cv}+U_i^{nbr}+u_i^{nbr}}{2}\\ +V_{cv}\frac{\partial}{\partial x_i}\left(P+p\right)+\sum_{BF}\left(T_i+\tau_i\right)_i A_f-\Bigg(V_{cv}\frac{\partial U^{cv}}{\partial t}+V_{cv}\frac{\partial P}{\partial x_i}+\sum_{BF}T_i A_f\\ +\sum_{IF}\frac{U^f U_i^{cv}+U^f U_i^{nbr}}{2}+\sum_{IF}\frac{\langle u^f u_i^{cv}\rangle+\langle u^f u_i^{nbr}\rangle}{2}\Bigg)+\mathcal{V}_i=0, \quad \text{(C.2)}\end{aligned}$$

which implies

$$\begin{aligned}V_{cv}\frac{\partial u_i^{cv}}{\partial t}=-\sum_{IF}U^f\frac{u_i^{cv}+u_i^{nbr}}{2}-\sum_{IF}u^f\frac{U_i^{cv}+u_i^{cv}+U_i^{nbr}+u_i^{nbr}}{2}\\ -V_{cv}\frac{\partial p}{\partial x_i}-\sum_{BF}\tau_i A_f+\sum_{IF}\frac{\langle u^f u_i^{cv}\rangle+\langle u^f u_i^{nbr}\rangle}{2}-\mathcal{V}_i. \quad \text{(C.3)}\end{aligned}$$

The discretized transport equation for the Reynolds stresses, R_{ij}, can be derived using the following trivial manipulation,

$$
\begin{aligned}
V_{cv}\frac{\partial u_i^{cv}u_j^{cv}}{\partial t} &= V_{cv}\big(u_i^{cv}\frac{\partial u_j^{cv}}{\partial t}+u_j^{cv}\frac{\partial u_i^{cv}}{\partial t}\big)\\
&= u_i^{cv}\big(V_{cv}\frac{\partial u_j^{cv}}{\partial t}\big)+u_j^{cv}\big(V_{cv}\frac{\partial u_i^{cv}}{\partial t}\big).
\end{aligned}
\tag{C.4}
$$

Inserting Equation (C.3) into the above relation yields the semi-discrete equation of $u_i^{cv}u_j^{cv}$ shown below.

$$
\begin{aligned}
V_{cv}\frac{\partial u_i^{cv}u_j^{cv}}{\partial t} = &-u_j^{cv}\Bigg(\sum_{IF}U^f\frac{u_i^{cv}+u_i^{nbr}}{2}+\sum_{IF}u^f\frac{U_i^{cv}+u_i^{cv}+U_i^{nbr}+u_i^{nbr}}{2}\\
&+V_{cv}\frac{\partial p}{\partial x_i}+\sum_{BF}\tau_i A_f-\sum_{IF}\frac{\langle u^f u_i^{cv}\rangle+\langle u^f u_i^{nbr}\rangle}{2}\Bigg)\\
&-u_i^{cv}\Bigg(\sum_{IF}U^f\frac{u_j^{cv}+u_j^{nbr}}{2}+\sum_{IF}u^f\frac{U_j^{cv}+u_j^{cv}+U_j^{nbr}+u_j^{nbr}}{2}\\
&+V_{cv}\frac{\partial p}{\partial x_j}+\sum_{BF}\tau_j A_f-\sum_{IF}\frac{\langle u^f u_j^{cv}\rangle+\langle u^f u_j^{nbr}\rangle}{2}\Bigg)-\tilde{\mathcal{V}}_{i,j}
\end{aligned}
\tag{C.5}
$$

After some simple algebraic manipulation, Equation (C.5) becomes Equation (C.6).

$$
\begin{aligned}
V_{cv}\frac{\partial u_i^{cv}u_j^{cv}}{\partial t} = &-u_j^{cv}u_i^{cv}\sum_{IF}U^f-\sum_{IF}U^f\frac{u_j^{cv}u_i^{nbr}+u_i^{cv}u_j^{nbr}}{2}\\
&-u_j^{cv}u_i^{cv}\sum_{IF}u^f-\sum_{IF}u^f\frac{u_j^{cv}u_i^{nbr}+u_i^{cv}u_j^{nbr}}{2}\\
&-\Big(u_j^{cv}U_i^{cv}+u_i^{cv}U_j^{cv}\Big)\sum_{IF}u^f-\sum_{IF}u^f\frac{u_j^{cv}U_i^{nbr}+u_i^{cv}U_j^{nbr}}{2}\\
&-V_{cv}\big(u_j^{cv}\frac{\partial p}{\partial x_i}+u_i^{cv}\frac{\partial p}{\partial x_j}\big)\\
&-\sum_{BF}\big(u_j^{cv}\tau_i+u_i^{cv}\tau_j\big)A_f\\
&+\sum_{IF}\frac{u_j^{cv}\langle u^f u_i^{cv}\rangle+u_j^{cv}\langle u^f u_i^{nbr}\rangle+u_i^{cv}\langle u^f u_j^{cv}\rangle+u_i^{cv}\langle u^f u_j^{nbr}\rangle}{2}\\
&-\tilde{\mathcal{V}}_{i,j}
\end{aligned}
\tag{C.6}
$$

Enforcing the divergence free constraint for U^f and u^f, Equation (C.6) reduce to Equation (C.7) below.

$$
\begin{aligned}
V_{cv}\frac{\partial u_i^{cv}u_j^{cv}}{\partial t} =& -\sum_{IF} U^f \frac{u_j^{cv}u_i^{nbr}+u_i^{cv}u_j^{nbr}}{2} - \sum_{IF} u^f \frac{u_j^{cv}u_i^{nbr}+u_i^{cv}u_j^{nbr}}{2} \\
&- \sum_{IF} u^f \frac{u_j^{cv}U_i^{nbr}+u_i^{cv}U_j^{nbr}}{2} - V_{cv}\big(u_j^{cv}\frac{\partial p}{\partial x_i}+u_i^{cv}\frac{\partial p}{\partial x_j}\big) \\
&- \sum_{BF}\big(u_j^{cv}\tau_i+u_i^{cv}\tau_j\big)A_f \\
&+ \sum_{IF}\frac{u_j^{cv}\langle u^f u_i^{cv}\rangle + u_j^{cv}\langle u^f u_i^{nbr}\rangle + u_i^{cv}\langle u^f u_j^{cv}\rangle + u_i^{cv}\langle u^f u_j^{nbr}\rangle}{2} \\
&- \tilde{\mathcal{V}}_{i,j}
\end{aligned}
\tag{C.7}
$$

Taking the ensemble average of Equation (C.6) yields the semi-discrete transport equation of the Reynolds stresses, $R_{ij} = \langle u_i^{cv}u_j^{cv}\rangle$,

$$
\begin{aligned}
V_{cv}\frac{\partial R_{ij}}{\partial t} =& -\frac{1}{2}\sum_{IF} U^f\Big(\langle u_j^{cv}u_i^{nbr}\rangle + \langle u_i^{cv}u_j^{nbr}\rangle\Big) \\
&- \frac{1}{2}\sum_{IF}\Big(\langle u^f u_j^{cv}u_i^{nbr}\rangle + \langle u^f u_i^{cv}u_j^{nbr}\rangle\Big) \\
&- \frac{1}{2}\sum_{IF}\Big(\langle u^f u_j^{cv}\rangle U_i^{nbr} + \langle u^f u_i^{cv}\rangle U_j^{nbr}\Big) \\
&- V_{cv}\langle u_j^{cv}\frac{\partial p}{\partial x_i} + u_i^{cv}\frac{\partial p}{\partial x_j}\rangle \\
&- \sum_{BF}\langle u_j^{cv}\tau_i + u_i^{cv}\tau_j\rangle A_f \\
&+ \frac{1}{2}\sum_{IF}\Big(\langle u_j^{cv}\rangle\langle u^f u_i^{cv}\rangle + \langle u_j^{cv}\rangle\langle u^f u_i^{nbr}\rangle + \langle u_i^{cv}\rangle\langle u^f u_j^{cv}\rangle + \langle u_i^{cv}\rangle\langle u^f u_j^{nbr}\rangle\Big) \\
&- \tilde{\mathcal{V}}_{i,j}
\end{aligned}
\tag{C.8}
$$

which imply

$$
\begin{aligned}
V_{cv}\frac{\partial R_{ij}}{\partial t} = &-\sum_{IF}\left(U^f\frac{\langle u_i^{cv}u_j^{nbr}\rangle + \langle u_j^{cv}u_i^{nbr}\rangle}{2}\right)\\
&-\sum_{IF}\left(\frac{\langle u^f u_j^{cv}u_i^{nbr}\rangle + \langle u^f u_i^{cv}u_j^{nbr}\rangle}{2}\right)\\
&-\sum_{IF}\left(\frac{\langle u^f u_j^{cv}\rangle U_i^{nbr} + \langle u^f u_i^{cv}\rangle U_j^{nbr}}{2}\right)\\
&-V_{cv}\left(\left\langle u_j^{cv}\frac{\partial p}{\partial x_i}\right\rangle + \left\langle u_i^{cv}\frac{\partial p}{\partial x_j}\right\rangle\right)\\
&-\sum_{BF}\langle u_j^{cv}\tau_i + u_i^{cv}\tau_j\rangle A_f\\
&-\tilde{\mathcal{V}}_{i,j}.
\end{aligned}
\tag{C.9}
$$

The above equation can be expressed as,

$$
V_{cv}\frac{\partial R_{ij}}{\partial t} + \tilde{\mathcal{A}}_{ij} = -\tilde{\mathcal{P}}^s_{ij} - \tilde{\mathcal{P}}^\tau_{ij} - \tilde{\mathcal{R}}_{ij} - \tilde{\mathcal{T}}_{ij} - \tilde{\mathcal{V}}_{ij} \tag{C.10}
$$

where $\tilde{\mathcal{A}}_{ij}, \tilde{\mathcal{P}}^s_{ij}, \tilde{\mathcal{R}}_{ij}$ and $\tilde{\mathcal{T}}_{ij}$ denotes the numerical advection, production, turbulent transport and pressure redistribution of the semi-discretized transport equation and are presented below. $\tilde{\mathcal{V}}_{ij}$ represent the viscous terms, that is, the viscous diffusion rate and the viscous dissipation rate. $\tilde{\mathcal{P}}^\tau_{ij}$ acts like a production terms for the turbulent energy and is caused by correlations between the wall shear and the of wall velocity. The five terms are summarized below.

$$
\tilde{\mathcal{A}}_{ij} = \sum_{IF} U^f\frac{\langle u_j^{cv}u_i^{nbr}\rangle + \langle u_i^{cv}u_j^{nbr}\rangle}{2} \qquad \text{Advection}
$$

$$
\tilde{\mathcal{P}}^s_{ij} = \sum_{IF}\left(\langle u^f u_j^{cv}\rangle\frac{U_i^{nbr}}{2} + \langle u^f u_i^{cv}\rangle\frac{U_j^{nbr}}{2}\right) \qquad \text{Production}
$$

$$
\tilde{\mathcal{P}}^\tau_{ij} = \sum_{BF}\langle u_j^{cv}\tau_i + u_i^{cv}\tau_j\rangle A_f \qquad \text{Production due to wall shear}
$$

$$
\tilde{\mathcal{R}}_{ij} = V_{cv}\left(\left\langle u_j^{cv}\frac{\partial p}{\partial x_i}\right\rangle + \left\langle u_i^{cv}\frac{\partial p}{\partial x_j}\right\rangle\right) \qquad \text{Velocity-pressure gradient tensor}
$$

$$
\tilde{\mathcal{T}}_{ij} = \sum_{IF}\frac{\langle u^f u_j^{cv}u_i^{nbr}\rangle + \langle u^f u_i^{cv}u_j^{nbr}\rangle}{2} \qquad \text{Turbulent transport rate}
$$

Bibliography

Ahlfors, L. V. (1966). *Complex analysis: An introduction to the theory of analytic functions of one complex variable*. eng. New York.

Ambo, K. et al. (2020). 'Aerodynamic force prediction of the laminar to turbulent flow transition around the front bumper of the vehicle using Dynamic-slip wall model LES'. In: *AIAA Scitech 2020 Forum*.

Bazilevs, Y. and Hughes, T. (2007). 'Weak imposition of Dirichlet boundary conditions in fluid mechanics'. eng. In: *Computers fluids* vol. 36, no. 1, pp. 12–26.

Bose, S. T. and Park, G. I. (2018). 'Wall-modeled large-eddy simulation for complex turbulent flows'. In: *Annual review of fluid mechanics* vol. 50, pp. 535–561.

Bose, S. and Moin, P. (2014). 'A dynamic slip boundary condition for wall-modeled large-eddy simulation'. In: *Physics of Fluids* vol. 26, no. 1, p. 015104.

Bou-Zeid, E., Meneveau, C. and Parlange, M. B. (2004). 'Large-eddy simulation of neutral atmospheric boundary layer flow over heterogeneous surfaces: Blending height and effective surface roughness'. eng. In: *Water resources research* vol. 40, no. 2, W02505–n/a.

Brasseur, J. G. and Wei, T. (2010). 'Designing large-eddy simulation of the turbulent boundary layer to capture law-of-the-wall scaling'. eng. In: *Physics of Fluids* vol. 22, no. 2, pp. 1–21.

Brès, G. A. et al. (2018). 'Large-eddy simulations of co-annular turbulent jet using a Voronoi-based mesh generation framework'. In: *2018 AIAA/CEAS Aeroacoustics Conference*.

Çengel, Y. A. and Cimbala, J. M. (2014). *Fluid mechanics : fundamentals and applications*. eng. 3rd ed. in SI units. Boston: McGraw-Hill.

Choi, H. and Moin, P. (2012). 'Grid-point requirements for large eddy simulation: Chapman's estimates revisited'. eng. In: *Physics of Fluids* vol. 24, no. 1, pp. 011702–011702-5.

Chung, D. and Pullin, D. I. (2009). 'Large-eddy simulation and wall modelling of turbulent channel flow'. eng. In: *Journal of Fluid Mechanics* vol. 631, pp. 281–309.

Coles, D. (1956). 'The law of the wake in the turbulent boundary layer'. eng. In: *Journal of Fluid Mechanics* vol. 1, no. 2, pp. 191–226.

De Santis, A. et al. (2020). 'Assessment of the impact of subgrid-scale stress models and mesh resolution on the LES of a partially-premixed swirling flame'. eng. In: *Fuel (Guildford)* vol. 281, p. 118620.

Deardorff, J. W. (1970). 'A numerical study of three-dimensional turbulent channel flow at large Reynolds numbers'. eng. In: *Journal of Fluid Mechanics* vol. 41, no. 2, pp. 453–480.

Falkner, V. and Skan, S. (1931). 'Some approximate solutions of the boundary layer equations.' eng. In: *Philos. Mag.* vol. 12, no. 7, pp. 865–896.

Fureby, C. et al. (1997). 'A comparative study of subgrid scale models in homogeneous isotropic turbulence'. eng. In: *Physics of Fluids* vol. 9, no. 5, pp. 1416–1429.

Germano, M. et al. (1991). 'A dynamic subgrid-scale eddy viscosity model'. eng. In: *Physics of Fluids. A, Fluid dynamics* vol. 3, no. 7, pp. 1760–1765.

Gropp, W. (1999). *Using MPI : portable parallel programming with the message-passing interface*. eng.

Hager, G. and Wellein, G. (2011). *Introduction to High Performance Computing for Scientists and Engineers*. eng. Chapman & Hall/CRC computational science series. Baton Rouge: CRC Press.

Imtiaz, H. and Akhtar, I. (2019). 'Nonlinear closure modeling in reduced order models for turbulent flows: a dynamical system approach'. eng. In: *Nonlinear dynamics* vol. 99, no. 1, pp. 479–494.

Jackson, D. and Launder, B. (2007). 'Osborne Reynolds and the publication of his papers on turbulent flow'. eng. In: *Annual Review of Fluid Mechanics* vol. 39, no. 1, pp. 19–35.

Kawai, S. and Larsson, J. (2012). 'Wall-modeling in large eddy simulation: Length scales, grid resolution, and accuracy'. eng. In: *Physics of Fluids* vol. 24, no. 1, pp. 015105–015105-10.

Klebanoff, P. S. (1955). *Characteristics of turbulence in boundary layer with zero pressure gradient*. eng.

Kolmogorov, A. N. (1991). 'The Local Structure of Turbulence in Incompressible Viscous Fluid for Very Large Reynolds Numbers'. eng. In: *Proceedings of the Royal Society. A, Mathematical and physical sciences* vol. 434, no. 1890, pp. 9–13.

Kovasznay, L. S. G. (1948). 'The spectrum of locally isotropic turbulence'. eng. In: *Physical review* vol. 73, no. 9, pp. 1115–1116.

Larsson, J. (2022). *Workshop on the status and future directions of wall-modeled large eddy simulation for aeronautical applications*. Available at https://wmles.umd.edu/wall-stress-models/coupling-les-to-a-wall-stress-model/. Accessed 12-April-2022.

Larsson, J. et al. (2016). 'Large eddy simulation with modeled wall-stress: recent progress and future directions'. In: *Mechanical Engineering Reviews* vol. 3, no. 1, pp. 15–00418.

Lee, J., Cho, M. and Choi, H. (2013). 'Large eddy simulations of turbulent channel and boundary layer flows at high Reynolds number with mean wall shear stress boundary condition'. eng. In: vol. 25, no. 11, p. 110808.

Lee, M. and Moser, R. (2015). 'Direct numerical simulation of turbulent channel flow up to $Re_\tau \approx 5200$'. eng. In: *Journal of Fluid Mechanics* vol. 774, pp. 395–415.

Leonard, A. (1975). 'Energy Cascade in Large-Eddy Simulations of Turbulent Fluid Flows'. eng. In: *Advances in Geophysics*. Vol. 18. Elsevier Science & Technology, pp. 237–248.

Lesieur, M., Métais, O. and Comte, P. (2005). *Large-Eddy Simulations of Turbulence*. eng. Vol. 9780521781244. Cambridge: Cambridge University Press.

Lilly, D. K. (1992). 'A proposed modification of the Germano subgrid-scale closure method'. eng. In: *Physics of Fluids. A, Fluid dynamics* vol. 4, no. 3, pp. 633–635.

Lund, T. (2003). 'The use of explicit filters in large eddy simulation'. eng. In: *Computers & mathematics with applications (1987)* vol. 46, no. 4, pp. 603–616.

Mansour, N. N., Kim, J. and Moin, P. (1988). 'Reynolds-stress and dissipation-rate budgets in a turbulent channel flow'. eng. In: vol. 194, no. 1, pp. 15–44.

Marusic, I., Mathis, R. and Hutchins, N. (2010). 'Predictive Model for Wall-Bounded Turbulent Flow'. eng. In: *Science (American Association for the Advancement of Science)* vol. 329, no. 5988, pp. 193–196.

Mathis, R. et al. (2013). 'Estimating wall-shear-stress fluctuations given an outer region input'. eng. In: *Journal of Fluid Mechanics* vol. 715, pp. 163–180.

Moin, P. and Mahesh, K. (1998). 'Direct Numerical Simulation: A Tool in Turbulence Research'. eng. In: *Annual review of fluid mechanics* vol. 30, no. 1, pp. 539–578.

Moser, R. D. (2006). 'On the validity of the continuum approximation in high Reynolds number turbulence'. In: *Physics of Fluids* vol. 18, no. 7, p. 078105.

Mukha, T., Bensow, R. and Liefvendahl, M. (2021). 'Predictive accuracy of wall-modelled large-eddy simulation on unstructured grids'. eng. In: *Computers fluids* vol. 221, p. 104885.

Nicoud, F., Baggett, J. S. et al. (2001). 'Large eddy simulation wall-modeling based on suboptimal control theory and linear stochastic estimation'. eng. In: *Physics of Fluids* vol. 13, no. 10, pp. 2968–2984.

Nicoud, F., Toda, H. B. et al. (2011). 'Using singular values to build a subgrid-scale model for large eddy simulations'. eng. In: *Physics of Fluids* vol. 23, no. 8, pp. 085106–085106-12.

Phillips, O. M. (1991). 'The Kolmogorov Spectrum and Its Oceanic Cousins: A Review'. eng. In: *Proceedings of the Royal Society. A, Mathematical and physical sciences* vol. 434, no. 1890, pp. 125–138.

Piomelli, U. (1999). 'Large-eddy simulation: achievements and challenges'. In: *Progress in Aerospace Sciences* vol. 35, no. 4, pp. 335–362.

Piomelli, U. (2008). 'Wall-layer models for large-eddy simulations'. In: *Progress in Aerospace Sciences* vol. 44, no. 6. Large Eddy Simulation - Current Capabilities and Areas of Needed Research, pp. 437–446.

Piomelli, U. and Balaras, E. (2002). 'Wall-layer models for large-eddy simulations'. eng. In: *Annual review of fluid mechanics* vol. 34, no. 1, pp. 349–374.

Piomelli, U., Ferziger, J. et al. (1989). 'New approximate boundary conditions for large eddy simulations of wall-bounded flows'. eng. In: *Physics of Fluids. A, Fluid dynamics* vol. 1, no. 6, pp. 1061–1068.

Pope, S. B. (2000). *Turbulent flows*. eng. 4th. Cambridge: Cambridge University Press.

— (Mar. 2004). 'Ten questions concerning the large-eddy simulation of turbulent flows'. In: *New Journal of Physics* vol. 6, pp. 35–35.

Prandtl, L. (1925). 'Bericht über Untersuchungen zur ausgebildeten Turbulenz'. In: *Zeitschrift für angewandte Mathematik und Mechanik* vol. 5, no. 2, pp. 136–139.

Pruett, C. (2007). 'Temporal large-eddy simulation: theory and implementation'. eng. In: *Theoretical and computational fluid dynamics* vol. 22, no. 3-4, pp. 275–304.

Reynolds, O. (1995). 'On the Dynamical Theory of Incompressible Viscous Fluids and the Determination of the Criterion'. eng. In: *Proceedings of the Royal Society. A, Mathematical and physical sciences* vol. 451, no. 1941, pp. 5–47.

Sagaut, P. (2006). *Large eddy simulation for incompressible flows : an introduction*. eng. Berlin.

Schlichting, H. and Gersten, K. (2016). *Boundary-Layer Theory*. eng. 9th ed. 2017. Berlin, Heidelberg: Springer Berlin / Heidelberg.

Schlichting, H. and Gersten, K. (2000). *Boundary-Layer Theory*. eng. 8th ed. Revised and Enlarged Edition. Berlin, Heidelberg: Springer Berlin Heidelberg.

Schumann, U. (1975). 'Subgrid scale model for finite difference simulations of turbulent flows in plane channels and annuli'. eng. In: *Journal of computational physics* vol. 18, no. 4, pp. 376–404.

Smagorinsky, J. (1963). 'General Circulation Experiments with the Primitive Equations'. eng. In: *Monthly weather review* vol. 91, no. 3, pp. 99–164.

Spalart, P. R. (1988). 'Direct simulation of a turbulent boundary layer up to R = 1410'. eng. In: *Journal of Fluid Mechanics* vol. 187, pp. 61–98.

Spalding, D. (1961). 'A single formula for the law of the wall'. In: *Journal of Applied Mechanics* vol. 28, no. 3, pp. 455–458.

Speziale, C. G. (1991). 'Analytical Methods for the Development of Reynolds-Stress Closures in Turbulence'. eng. In: *Annual review of fluid mechanics* vol. 23, no. 1, pp. 107–157.

Strogatz, S. H. (2015). *Nonlinear dynamics and chaos : with applications to physics, biology, chemistry, and engineering*. eng. Westview Press, 2465 Central Avenue, Boulder, CO 80301.

Tani, I. (1977). 'History of Boundary Layer Theory'. eng. In: *Annual review of fluid mechanics* vol. 9, no. 1, pp. 87–111.

Taylor, G. I. (1935). 'Statistical Theory of Turbulence'. eng. In: *Proceedings of the Royal Society of London. Series A, Mathematical and physical sciences* vol. 151, no. 873, pp. 421–444.

Tennekes, H. (1972). *A first course in turbulence*. eng. Cambridge, Mass: MIT Press.

Tulapurkara, E. G. (2005). 'Hundred years of the boundary layer — Some aspects'. eng. In: *Sadhana (Bangalore)* vol. 30, no. 4, pp. 499–512.

Von Karman, T. (1931). *Mechanical similitude and turbulence*. Available at https://ntrs.nasa.gov/citations/19930094805. Accessed 4-April-2022.

Vreman, A. (2004). 'An eddy-viscosity subgrid-scale model for turbulent shear flow: Algebraic theory and applications'. In: *Physics of Fluids* vol. 16, no. 10, pp. 3670–3681.

Vreman, B., Geurts, B. and Kuerten, H. (1997). 'Large-eddy simulation of the turbulent mixing layer'. eng. In: *Journal of Fluid Mechanics* vol. 339, pp. 357–390.

White, F. M. (2006). *Viscous fluid flow*. eng. 3rd ed. McGraw-Hill series in mechanical engineering. Boston: McGraw-Hill Higher Education.

Wu, P. and Meyers, J. (2013). 'A constraint for the subgrid-scale stresses in the logarithmic region of high Reynolds number turbulent boundary layers: A solution to the log-layer mismatch problem'. eng. In: *Physics of Fluids* vol. 25, no. 1, p. 15104.

Yang, X. et al. (2015). 'Integral wall model for large eddy simulations of wall-bounded turbulent flows'. eng. In: *Physics of Fluids* vol. 27, no. 2, p. 25112.

Yang, X. I. and Bose, S. T. (2017). 'A physical basis of the slip-wall model for wall-modeled large-eddy simulations'. In: *10th International Symposium on Turbulence and Shear Flow Phenomena (TSFP10)*.

Yang, X. I., Park, G. I. and Moin, P. (2017). 'Log-layer mismatch and modeling of the fluctuating wall stress in wall-modeled large-eddy simulations'. In: *Physical review fluids* vol. 2, no. 10, p. 104601.

Zhiyin, Y. (2015). 'Large-eddy simulation Past, present and the future'. eng. In: *Chinese journal of aeronautics* vol. 28, no. 1, pp. 11–24.